

ABSTRACT

Title of dissertation:

CHARACTERIZATION OF MECHANICAL PROPERTIES AND DEFECTS OF SOLID-OXIDE FUEL CELL MATERIALS

Patrick Owen Stanley
Doctor of Philosophy, 2018

Dissertation directed by:

Professor Eric D. Wachsman
Materials Science and Engineering

Solid-oxide fuel cells (SOFCs) have the potential to help meet global energy demands by efficiently converting fuel to electricity. The technology currently requires high temperatures and has reliability limitations. A critical concern is the structural integrity of the cell after redox cycling at operating temperatures. As new materials are developed to reduce operating temperatures and improve redox stability, the effect of the environment on the mechanical properties must be studied. Ceria-based systems have allowed the operating temperature to be decreased to the 600 °C range. For this reason, a three-point bend apparatus was developed which could test materials up to 650 °C in reducing environments.

Using this apparatus, it was shown how pore geometry and amount affected strength of porous gadolinium doped ceria (GDC) at 650 °C with lower aspect ratio pores, leading to higher fracture strength due to crack tip blunting. The strength of Ni-GDC/GDC half-cell coupons showed no dependence on loading orientation at elevated temperatures in air, but were 47% weaker when the electrolyte was placed

in tension under H₂ as compared to when the electrolyte was placed in compression. It was also determined that a reduced Ni-GDC/GDC coupon could be exposed to air for an extended period of time and reheated under H₂ with no effect to the strength, allowing for more options when processing and preparing cells.

A new anode material, SrFe_{0.2}Co_{0.4}Mo_{0.4}O_{3-δ} (SFCM), was investigated for chemical expansion, oxygen non-stoichiometry, and mechanical properties. SFCM maintains phase purity under reducing conditions, with little changes to lattice parameter between oxidation and reduction, but under oxidation, SFCM forms Sr₂Co_{1.2}Mo_{0.8}O₆ impurities. SFCM supports a large degree of non-stoichiometry, up to $\Delta\delta = 0.176$ at 600 °C, due to a low enthalpy of formation for oxygen vacancies of 39.1 kJ mol⁻¹. Fracture toughness of SFCM was determined to be (0.124 ± 0.023) MPa $\sqrt{\text{m}}$ in air at room temperature and (0.286 ± 0.038) MPa $\sqrt{\text{m}}$ at 600 °C. The strength of SFCM-GDC half-cells increased by 31% upon heating to 600 °C, after which reduction decreased strength by 29%. Reduction and redox cycling were shown to only decrease the characteristic strength, not alter the structural flaw distribution, as microcracks uniformly grew.

CHARACTERIZATION OF MECHANICAL PROPERTIES AND DEFECTS OF SOLID-OXIDE FUEL CELL MATERIALS

by

Patrick Owen Stanley

Dissertation submitted to the Faculty of the Graduate School of the
University of Maryland, College Park in partial fulfillment
of the requirements for the degree of
Doctor of Philosophy
2018

Advisory Committee:

Professor Eric D. Wachsman: *Advisor, Chair*

Professor Peter Sandborn: *Dean's Representative*

Professor Lourdes Salamanca-Riba

Professor Sreeramamurthy Ankem

Associate Professor Isabel K. Lloyd

© Copyright by
Patrick Owen Stanley
2018

Dedication

I dedicate this to my wife, Bethany, who has encouraged and supported me throughout the process, and to my two wonderful daughters, Lucy and Madeleine.

Acknowledgments

I would like to start by thanking my advisor, Dr. Eric Wachsman, for his support during my graduate career. He allowed me the freedom to direct the details of my research and the support to help me reach my goals. He was also supportive of me as my family has grown through the years.

More thanks than I can express is due to my wonderful wife, Bethany, and now our daughters, Lucy and Madeleine. When Bethany and I first met, I was still deciding between graduate programs, and now, after many life changes, she continues to challenge and support me in my endeavors. Lucy and Madeleine have provided me the impetus to continue pushing through the challenges and to strike a balance between my personal and professional pursuits.

Of course, I owe acknowledgement to my parents, Jim and Marilyn Stanley, who raised me to be inquisitive and persistent. Thank you for helping me to become the person that I am today.

The Materials Science and Engineering Department at UMD has been filled with marvelous and helpful people. Dr. Kathleen Hart was one of the first people I met in the department, seemed to help organize everything, and was always there when needed. She has been sorely missed this past year, and I hope she is making the most of her retirement. Kay Morris and Jenna Bishop in the business office help the department run smoothly, if it be answering benefits and procurement questions, or doting on my children when they visit. Of the many professors I have been able to interact with, I would like to especially thank Dr. Isabel Lloyd, who has graciously

given me her advice, helped make introductions, and passed along opportunities to me when they come her way.

Somehow a small group of my friends from undergraduate school have accumulated in the area. It has been a blessing to have them nearby, always willing to help out when need be or to just spend time together. Dave and Katie Shahin are a large part of what brought me to the University, and I am grateful for the continued shared experiences with Dave. Andrew Dunkman has helped me in so many ways, from apartment hunting a thousand miles away to programming questions, for which I express my thanks. And finally, Angela Rudolph has been very supportive of me and my family getting through graduate school.

I owe a good amount of thanks to the various people in lab who helped show me the way to get started with my experiments, allowed me to bounce ideas off them, or helped with the work. Chris Pellegrinelli and Greg Hitz were two people whom I was always comfortable going to and asking what seemed like the most basic questions on how to do things, helping me get started in lab. Drs. Mohammad Hussain and Yi-Lin Huang shared their experience and knowledge of material science as I worked through the fundamentals. Thanks to Tom Hays for being my partner as we started mechanical testing in lab. Ian Robinson, Evans Gritton and Jon O'Neill provided much needed help with SEM, XRD, and modeling, saving me from fumbling through it myself.

I would like to acknowledge my friends and classmates at the University who formed part of my support network, sharing knowledge and encouragement. Mimi Hiebert, Doug Henderson, Michael Van Order, Beth Tennyson, Travis Dietz, Adam

Pranda, Marina Pranda, and Max Lerman, thank you for the time spent in and out of class as we worked through our problems together, laughing and having fun along the way.

Early when starting to look into mechanical properties, I was introduced to Mr. George Quinn at the National Institute of Standards and Technology. Mr. Quinn was kind enough to take much of his time to look though my preliminary work and give me feedback on testing methodology and fractography. It was a great privilege to meet the man who literally wrote the standards that I was attempting to follow and to have his guidance as I started to navigate my way though his world.

Thank you, as well, to Dr. Sean Bishop, who helped guide me as I made my ambitious goals and helped me plan out the steps needed to accomplish them.

Many facilities across campus assisted in the collection and analysis of data for this work. My thanks go to the Advanced Imaging & Microscopy Laboratory (AIMLab), the X-Ray Crystallographic Center, the Surface Analysis Center, and Dr. Robert Bonenberger at the Modern Engineering Materials Instructional Laboratory.

Finally, thank you to Redox Power Systems, the Department of Energy's National Energy Technology Laboratory, and the Maryland Industrial Partnerships Program for supporting this work.

Table of Contents

Dedication	ii
Acknowledgements	iii
List of Tables	ix
List of Figures	x
List of Abbreviations	xiii
1 Introduction	1
1.1 Motivation for Solid-Oxide Fuel Cell Research	1
1.2 Solid-Oxide Fuel Cell Operation	2
1.3 Solid-Oxide Fuel Cell Materials	8
1.4 Mechanical Properties	12
1.5 Summary of Contributions	15
2 Experimental Procedures	18
2.1 Sample Preparation	18
2.1.1 $\text{SrFe}_{0.2}\text{Co}_{0.4}\text{Mo}_{0.4}\text{O}_{3-\delta}$ Powder	18
2.1.2 Bars	18
2.1.3 Test Coupons	19
2.2 Density Measurements	21
2.3 X-Ray Diffraction (XRD)	21
2.4 Thermogravimetric Analysis (TGA)	21
2.4.1 Temperature Programed Desorption (TPD)	23
2.5 Conductivity	24
2.6 Mechanical Testing	24
2.6.1 Development of Mechanical Test Apparatus	26
2.6.2 Atmospheric Treatment	27
2.6.3 Fracture Strength	29
2.6.4 Fracture Toughness	30
2.7 Scanning Electron Microscopy (SEM)	30

3	High Temperature Mechanical Behavior of Porous Ceria and Ceria-Based Solid-Oxide Fuel Cells	32
3.1	Introduction	32
3.2	Results	33
3.2.1	Porosity and Pore Former Choice	33
3.2.2	Flexural Stress Orientation	36
3.2.3	Reduction and Strength	41
3.2.4	Reoxidation at Low Temperatures	44
3.3	Conclusions	49
4	Defect Chemistry and Oxygen Non-Stoichiometry of $\text{SrFe}_{0.2}\text{Co}_{0.4}\text{Mo}_{0.4}\text{O}_{3-\delta}$	51
4.1	Introduction	51
4.2	Results and Discussion	52
4.2.1	Phase Purity and Chemical Expansion	52
4.2.2	Conductivity	55
4.2.3	Temperature Programed Desorption	56
4.2.4	Oxygen Non-Stoichiometry	60
4.2.5	Defect Equilibrium Model and Diagram	62
4.3	Conclusions	67
5	Flexural Strength and Flaw Distributions of $\text{SrFe}_{0.2}\text{Co}_{0.4}\text{Mo}_{0.4}\text{O}_{3-\delta}$ Based Ceramic-Supports for SOFCs at Operating Conditions	69
5.1	Introduction	69
5.2	Results and Discussion	69
5.2.1	Redox Cycling Stability	69
5.2.2	Fracture Toughness	72
5.2.3	Half-cell Strength of Anode-Supported SOFCs at Operating Conditions	74
5.2.4	Strength of Anode Support Layer After Redox Cycling	78
5.3	Conclusions	83
6	Conclusions	87
6.1	Future Work	90
6.2	Publications and Presentations	90
A	Statistics	91
A.1	t-Test	91
A.2	Weibull Statistics	94
B	TGA Manual	98
B.1	Theory of Operation	98
B.2	Mass Measurement	98
B.2.1	Setup and Operation	99
B.3	Heating	103
B.4	Gas Delivery	103

B.5	pO ₂ Measurement	105
B.6	Controls	106
	B.6.1 Gas Controls	106
	B.6.2 Temperature and pO ₂ Measurements	108
	B.6.3 Starting a Run	109
B.7	Interfacing with Other Devices	110
B.8	Troubleshooting	110
C	Code	112
C.1	Arduino PID Relay Furnace Controller with Serial Connectivity	112
	C.1.1 Hardware and Other Libraries	112
	C.1.2 Variables	113
	C.1.3 Serial Communications	113
	C.1.4 Arduino Sketch	114
C.2	MKS Gas Controller and Scheduler	119
	C.2.1 Hardware and Other Libraries	119
	C.2.2 Program Overview	120
C.3	Temperature and pO ₂ Measurements	130
	C.3.1 Hardware and Other Libraries	130
	C.3.2 Program Overview	130
	Bibliography	133

List of Tables

3.1	Chi-squared values for fixed η and variable η fits of porous gadolinium doped ceria, $\text{Gd}_{0.1}\text{Ce}_{0.9}\text{O}_3$ (GDC) strength data (Figure 3.1)	33
3.2	Summary of fit parameters for reduction of NiO-GDC/GDC half-cell coupons under 3% H_2 , 3% H_2O , 94% N_2 at different temperatures.	44
4.1	Refinement results of SFCM before and after exposure to reducing and oxidizing environments	54
4.2	Equations for defect equilibrium under reducing conditions	65
5.1	Summary of strengths for SFCM-GDC/GDC half-cells at different environments	76
5.2	Summary of Weibull fitting parameters (characteristic strength and Weibull modulus) for SFCM-GDC/GDC half-cells at different environments	78
5.3	Summary of Cycled SFCM-GDC anode support layer (ASL) Mechanical Properties	81
5.4	Summary of Weibull Fit Parameters (characteristic strength and Weibull modulus) for Cycled SFCM-GDC ASL	83
B.1	Cahn D200 Microbalance Specifications	99

List of Figures

1.1	Diagram showing flow of materials in the operation of an SOFC.	3
1.2	Diagram showing the triple phase boundary and the importance as being the site where incorporation and reactions occur.	7
1.3	Optical profilometer measurements of a 10 cm by 10 cm Ni-GDC/GDC half-cell where the z-axis has been magnified 6X to highlight curvature	16
2.1	Assembled Alumina 3-Point Bend Fixture	28
2.2	Design drawing and photo of mechanical testing atmospheric chamber	28
3.1	Flexural strength-porosity dependence for porous GDC at 650 °C and 25 °C using spherical poly(methyl methacrylate) (PMMA) or graphite flake pore former: a) Measured strengths fitted using fixed geometric constant; b) Measured strengths fitted using different geometric constants	34
3.2	Scanning electron microscope (SEM) micrographs of porous GDC bars made using: a) PMMA pore former; b) graphite flake pore former . .	37
3.3	Temperature dependent strength of Ni-GDC anode supports and half-cells in both air (filled data points), and reducing atmosphere (3% H ₂ , balance Ar, hollow data points), tested in both “electrolyte-up” and “electrolyte-down” orientations resulting in the electrolyte layer experiencing tension and compression, respectively	39
3.4	Flexural test measurements of coupons sample sets: a) strength at 25 °C b) strength at 650 °C c) modulus at 25 °C d) modulus at 650 °C	40
3.5	SEM micrographs of unreduced half-cell fracture surface tested in air at 25 °C at a) 2k magnification and b) 5k magnification	42
3.6	SEM micrographs of reduced half-cell fracture surface tested in reducing atmosphere at 650 °C at a) 1k magnification and b) 5k magnification	43
3.7	Thermogravimetric analysis curves for Ni-GDC/GDC half-cells showing mass loss over time at temperatures ranging from 550 °C to 750 °C in 3% H ₂ 3% H ₂ O balance N ₂ , 50 sccm flow.	45
3.8	Thermogravimetric analysis of Ni-GDC/GDC half-cell showing no mass gain after reduction and exposure to room temperature and simulated air: a) Mass loss of interrupted reduction with exposure to ambient condition; b) Temperature of sample during cycle c) Oxygen partial pressure measured at the sample during cycle	47

3.9	Flexural properties, a) strength and b) modulus, of Ni-GDC/GDC half-cell coupons after reduction via two different methods, compared to unreduced cells. Strength and modulus show a decrease upon reduction but no significant difference between methods.	48
4.1	a) Powder X-ray diffraction (XRD) patterns of SFCM samples taken after synthesis, reduction, and oxidation compared to pure phase SFCM diffraction pattern. b) Crystal structure of unordered double perovskite SFCM.	53
4.2	Total conductivity as p_{O_2} changes under a) reducing and b) oxidizing conditions at 600 °C.	57
4.3	Temperature programmed desorption of oxygen in SFCM with mass loss from TGA (top) and oxygen desorption from mass spectrometer (MS) (bottom) as it is heated to 800 °C in N_2	59
4.4	Non-stoichiometry (top) and corresponding oxygen vacancy concentration (bottom) of SFCM under oxidizing conditions (right) and reducing conditions (left) at 600 °C	61
4.5	Non-stoichiometry of SFCM as p_{O_2} changes at 400 °C, 500 °C, and 600 °C	63
4.6	Oxygen vacancy and electronic defects in SFCM based on conductivity and TGA non-stoichiometry	66
5.1	a) DC conductivity of SFCM and SFCM-GDC after cycling at 650 °C between 10% H_2 in N_2 and air. b) Mass loss of SFCM-GDC and NiO-GDC during reduction in 3% H_2 /3% H_2O in N_2 at 650 °C.	71
5.2	Mass changes of SFCM during cycling between 21% O_2 and 3% H_2 /3% H_2O in N_2 at 600 °C. Each exposure was 5 hours. a) Percent mass change with time as the gas is switched back and forth. b) Summary of maximum and minimum changes with each cycle.	73
5.3	a) Fracture toughness of SFCM from 20 °C to 600 °C. b) Thermal expansion of SFCM, GDC, and SFCM-GDC.	75
5.4	Flexural strengths of half-cell coupons made from SFCM-GDC anode with GDC electrolyte tested at 20 °C in air, 600 °C in air, and 600 °C in 5% H_2	77
5.5	Fitted Weibull distributions of SFCM-GDC/GDC half-cells at different environments, plotted linearly with 95% confidence intervals shaded.	79
5.6	Scanning electron microscope images of epoxy-filled and polished SFCM-GDC/GDC half-cell cross sections tested at a) 20 °C in air, b) 600 °C in air and c) 600 °C in 5% H_2	80
5.7	Results of four point bend test at ambient conditions of SFCM-GDC ASL with a) strength and b) modulus for samples before any cycling and after 10 redox cycles between 10% H_2 and N_2	82
5.8	Fitted Weibull distributions of SFCM-GDC ASL before any cycling and after 10 redox cycles between 10% H_2 and N_2 , plotted linearly with 95% confidence intervals shaded	84

5.9	Scanning electron microscope images of epoxy-filled and polished SFCM-GDC ASL cross sections tested a) before any cycling, b) after 10 cycles between 10% H ₂ and N ₂	85
B.1	MicroScan Acquisition with Open Method open and the current read out of the balance displayed	102
B.2	Front panel display of Gas Controller program	107
B.3	Front panel display of Gas Scheduler program	107
B.4	Front panel display of Temp & pO ₂ Measurements program	109
C.1	MFC Controller program	122
C.2	Gas Scheduler program	129
C.3	Temperature and pO ₂ measurement program	132

List of Abbreviations

ASL	anode support layer
CDF	cumulative distribution function
csv	comma separated value
GDC	gadolinium doped ceria, $\text{Gd}_{0.1}\text{Ce}_{0.9}\text{O}_3$
GFC	gas correction factor
LSM	lanthanum strontium manganite
MFC	mass flow controller
MIEC	mixed ionic-electronic conductor
MS	mass spectrometer
NI	National Instruments
Po₂	partial pressure of oxygen
PMMA	poly(methyl methacrylate)
PWM	pulse width modulation
SCM	$\text{Sr}_2\text{CoMoO}_6$
SEM	scanning electron microscope
SFCM	$\text{SrFe}_{0.2}\text{Co}_{0.4}\text{Mo}_{0.4}\text{O}_{3-\delta}$
SFM	$\text{Sr}_2\text{Fe}_{1.5}\text{Mo}_{0.5}\text{O}_6$
SMM	$\text{Sr}_2\text{MgMoO}_6$
SOFC	solid-oxide fuel cell
TGA	thermogravimetric analysis
TPB	triple phase boundary
TPD	temperature programmed desorption
UTM	universal testing machine
XRD	X-ray diffraction
YSZ	yttria-stabilized zirconia

Chapter 1: Introduction

1.1 Motivation for Solid-Oxide Fuel Cell Research

The world depends on fossil fuels for its daily energy needs. This is a fact that is going to stay with us for the foreseeable future. By 2040, it is estimated that fossil fuels will still supply 78% of total energy demand. [1] Traditionally, the annual increase in demand is met by an increase in supply of fuel. This increase is supplied by developments in mining and drilling operations, although recent advances have been found to be controversial, such as hydraulic fracturing. [2, 3] These concerns do not even account for the increased emissions caused from combustion of fossil fuels and their effect on the global environment. [4–6]

An alternative to increasing the supply and use of fossil fuels is to increase the efficiency of converting the fuel into useful work. Combustion generators convert chemical energy to thermal energy, then to mechanical energy, and finally into electrical energy. Each energy conversion step has intrinsic losses which limit efficiency. Solid-oxide fuel cells (SOFCs) have the ability to solve this for applications where electrical power is desired. SOFCs side step these losses by allowing for the direct conversion of chemical energy to electrical energy. Power generation plants have efficiencies around 30%, while a stand-alone SOFC generator can convert fuel to

electricity at 45 to 65% efficiency. [7,8] SOFCs are able to run on a variety of fuel sources, such as hydrogen, methane or even biogas. [9] This fuel flexibility and higher efficiency positions SOFCs to bridge the gap in the energy economy as it transitions from fossil fuels to renewable sources. However, many technical hurdles still remain which currently limit SOFCs' viability and must be addressed.

1.2 Solid-Oxide Fuel Cell Operation

The layout for a hydrogen-fueled SOFC is presented in Figure 1.1. Fuel is exposed to the anode side of the cell, while an oxygen rich gas (usually air) is exposed to the cathode side. Separating the two sides is the cell itself, with anode, electrolyte, and cathode. The electrolyte is only conductive to oxygen ions, not electrons. A perfect electrolyte would have no electronic conduction, allowing no leakage current from anode to cathode and forcing all electrons to travel via an alternative route. At the cathode, diatomic oxygen gas will disassociate into oxygen ions, each with a 2– charge from the addition of electrons from the cathode to the oxygen. The oxygen ions then travel though the electrolyte and react with the fuel at the anode, freeing the previously captured electrons. To maintain charge balance, electrons must travel in the opposite direction to the cathode. Because the electrolyte only allows oxygen ions to diffuse though it, the electrons travel though an external circuit performing useful work in the process. A limiting factor in this movement is the ability of oxygen to transport into, through, and out of the cell. As the rate of oxygen transport is increased, the ability for electrons to perform work also increases.

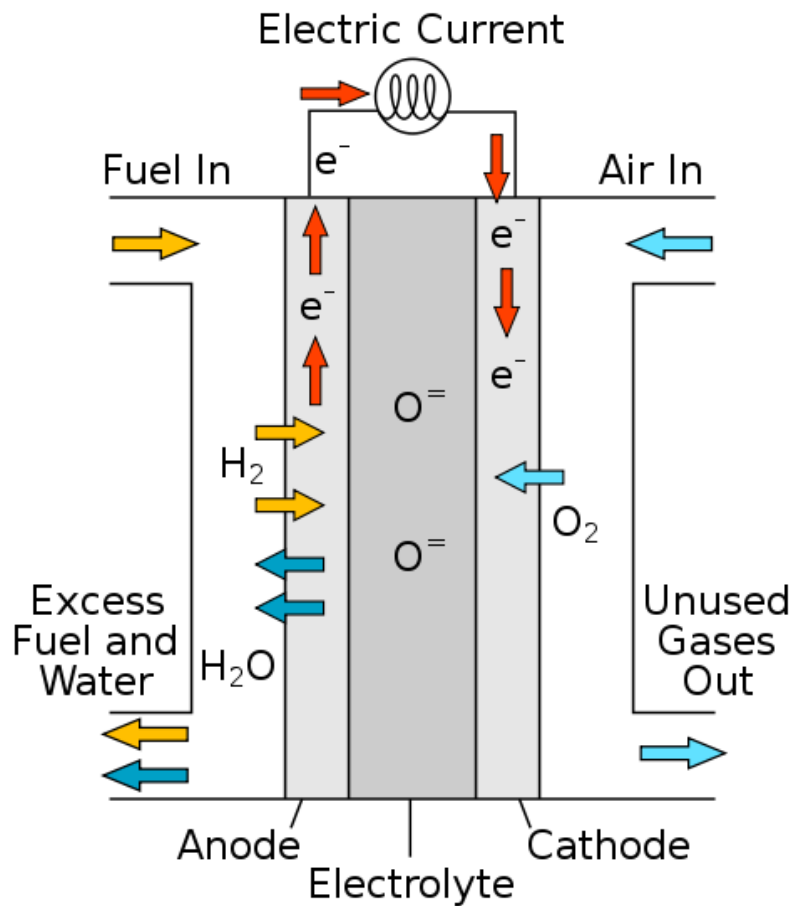


Figure 1.1: Diagram showing flow of materials in the operation of an SOFC. [10]

The driving force for the movement of oxygen ions and electrons comes from the chemical potential gradient across the cell. When the anode is exposed to fuel, it creates a low partial pressure of oxygen (p_{O_2}) in comparison to the cathode, which is exposed to air. This gradient drives the motion of oxygen through the cell from the high p_{O_2} of the cathode to the low p_{O_2} of the anode and generates electric current in the opposite direction to maintain a charge balance. The electrical potential at open circuit conditions (voltage with no current draw) is expressed by the Nernst equation, given in Equation 1.2 for the reaction given in Equation 1.1, where f_A is the fugacity of species A, E^o is the standard potential for the reaction, and n is the number of charges involved in the reaction, R is the ideal gas constant and F is Faraday's constant. [11] Commonly, the fugacity is replaced by the partial pressure of the species. For the case of a hydrogen-fueled SOFC, Equation 1.2 can be simplified to Equation 1.3. [12] From these equations it can be seen that the partial pressures of the involved species have a large role to play in the open circuit voltage of the cell. It is critical that the fuel and air remain separated by the cell. If there is a leak either through the cell or around it, then the electric potential across the cell will decrease, harming performance.



$$E = E^o - \frac{RT}{nF} \ln \left(\frac{f_C^c f_D^d}{f_A^a f_B^b} \right) \quad (1.2)$$

$$E = E^o + \frac{RT}{2F} \ln \left(\frac{p_{H_2}(p_{O_2})^{1/2}}{p_{H_2O}} \right) \quad (1.3)$$

While the electric potential is established by the partial pressure gradient, the electric current is limited by the ionic conduction of oxygen ions from the cathode

to the anode. In ionic conduction, oxygen ions hop from site to site via oxygen vacancies, locations where an oxygen atom is missing from the site it usually occupies in the crystal lattice. Because conduction depends on vacancies, the more vacancies that are present in the lattice, the more available sites for oxygen to move between, the greater the conductance, and the greater power output of a cell. The relationship between oxygen vacancy concentration and oxygen conductance is given by Equation 1.4, where σ_i is the ionic conductivity, $[V_O^{••}]$ is the concentration of oxygen vacancies in the lattice, μ_O is the ionic mobility of the oxygen, and Ze is the total charge of the conducting species. [13] Thus, by adding more oxygen vacancies the ionic conductivity increases. While additional oxygen vacancies are a benefit to the electrical performance of the cell, the resulting changes to the interatomic bonding can weaken bond strengths.

$$\sigma_i = [V_O^{••}]Ze\mu_O \quad (1.4)$$

During operation, oxygen vacancies are created by removal of lattice oxygen from the anode as it reacts with the fuel, as shown in the half-cell reaction of Equation 1.5. This reaction takes place on the surface of the anode, but for convenience it is written where oxygen has associated back into a diatomic state and the fuel subsequently reacts with it. This reaction of fuel with oxygen creates an environment with a very low p_{O_2} at the surface of the anode. A steady state concentration of oxygen vacancies will be reached as the cell comes into equilibrium with the environment, but this concentration will depend on the exact environmental, material, and performance

conditions of the cell.



The cathode and anode materials must facilitate the incorporation of oxygen into the cell and the reaction with the fuel. They must also serve to transport the electrons into and out of the cell as oxygen changes state. As a result, the anode and cathode must possess both electrical and ionic conductivity. To achieve this, a mixture of the electrolyte material and an electronically conductive material are used to create these structures. This mixture of materials creates specific sites where the cell is active, known as triple phase boundarys (TPBs) and demonstrated in Figure 1.2. The TPB is the location where gas, electronic conductor, and ionic conductor meet and oxygen can incorporate into the cell or react with the fuel. To assist gas diffusion to the TPB and to maximize the length of TPBs, pores are added, greatly increasing the available surface area of the electrodes. The more TPBs that are present, the more exchange can occur between the gas and the cell at any given time and the current output of the cell is increased. This added porosity does not come without the disadvantage of decreasing the mechanical strength of the cell. [14, 15]

An operating SOFC would consist of a series of individual cells stacked together for combined power output. The cells would be sealed between current collectors and interconnects and heated to operating temperature. The elevated temperature enables oxygen conduction though the electrolyte by increasing vacancy concentration and mobility but decreases the theoretical voltage due to the equilibrium constant of the H₂/H₂O reaction. Historically, SOFCs operated near 1000 °C, but advances in

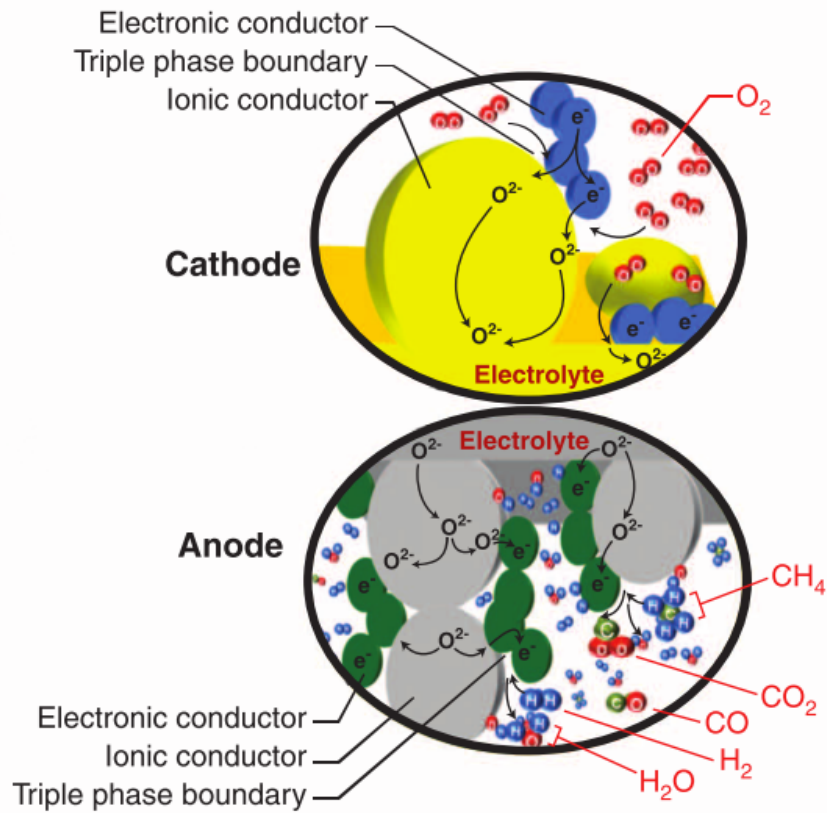


Figure 1.2: Diagram showing the triple phase boundary and the importance as being the site where incorporation and reactions occur. [7]

materials have allowed cells to decrease to the intermediate temperature range (650 °C to 800 °C) and now even further to the low temperature range (below 650 °C). [7] At lower operating temperatures, it becomes easier to create better seals and the stack can be built from more readily available materials. Additionally, the cells are subjected to less thermal expansion, reducing the stresses on the cell.

1.3 Solid-Oxide Fuel Cell Materials

Each structure of an SOFC is fabricated from combinations of materials designed to optimize that part's function then laminated with the other structures to create the cell. For example, a cell can be comprised of a nickel metal-gadolinium doped ceria, $\text{Gd}_{0.1}\text{Ce}_{0.9}\text{O}_3$ (GDC) anode, a GDC electrolyte, and then a lanthanum strontium manganite (LSM) cathode. [16, 17] The individual parts are cast into thin flexible sheets (tapes) from bulk powders, with additives such as pore formers where appropriate, and then laminated together and co-fired to create a single cell. As a result, a completed cell has distinct layers in it where the material and properties abruptly change. This composite structure can then have interdiffusion between layers, smoothing out the abrupt changes, but creating new structures and compositions that were not present upon lamination. [18]

The traditional material used for electrolytes in SOFCs has been yttria-stabilized zirconia (YSZ). YSZ is very stable, has a high strength, has a ratio of ionic conductivity to total conductivity (transference number) of approximately 1, and good conductivity at temperatures in excess of 800 °C even in very low p_{O_2} s. A

high transference number minimizes leakage current due to electronic conduction in the electrolyte, maintaining cell performance. As mentioned previously, GDC is another choice for an electrolyte. Other rare-earth doped cerias have been used as electrolytes, but GDC tends to outperform them under a variety of conditions. At 600 °C, GDC exhibits an order of magnitude higher conductivity than YSZ, but has a smaller electrolytic domain, where the transference number is near 1. [19] Under conditions of high temperature or very low p_{O_2} , GDC will become electrically conductive and start to leak electrons through the electrolyte, reducing cell performance. As SOFC operating temperatures are reduced for improved efficiency, GDC is favored for the electrolyte material.

The anode usually consists of a mixture of the electrolyte material, which provides good ionic conductivity, with an electronic conductor that can facilitate fuel oxidation reactions on the surface. Nickel has commonly been used in the anode due to its high conductivity and catalytic properties. In combination with an ionic conductor, the nickel creates a cermet which functions as the anode. A challenge with nickel is that at ambient conditions it oxidizes into nickel oxide, but at operating conditions it reduces to the desired nickel metal. There is a large lattice parameter change between nickel and nickel oxide, such that, upon reduction it decreases volume by over 15%. As a result, the overall porosity of the anode layer increases as the SOFC is put into service and the anode is exposed to reducing conditions. [20, 21] This increased porosity can greatly decrease the flexural strength and modulus of the anode and of the overall cell. [22, 23] Redox cycling presents an additional challenge because cycling of oxidation and reduction phases causes crack growth and failure

after a few cycles. [14, 15, 21, 24–27] Additionally, nickel is prone to poisoning from sulfur contaminants in the fuel, so alternative anodes are of interest for use in SOFCs.

Alternative metal-ceramic systems have been researched to serve the function of the anode. These have included copper, cobalt, and platinum systems, but each suffer from a significant drawback such as coking, long-term performance degradation or cost. A different approach is to use an all-ceramic anode, made of a mixed ionic-electronic conductor (MIEC) where both ionic and electronic conductions occur simultaneously, such as such as $\text{La}_{1-x}\text{Sr}_x\text{Cr}_{1-y}\text{Mn}_y\text{O}_3$, $\text{Sr}_{0.94}\text{Ti}_{0.9}\text{Nb}_{0.1}\text{O}_{3-\delta}$, $\text{Ba}_{0.98}\text{La}_{0.02}\text{SnO}_3$, or $\text{Sr}_2\text{MgMoO}_6$. [28–34]

Perovskite structures have yielded a number of MIECs with potential uses as electrode materials. [35–37] $\text{Sr}_2\text{MgMoO}_6$ (SMM) and its related family of materials (Sr_2MMoO_6 , where M is a transition metal dopant) yield good conductivities and catalytic actives. [38] The mixed valence state of Mo(VI)/Mo(V) provides high electronic conduction while supporting oxygen vacancy formation. [39] If a dopant is used which has an overlapping redox couple band, such as Fe, electronic conduction can be further improved. Mo(VI) and Mo(V) are stable in both octahedral and tetrahedral coordination, further adding stability to oxygen vacancy formation. [40] $\text{SrFe}_{0.2}\text{Co}_{0.4}\text{Mo}_{0.4}\text{O}_{3-\delta}$ (SFCM) is a recently developed double perovskite MIEC with multiple dopants on the B-site with a high conductivity of 30 S/cm at 650 °C. [41–43] Due to the all-ceramic nature of these anodes, their thermal expansion coefficients better match that of the other ceramic components of the cell, reducing sintering stresses and improving redox cycling durability. [28] Conversely, all-ceramic anodes tend to have lower conductivity and catalytic performance. [44]

This work focuses on the structures in the cell which give mechanical support, the anode and electrolyte. Specifically, Ni-GDC and SFCM-GDC with GDC electrolytes were investigated. While YSZ systems have been studied extensively, the mechanical properties of GDC systems have not been thoroughly explored. As SOFCs are developed which operate at lower temperatures, GDC is the preferred choice for an electrolyte material due to its high conductivity. Ni-GDC serves as a reliable starting place to characterize the mechanical properties of the anode, focusing on the changes which occur during reduction as NiO reduces to Ni metal. SFCM being a new material has no available data on the mechanical properties, let alone the non-stoichiometry which occurs in the material under reducing conditions.

Various cathode materials exist which assist in the incorporation of oxygen into the lattice. The cathode must have many similar properties to that of the anode but be stable in oxidizing environments instead of reducing. As a result, perovskite structures again are found in many of the materials. LSM is one of the most commonly used materials, but others include doped SrCoO_3 , $\text{La}_{0.6}\text{Sr}_{0.4}\text{Co}_{0.2}\text{Fe}_{0.8}\text{O}_3$, $\text{Ba}_x\text{Sr}_{1-x}\text{Ti}_{1-y}\text{Fe}_y\text{O}_{3-y/2+\delta}$. [45–48] The cathode does not tend to play a structural role in the fabrication of a cell, and thus is not investigated or developed in this work.

Outside of the cell itself, several materials are needed to create a functioning stack. Metal interconnects support individual cells, holding them together, creating connections for the current to flow through current collectors and gas to flow through channels to the cell. [49] In intermediate and high temperature stacks, expensive metal alloys such as Inconel must be used to survive the extreme heat. As temperatures are lowered to below 600 °C, more common metals can be used for interconnects, such

as steel. Sealing materials are another critical component to assembly of an SOFC stack. Glasses with transition temperatures near the operating range are used at high temperatures as they can soften and flow into place creating gas tight seals. At lower temperatures new options are available, such as YSZ felt, vermiculite or mica gaskets.

1.4 Mechanical Properties

Ideally, an SOFC is as thin as possible to minimize diffusion path lengths and ionic resistances in the cell. [50] Realistically, the cell must be able to withstand the stresses of being manufactured, sealed, heating, and use. This means that a compromise must be made as to how much the cell is supported and which components do the supporting. Traditionally, electrolyte supported cells were used with YSZ electrolytes where the thick dense electrolyte provides the structural support for the cell. Recently cells with an anode support layer (ASL) made from GDC have been able to provide lower resistances due to the thinner electrolyte while adequately supporting the cell with a thicker anode which fuel can diffuse further into. [51, 52]

Now the anode layer with its porosity must support the majority of the stresses the cell is subjected to.

Ceramic materials used in SOFCs mechanically fail when stresses concentrate at a pre-existing microstructural flaw, overcoming the strength of the material, propagating a crack through the cell. Stresses can be intrinsic to the cell, left from lamination, sinter or cooling, or they can be applied externally during the sealing

or operation of the cell. Microstructural flaws could be intentional with the added porosity or unintended flaws such as inclusions, contamination or grain agglomeration.

Stresses are concentrated most by large, sharp featured flaws. As a result, in a uniform stress field, the largest flaw will usually cause failure. Ceramic materials will tend to fail where the sample is under tensile load and at a location near the point of maximum applied stress. Samples, even if processed together from the same raw materials, will each have a random sampling of flaws from the total batch, and a particular one which causes failure. No matter the care and attention paid to processing, some distribution of flaws will exist. The analysis of the distribution of flaws from a batch of samples is known as Weibull analysis and is explained in detail in Appendix A.2. To perform Weibull analysis, a large number of samples must be tested, but as a result the overall size/shape distribution of flaws can be obtained. This allows for the observation of the flaw distribution and if it changes at different points or if another phenomenon is occurring. One unique benefit of Weibull analysis is that the strength of a sample can be scaled up to a larger piece, as long as the distributions of flaws, or the Weibull modulus, is known.

Most of the materials used in SOFCs have crystal structures which promote the generation of oxygen vacancies. As oxygen vacancies are produced, the inter-atomic bonding of the structure changes, which can decrease the elastic modulus and fracture toughness of the crystal. [53, 54] If the strength of the atomic bonds weakens on average, due to added vacancies, it then follows that the elastic modulus and fracture toughness of the crystal would also decrease. This relationship has been shown to fit for single grains of GDC using nanoindentation, but this does not necessarily hold

true for an actual cell. [55] Grain boundaries can play a large role in the mechanical properties of a bulk sample as they can impede or enhance the propagation of a crack. For this reason, microstructure combined with environmental conditions can play a large role on the overall mechanical properties of a fuel cell.

Another parameter which can change based on environment is the fracture toughness of the material. The fracture toughness is how much stress it takes for a crack to grow and propagate once initiated, or in other words the material's ability to resist crack growth. Just as modulus changes upon heating or reduction, so too can fracture toughness change. Equation 1.6 demonstrates how fracture toughness and flaw geometry impact the strength of a sample, where σ is the strength, K_{Ic} is the fracture toughness, Y is the shape factor for the flaw which caused failure and a is the size of the flaw. [56] The fracture toughness and flaw distributions play a direct role in the overall strength of the cell.

$$\sigma = \frac{K_{Ic}}{Y\sqrt{a}} \quad (1.6)$$

The first external stress applied to the cell, and the one most likely to result in failure, is the sealing of an individual cell into a stack, creating a gas tight seal between the anode and cathode sides. In this process, multiple cells are sandwiched with gasket seals and interconnects between them and compressed until a gas tight seal is achieved. While it is a compressive force that is applied, the cells are never perfectly flat, resulting in flexural stresses as the cell is pressed flat. Figure 1.3 highlights this fact by using an optical profilometer to measure the flatness of a 10 cm by 10 cm Ni-GDC/GDC half-cell. It can be seen that the cell curves by over

a millimeter, mostly at edges, where the seal would be taking place. It is for this reason that the study of the failure of SOFC materials utilizes flexural testing.

1.5 Summary of Contributions

Much of the study of fracture in ceramic materials has been done on technical ceramics for medical applications and for coating metal components. [57–64] These materials are optimized for fracture toughness and durability and very rarely experience temperatures above a few hundred degrees Celsius. The fracture surface analysis and correlations between microstructure and strength described for these materials are a valuable starting point for investigating fuel cell materials. However, there is a lack of extensive investigation into the properties of low temperature SOFC materials at their expected operating temperatures and environments.

Most of the previous research into the mechanical properties of SOFCs has focused on YSZ based devices. [21, 65, 66] This material has been the standard for the field and has desirable mechanical properties but requires high temperatures to function well. Nakajo et al. conducted a wide ranging study of materials used in anode supported SOFCs which included some attention to temperature and atmosphere effects but did not go beyond YSZ. [66] As efforts are made to lower SOFC operating temperatures, a shift to ceria-based electrolytes has occurred. Less attention has been given to the mechanical behavior of doped ceria materials across SOFC operating conditions. Flexural strength and Young's modulus measurements for GDC have been carried out in ambient conditions by Yasuda et al. [67] They characterized the

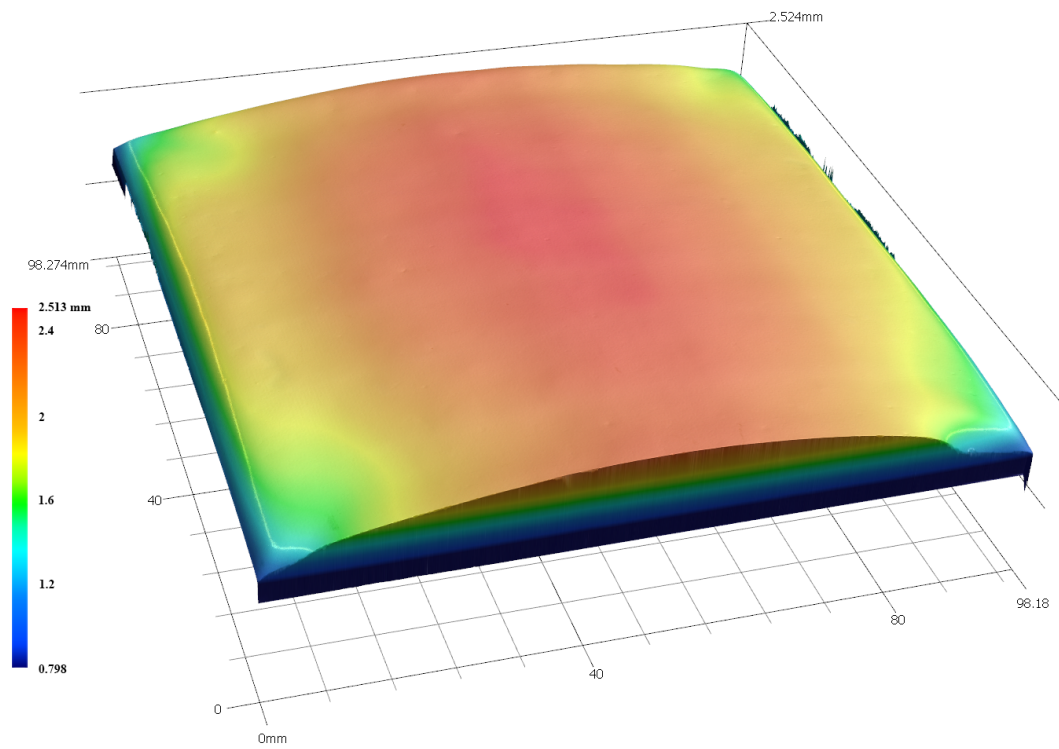


Figure 1.3: Optical profilometer measurements of a 10 cm by 10 cm Ni-GDC/GDC half-cell where the z-axis has been magnified 6X to highlight curvature

effects of sintering temperature on density and the resulting mechanical properties. Further testing of this material system at elevated temperatures and anode gas reducing environments must be done to fully understand the mechanical behavior of GDC.

Additionally, most research has focused on measuring and comparing the Young's moduli of different materials as it changes with temperature or after reduction treatments at room temperature. [20, 68–70] While the modulus can be correlated to the fracture strength of the cell, direct measurement of flexural strength remains the best means to characterize the strength of the cell.

To help develop SOFCs into a viable technology which can stretch the gap in the energy economy, research is needed to improve the reliability of the cells during manufacturing and operation. This work aims to develop the understanding of fracture mechanics of real-world structures, by understanding how temperature and partial pressure of oxygen affect the strength, fracture toughness, and flaw distributions of SOFC components. This was done by analyzing the flexural properties of bulk bars and half-cell coupons at ambient conditions and at conditions similar to those found in an SOFC. Microscopy was used to look for changes in microstructure after various treatments in addition to Weibull analysis. Additionally, thermogravimetry, conductivity, and temperature programed desorption were used to understand the atomic defect structure of a new material to relate it to the mechanical properties.

Chapter 2: Experimental Procedures

2.1 Sample Preparation

2.1.1 $\text{SrFe}_{0.2}\text{Co}_{0.4}\text{Mo}_{0.4}\text{O}_{3-\delta}$ Powder

SFCM was created from stoichiometric amounts of strontium carbonate (SrCO_3 , Sigma-Aldrich), iron oxide (Fe_2O_3 , Sigma-Aldrich), cobalt oxide (Co_2O_3 , Infram Advanced Materials), and molybdenum oxide (MoO_3 , Alfa-Aesar) using conventional solid-state methods. The constituents were ball milled for 24 hours in ethanol and dried using a 100 °C oven. Afterwards the powder was calcined at 1100 °C for four hours.

2.1.2 Bars

Porous GDC bars were created by uniaxially pressing a mixture of GDC and pore former in a rectangular die. GDC powder ($\text{Gd}_{0.1}\text{Ce}_{0.9}\text{O}_3$, **fuelcell**materials) was mixed with the varying amounts of poly(methyl methacrylate) (PMMA) microspheres (5 μm diameter) or graphite flake with 0.1wt% of polyvinyl butyral added to act as a binder during pressing and a drop of fish oil to act as a dispersant during milling. Different pore geometries were created from the flake and spherical

pore formers. The PMMA or graphite was burned out by pre-sintering at 400 °C, which was followed by sintering at 1500 °C for 4 hours. Percent porosity was measured using the Archimedes density technique and samples were polished with 600 grit sandpaper before testing.

Dense SFCM bars were used to maximize the total mass and mass changes during thermogravimetric testing. Samples were made by combining SFCM powder with 0.6 wt% polyethylene glycol 600, 1.8 wt% ethylene glycol, and 0.6 wt% glycerol in isopropyl alcohol and ball milling overnight. After drying at 100 °C, the powder was ground by mortar and pestle, then pressed uniaxially into rectangular bars at 30 MPa, then isostatically pressed at 30 MPa. Bars were sintered by heating to 400 °C for one hour and then 1340 °C for four hours, using a $3\text{ }^{\circ}\text{C min}^{-1}$ heating and cooling rate. This produced bars with 97% theoretical density by Archimedes' technique. To create fracture toughness test samples, dense bars were cut and sanded to final dimensions of 3 x 4 x 25 mm. The chevron notch required for testing was cut using the jig described by Jenkins, Chang and Okura following the ASTM procedure. [71, 72]

2.1.3 Test Coupons

Tape casting was used to create ASL and half-cell coupons used in flexural testing. A 6:4 weight ratio of NiO and GDC was ball milled with ethanol, toluene, and Menhaden fish oil for 24 hours. Afterwards, polyvinyl butyral and benzyl butyl phthalate were added as binder and plasticizer and the mixture was ball milled for an additional 24 hours. The slurry was degassed using a vacuum and then tape

cast using a 700 μm doctor blade height. After drying overnight, the tapes were cut into 12 cm by 12 cm squares. Three squares were layered on top of each other and laminated using a hot press at 49 $^{\circ}\text{C}$ for 30 minutes at 2 tons. After lamination, the green tapes were cut into rectangular coupons which measured 25 mm by 10 mm. The sample coupons were fired at 1400 $^{\circ}\text{C}$ for 4 hours, after which the average final dimensions were 8.16 x 24.15 x 2.98 mm.

A GDC electrolyte layer was cast using a 40 μm blade height for the creation of half-cell coupons. Three ASL layers were laminated as before, then the additional single electrolyte layer as before was laminated on for 2 hours. Half-cell coupons were sintered at the same parameters as the ASL coupons.

Tape casting was also used to create test coupons of porous SFCM-GDC ASL and SFCM-GDC/GDC half-cells. Using ethanol as a solvent, SFCM-GDC was ball milled with polyvinyl butyral, benzyl butyl phthalate, 12 μm PMMA (16 wt% with respect to SFCM-GDC), and Menhaden fish oil. The tape was cast to a thickness of 110 μm on Mylar then laminated using a hot press to a final thickness of 660 μm . Dense GDC was casted to 30 μm and laminated to the top of the SFCM-GDC to create half-cells. Individual coupons were cut from the green tape, sintered at 1200 $^{\circ}\text{C}$ for four hours, with holds at low temperatures to burn out organic binder and pore former. The final thicknesses were measured to be 400 μm for the SFCM-GDC ASL and \sim 20 μm thick GDC electrolyte.

Test coupons had their edges sanded to remove defects left from cutting, following ASTM standards. [73] Top and bottom surfaces were not sanded to preserve possible defects left from tape casting procedure, which would be representative of

industrially manufactured SOFCs.

2.2 Density Measurements

Density of test bars was determined using the Archimedes method following Equation 2.1, where ρ is the density of the sample, ρ_{liq} is the density of the liquid used, w_{dry} is the weight of the sample before submersion and w_{sub} is the apparent weight after submersion. Isopropyl alcohol was used as the liquid for measurements and samples were placed in a vacuum chamber while submerged to ensure all open porosity was filled before measuring the submerged weight.

$$\rho = \frac{w_{dry}}{w_{dry} - w_{sub}} \rho_{liq} \quad (2.1)$$

2.3 X-Ray Diffraction (XRD)

X-ray diffraction (XRD) was used to confirm phase purity of the SFCM after synthesis and during the testing process. A Bruker D8 Advance with LynxEye was used with a Cu K α source. A step size of 0.02° was used with a dwell of 0.8 s. GSAS-II was used to perform the Rietveld refinement calculations and VESTA was used to visualize the unit cell. [74, 75]

2.4 Thermogravimetric Analysis (TGA)

Thermogravimetric analysis (TGA) of samples during oxidation or reduction was measured using a Cahn D200 microbalance. The samples were placed in a crucible suspended from a platinum wire or suspended from the wire itself. The wire

attached to the microbalance and was enclosed by an alumina tube inside a furnace. Heating control was achieved with a PID loop and temperature measurement done by a K-type thermocouple placed immediately below the sample inside the furnace tube. A heating and cooling rate of $10\text{ }^{\circ}\text{C min}^{-1}$ was used. Mass, temperature, and p_{O_2} measurements were taken at fixed intervals.

Gas flow was controlled at consistent 50 sccm by mass flow controllers, which mixed dry nitrogen, oxygen, hydrogen, and humidified nitrogen to obtain the p_{O_2} desired. For general oxidizing or reducing conditions, 21% O_2 in N_2 , or 3% H_2 , 3% H_2O in N_2 was used. Measurements of the p_{O_2} were taken by a calibrated YSZ oxygen sensor at $800\text{ }^{\circ}\text{C}$ located before the sample. For glsSFCM, intermediate p_{O_2} ranges were not able to be tested due to SFCM's incompatibility with the species required to create that environment.

Further details of the operation of the TGA and its various components are given in Appendix [B](#).

To prepare a sample for non-stoichiometry measurements, it was pre-weighed, wrapped in platinum wire and suspended from the balance, placed in the furnace with simulated air (21% O_2 , 79% N_2) flowing. Once the mass had stabilized, the furnace was heated to $800\text{ }^{\circ}\text{C}$ to allow for any organic contamination to burn off. After the mass stabilized at this elevated temperature, the sample was introduced to various environments. The mass of the sample would be noted only after steady state had been reached for a condition. After testing a sample, a bar of alumina was cut to the same dimensions as the sample and the process was repeated to obtain a blank which could be subtracted from the measurements to remove buoyancy effects.

Oxygen non-stoichiometry was calculated using Equation 2.2, where $\Delta\delta$ is the change in oxygen stoichiometry, MW_{SFCM} is the molecular weight of SFCM ($208.74 \text{ g mol}^{-1}$), MW_O is the molecular weight of oxygen (16.0 g mol^{-1}), w_{sample} is the weight of the sample, and Δw is the weight change as recorded by the TGA. The oxygen vacancy concentration ($[\text{V}_O^{\bullet\bullet}]$) is calculated using Equation 2.3, where ρ is the density of SFCM and N_A is Avogadro's number. To calculate the oxygen vacancy concentration, the non-stoichiometry of SFCM at a point needs to be established. For this work, based on the plateau present in the data at oxidizing conditions, it is assumed that in a pure oxygen environment ($\log(p_{\text{O}_2}) = 0$) all oxygen vacancies are filled with no oxygen interstitial or surface species, thus $\delta = 0$.

$$\Delta\delta = \frac{MW_{SFCM}}{MW_O w_{sample}} \Delta w \quad (2.2)$$

$$[\text{V}_O^{\bullet\bullet}] = \frac{\delta\rho N_A}{MW_{SFCM}} \quad (2.3)$$

2.4.1 Temperature Programed Desorption (TPD)

The effluent from the TGA was used as the inlet to a mass spectrometer (MS) to perform temperature programmed desorption (TPD). The sample was prepared as before and heat treated to remove any carbon contaminants but was allowed to cool under simulated air. It was then heated to 800°C at 5°C min^{-1} under a 50 sccm flow of nitrogen as the MS measured the 32 m/z signal which corresponded to O_2 desorption. Additional m/z signals were monitored to observed for other species.

2.5 Conductivity

Electric conductivity across p_{O_2} was measured using the four-wire technique and a Stanford SR 830 lock-in amplifier. A bar shape sample was used with dimensions of $6.46\text{ mm} \times 3.3\text{ mm} \times 1.3\text{ mm}$. Gold paste was used as a current collector, and the current range was between 0.005 to 0.05 A. A YSZ oxygen sensor operating at $800\text{ }^\circ\text{C}$ was used to monitor the changes in oxygen partial pressures. Intermediate p_{O_2} ranges were not tested due to an incompatibility between SFCM and the CO and CO_2 required to obtain those p_{O_2} .

Conductivity during redox cycling was measured using rectangular bars of SFCM and SFCM-GDC (2:1) composite. The samples were connected to a Keithley 2400 source meter by silver paste and wire. Using an in-house built reactor, the sample could be heated and the gas environment could be controlled. An initial measurement was taken after heating and 50 hours of exposure to 10% H_2 in N_2 , then the sample exposed cycled between air and reducing conditions over a period of 14 days.

2.6 Mechanical Testing

Measurements of mechanical properties were collected using a Tinius Olsen 10ST universal testing machine (UTM) equipped with a 250 N load cell. Experiments where any samples would be tested at elevated temperatures or under reducing environments were conducted using a custom built three point flexural test fixture

placed inside a gas-tight chamber and furnace. Otherwise, a fully-articulating four point flexural test fixture was used. Samples tested at ambient conditions were placed on the appropriate testing fixture and loaded until failure. For samples tested at elevated temperatures, the sample was heated in the test chamber at $10\text{ }^{\circ}\text{C min}^{-1}$, allowed to equilibrate for 20 minutes, then tested. Samples to be reduced were placed in the chamber and exposed to reducing conditions as described below.

All strength tests conducted in the UTM were done at a rate of 0.2 mm min^{-1} with a 20 mm lower span. After measuring the force at fracture, stress was calculated using Equation 2.4 for 3-point flexural of rectangular samples, where σ_f is the stress at failure, F is the load at failure, L is the span of the fixture, b is the width of the sample and d is the thickness of the sample. At room temperature, the coupons or bars were loaded into the fixture and tested in batches of 5 per condition. Occasionally samples would break or be damaged before testing, reducing the sample set. For sample sets at elevated temperatures in ambient atmosphere, the samples were loaded into the front of the chamber, acting as a staging area, prior to heating the on fixture in the center. Upon transferring the next coupon from the staging area to the fixture, a 20 minute waiting period was used to ensure that the coupon had reached thermal equilibrium prior to testing.

$$\sigma_f = \frac{3FL}{2bd^2} \quad (2.4)$$

Following the completion of the set, all coupon pieces were cooled at a rate of $10\text{ }^{\circ}\text{C/min}$. For testing in reducing atmosphere, each coupon was reduced and tested individually. Half-cell coupons were tested in two orientations, “electrolyte-up” and

“electrolyte-down.” These orientations cause the dense electrolyte layer to experience compressive or tensile stress. The “electrolyte-up” orientation subjects the electrolyte to compressive stress and vice-versa.

2.6.1 Development of Mechanical Test Apparatus

To develop a testing apparatus capable of simulating the various conditions experienced by operating SOFCs, appropriate materials were chosen based on thermal and chemical stability criteria. Alumina was chosen to build the bend fixture due to its chemical stability and high hardness. The sample rests crossways on two stationary 6.35 mm diameter rods which are placed in troughs separated by 20 mm. The upper half of the fixture consists of a 6.35 mm rod used to apply stress to the sample from the UTM crosshead. Both pieces are attached using silica-based cement to 300 mm rods attached at the anchor points of the UTM. Assembly and alignment is assisted with the use of a 3D printed jig to ensure repeatability. The complete alumina, 3-point bend fixture is seen in Figure 2.1 with the two bottom rollers, a sample, and the top roller making contact, applying flexural stresses to the sample.

To create the atmosphere control system, a combination of standard and custom vacuum system parts were used to enclose the bend fixture. For the main body of the chamber, a 3-inch inner diameter, stainless steel tee was made with QF80 and QF50 flanges. Welded NPT ports on top and bottom allow for gas inlet and outlet and the introduction of a thermocouple through a Swagelok Ultra-Torr fitting. Figure 2.2 shows the engineering drawings and photo of the custom pieces from

A&N Corp. Flexible bellows allow for the motion of the cross-bar to be translated into the fixture, requiring the subtraction of the spring force to be removed during analysis. The alumina fixture was then inserted through each end and the chamber incorporated into the furnace with QF50 to 1/2 inch tube adapters that fit over the alumina rods.

To heat the fixture and chamber, a 1 ft. cube was assembled from steel plates with cutouts on top, bottom and front. Steel wire mesh was used to create a framework inside to hold nickel-chromium alloy heating elements. Silica-based wool insulation was packed between the center cavity and the case walls. A K-type thermocouple was inserted into the chamber and used with an external PID controller to cycle the heating elements. The furnace was placed on a supporting scaffold to hold it in position during tests. The test fixture, atmosphere chamber, and furnace were affixed together as one unit and inserted into the UTM. The design was compared and qualified to a regular steel 3-point bend apparatus to ensure accurate results at room temperature.

2.6.2 Atmospheric Treatment

To test individual coupons under reducing environments, samples were loaded into the test chamber at 400 °C, after previous pre-heating in the staging area. After 20 minutes, the temperature would be increased to the desired set-point of 650 °C at a ramp rate of $10\text{ }^{\circ}\text{C min}^{-1}$ and the gas would be switched first to N₂ to flush the chamber, then to humidified argon containing 3% H₂. It would then be allowed to

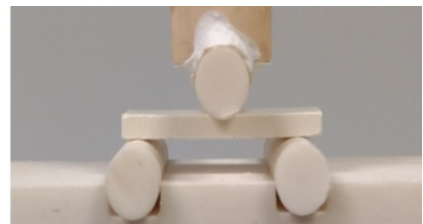


Figure 2.1: Assembled Alumina 3-Point Bend Fixture

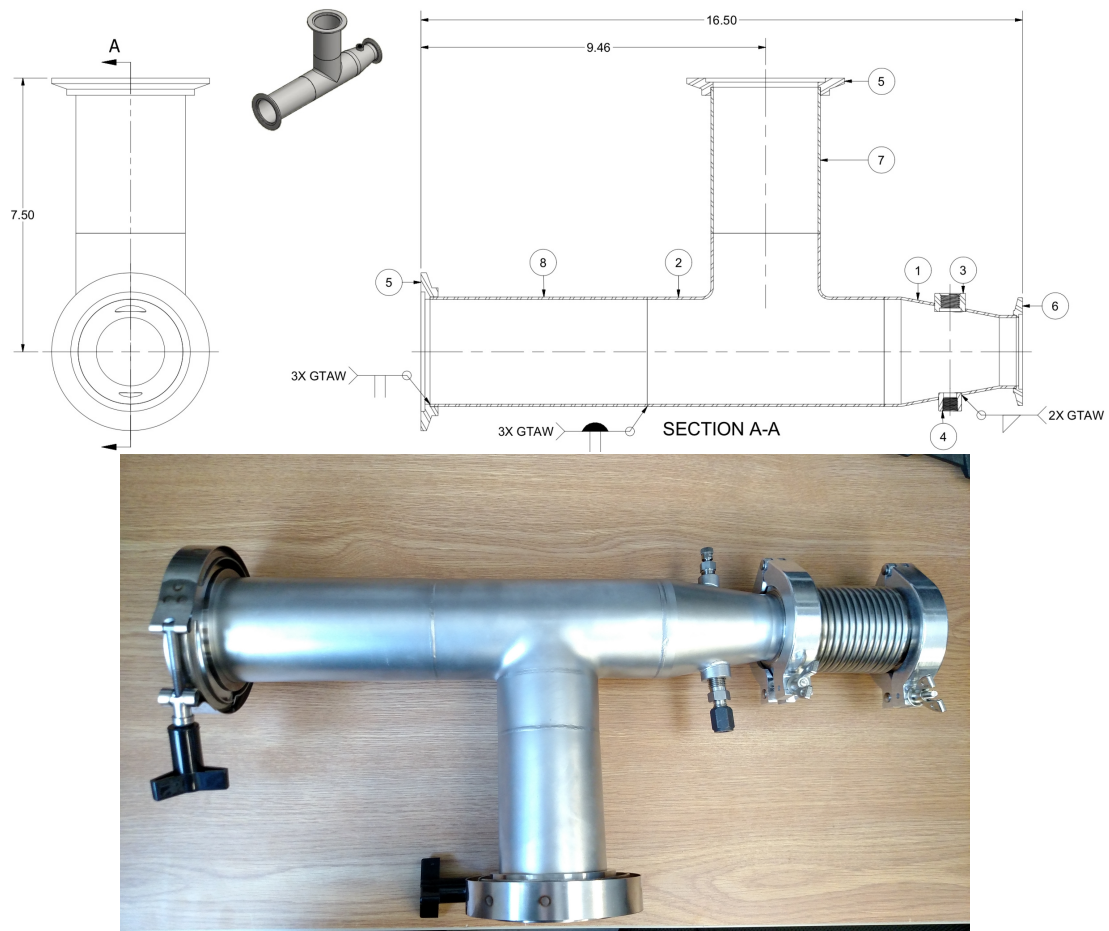


Figure 2.2: Design drawing and photo of mechanical testing atmospheric chamber

sit for 18 hours before testing to allow reduction. After testing, the chamber would be flushed again with N₂ and cooled to 400 °C before opening to change samples and repeat the process.

If samples had been previously reduced as a batch by exposure to hydrogen in a tube furnace and cooled under hydrogen, the atmospheric treatment was shortened, as supported by TGA results. Pre-reduced samples were loaded into the chamber at or below 400 °C, the chamber flushed N₂, then with H₂ in Ar. After this the chamber would be heated to 650 °C, the sample tested after a 30 minute period and cooled back down to 400 °C. At this point, the chamber would be flushed with N₂. While the chamber maintained a positive pressure of N₂, it could be opened, a new sample loaded, closed, and allowed to flush. This procedure allows for the batch reduction of many test coupons and replaced the 18 hour reduction time with a shorter 30 minute period.

2.6.3 Fracture Strength

A loading rate of 0.2 mm/min was used for all strength measurements. Strength was calculated from the maximum force measured before failure according to Equation 2.5 or 2.4 depending on if the four point or three point fixture is used respectively, where σ is the strength, P is the maximum force, L is the span width of the test fixture, b is the width of the sample and d is the thickness of the sample. Equation 2.5 is for a fixture where the top span is 1/2 the width of the bottom span. [73]

$$\sigma = \frac{3PL}{4bd^2} \quad (2.5)$$

2.6.4 Fracture Toughness

The fracture toughness of chevron notched samples were measured using a loading rate of 0.001 mm/min. Fracture toughness was calculated from the maximum force using Equation 2.6 or 2.7 for four point or three point fixtures. [72, 76] Y_{min}^* is the shape factor as calculated by Equation 2.8, S_o and S_i are the outer and inner spans, B is the width of the sample, W is the height of the sample, a_0 is the distance from the tip of the chevron notch to the bottom of the sample, and a_1 is the average distance from the side of the chevron notch to the bottom of the sample. Each sample was measured after failure, but in this study the approximate values were

$$S_o = 40\text{mm}, S_i = 20\text{mm}, B = 3.0\text{mm}, W = 4.0\text{mm}, a_0 = 0.80\text{mm}, a_1 = 3.8\text{mm}.$$

Fracture toughness was measured only under air at room temperature and up to 600 °C. Under reduction the fracture toughness bars of SFCM would spontaneously fracture, preventing measurements under that condition.

$$K_{Ivb} = Y_{min}^* \left[\frac{P[S_o - S_i]}{BW^{3/2}} \right] 10^{-6} \quad (2.6)$$

$$K_{Ivb} = Y_{min}^* \left[\frac{P}{BW^{1/2}} \right] 10^{-6} \quad (2.7)$$

$$Y_{min}^* = \frac{0.38742 - 3.0919(a_0/W) + 4.2017(a_1/W) - 2.3127(a_1/W)^2 + 0.6379(a_1/W)^3}{1.0000 - 2.9686(a_0/W) + 3.5056(a_0/W)^2 - 2.1374(a_0/W)^3 + 0.0130(a_1/W)} \quad (2.8)$$

2.7 Scanning Electron Microscopy (SEM)

After fracture, scanning electron microscope (SEM) images were taken of the fracture surfaces. This was to observe the nature of the crack as it propagated,

determining if it was transgranular or intergranular fracture, to find any flaws on the fracture which would lead to failure, and to observe pore geometry. Images were captured on an Hitachi SU-70 Schottky field emission SEM. Fracture surface images were mounted vertically and GDC samples were sputter coated with gold. Observations of porosity were taken using epoxy infiltrated samples and polished using down to a $0.25\text{ }\mu\text{m}$ diamond solution.

Chapter 3: High Temperature Mechanical Behavior of Porous Ceria and Ceria-Based SOFCs

3.1 Introduction

This study presents the results of a broad range of flexural tests involving the materials used in ceria-based anode supported SOFCs along with the assembled half-cells. Using a purpose-built temperature controlled environmental chamber installed in a UTM, porous doped ceria bars, ASLs composed of nickel and doped ceria cermet, and half-cells composed of an ASL and a doped ceria electrolyte were tested. The various test conditions used included expected operating temperatures ($450\text{ }^{\circ}\text{C}$ – $650\text{ }^{\circ}\text{C}$), and both reducing and oxygenated atmospheres. These variations in test conditions are important because these cells must maintain their integrity from when they are first placed in a sealed stack to when they reach operating conditions. In particular, this study was intended to determine at what point in their life SOFCs are most vulnerable to mechanical failure and the mechanisms involved. Additionally, the effect of the anode-electrolyte interface on flexural strength was explored.

3.2 Results

3.2.1 Porosity and Pore Former Choice

As expected, GDC bars with greater porosity displayed lower flexural strength values as compared to less porous samples. The relationship between porosity and strength followed an exponential trend. This behavior is well established for porous ceramics and is described by Equation 3.1, where σ_f is the flexural strength with porosity, σ_o is the flexural strength without porosity, η is a geometric constant dependent on the system, and P is the volume percent porosity of the sample. [77]

$$\sigma_f = \sigma_o e^{-\eta P} \quad (3.1)$$

The data was fit using this equation and both a fixed geometric constant, η , of 0.047 (Figure 3.1a) and a variable geometric constant (Figure 3.1b). Chi-squared values, indicating the divergence of the fit from the measured data for each sample set, were calculated for the two fitting methods and are displayed in Table 3.1.

The deviance from the fit curve for the fixed η method is quite large relative

Table 3.1: Chi-squared values for fixed η and variable η fits of porous GDC strength data (Figure 3.1)

Sample Set	χ^2 (Fixed η)	χ^2 (Variable η)
GDC PMMA 650	3.406	0.062
GDC Graphite 650	0.668	0.008
GDC Graphite 25	3.575	5.063

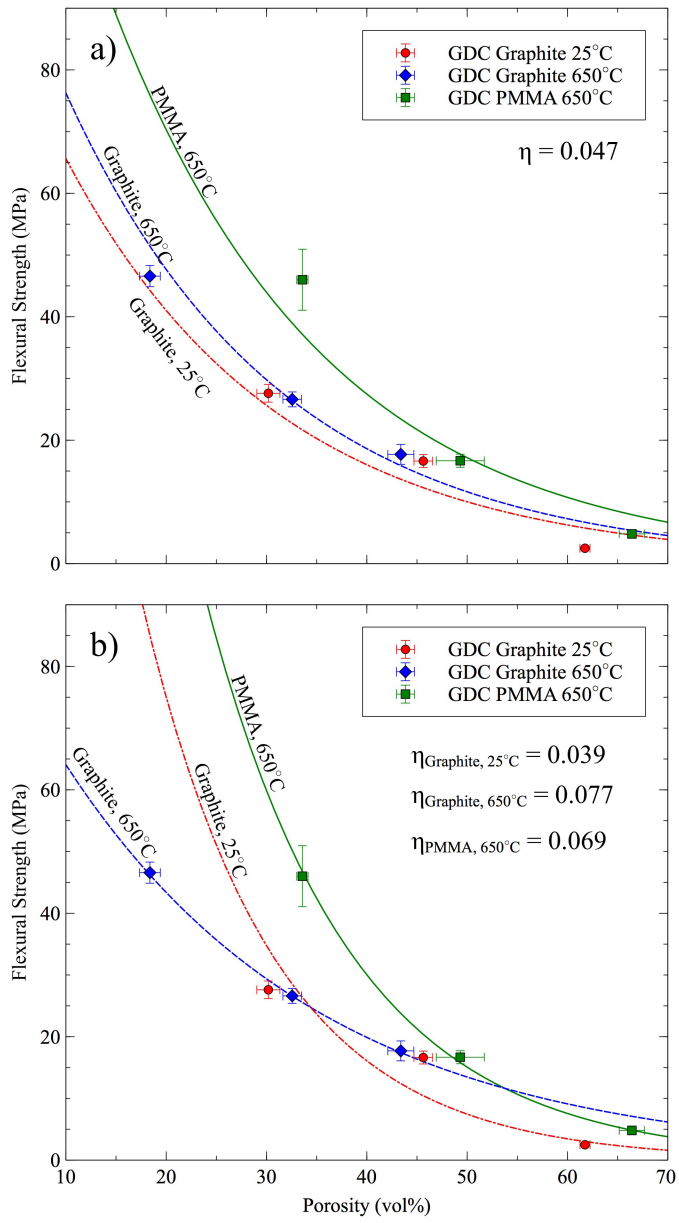


Figure 3.1: Flexural strength-porosity dependence for porous GDC at 650 °C and 25 °C using spherical PMMA or graphite flake pore former: a) Measured strengths fitted using fixed geometric constant; b) Measured strengths fitted using different geometric constants

to the variable η fit for both sample sets tested at 650 °C. Both fitting methods are fairly poor in the case of the room temperature graphite set. The poor fitting results in this case are due to the >60% porosity samples. The flatter pore geometry caused by the graphite likely leads to comparatively greater strength loss at high porosity due to greater pore connectivity. The comparison between the high temperature data sets is the most useful, given this, and the fact that SOFCs operate at this temperature. The poor fit of fixed η models suggests that a material-specific η value may be an oversimplification of the porosity-stress relationship in ceramics.

Samples tested at higher temperatures displayed a slightly higher flexural strength. Generally, it is expected that increasing temperature lowers strength of dense ceramics once plastic deformation processes become activated at high temperatures. [78] Below the temperature at which plastic deformation starts to occur, temperature has a minimal effect on flexural strength of dense ceramics. For dense GDC, it has been demonstrated that the strength decreases by 19% between room temperature and 800 °C. [13] Porosity changes this behavior by essentially creating a composite material, keeping the rate of change constant or increasing with temperature. [68] For porous GDC, thermal expansion places a compressive stress on any surface flaws that are sites for crack initiation and propagation. Additionally, the porosity helps reduce bulk stresses caused by thermal expansion. These two effects increase the material's fracture strength more than any decrease from plastic deformation at 625 °C.

Cross-sectional SEM of the fracture surfaces of the porous GDC samples, both PMMA and graphite, is shown in Figure 3.2. Figure 3.2a shows individual spherical

pores left by the PMMA while Figure 3.2b has an inter-connected network of long pores left by the graphite flakes.

The differences in quality of fit between Figure 3.1a and Figure 3.1b shows that the geometric factor is microstructurally dependent. Samples with porosity formed using PMMA spheres showed significantly greater strength as compared to samples with graphite-formed porosity. This can be explained by the effect of pore geometry on crack initiation and propagation in the ceramic. If a crack enters a pore, the pore can now be considered the new crack tip. The energy required to advance the crack is highly dependent on the geometry of the tip. For a spherical pore, this geometric factor is maximized and results in higher resilience to fracture. This is summarized by Equation 3.2 where σ_o is the stress at the crack tip, c is the length of the crack tip and ρ is the radius of curvature of the crack tip. [79]

$$\sigma_f = \frac{\sigma_o}{2} \sqrt{\frac{\rho}{c}} \quad (3.2)$$

Based on the mechanical behavior of these samples, porous ceramics should be designed and constructed such that the pore geometry is as low aspect ratio as possible to maximize strength.

3.2.2 Flexural Stress Orientation

Figure 3.3 shows the measure flexural strengths of a number of SOFC coupon samples. Anode support coupons were tested along with half-cells consisting of anode supports and electrolyte layers at temperatures ranging from 25 °C to 650 °C. The highest temperature test was repeated with coupons under reducing conditions (3%

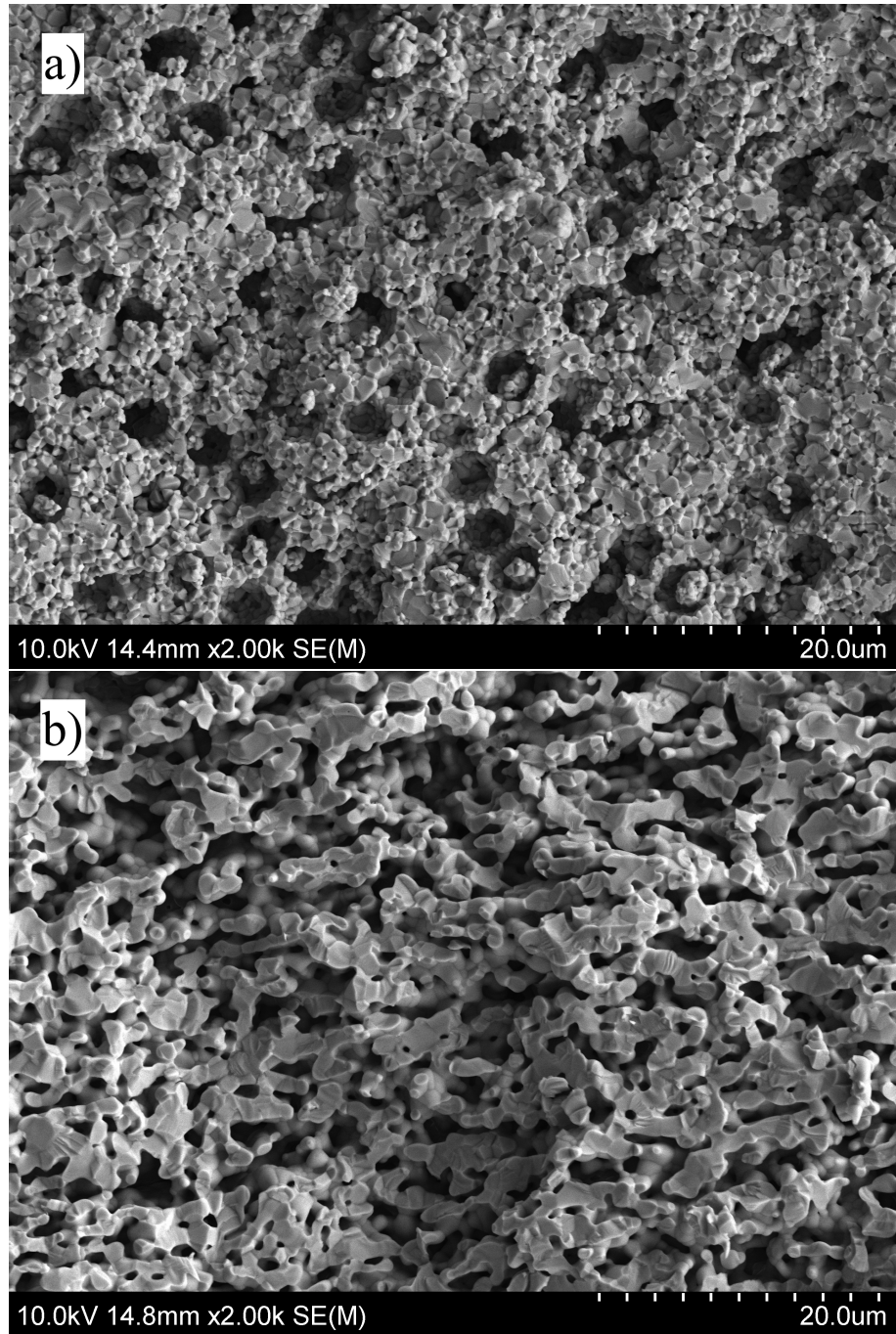


Figure 3.2: SEM micrographs of porous GDC bars made using: a) PMMA pore former; b) graphite flake pore former

H_2 , balance Ar).

All unreduced sample types showed increased strength at elevated temperatures with little difference between types at a given temperature. The high-temperature reduced coupons displayed large differences in strength depending on the orientation of the sample. Tests in which the dense electrolyte layer was placed in compression resulted in the highest strength values, while the samples were weakest when the electrolyte was placed in tension. In reduced samples, the anode support layer becomes a ceramic-metal composite and is therefore somewhat elastic while the electrolyte remains a brittle ceramic. The electrolyte-in-compression condition maximizes the mechanical performance of the coupon by placing the layers in their preferred stress state.

Figure 3.4 shows the box plots for the unreduced SOFC coupon samples. A Student's t-test was used to statically determine if the means of samples tested at different conditions were equal based on 95% confidence. Details on the use of the test are given in Appendix A.1. There is no discernible difference in the strength between the three sample types at each temperature. At elevated temperature there was a significant difference in the modulus of ASL only samples and samples with electrolyte in tension with a p-value of 0.0091. This difference was not present at room temperature. As the materials reach elevated temperature, small differences in elasticity become magnified due to different thermal effects on dense and porous layers.

Additionally, SEM analysis of the fractured half-cells showed very good adhesion between layers (Figures 3.5 and 3.6). Delamination is a common failure mode in

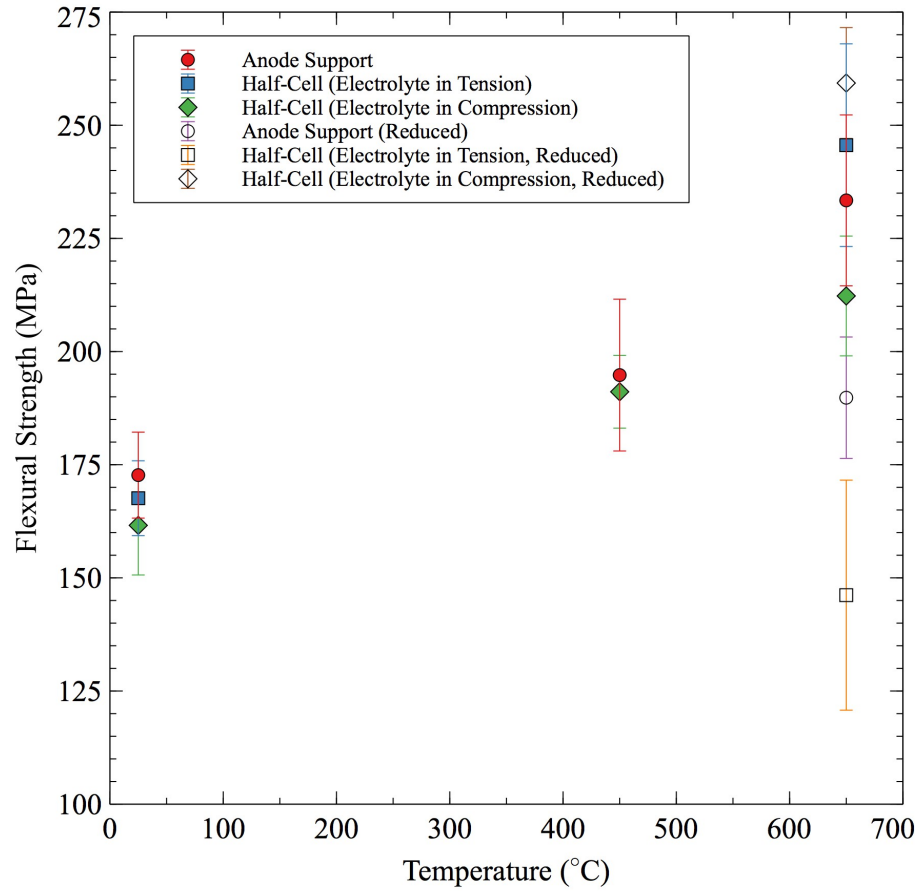


Figure 3.3: Temperature dependent strength of Ni-GDC anode supports and half-cells in both air (filled data points), and reducing atmosphere (3% H₂, balance Ar, hollow data points), tested in both “electrolyte-up” and “electrolyte-down” orientations resulting in the electrolyte layer experiencing tension and compression, respectively

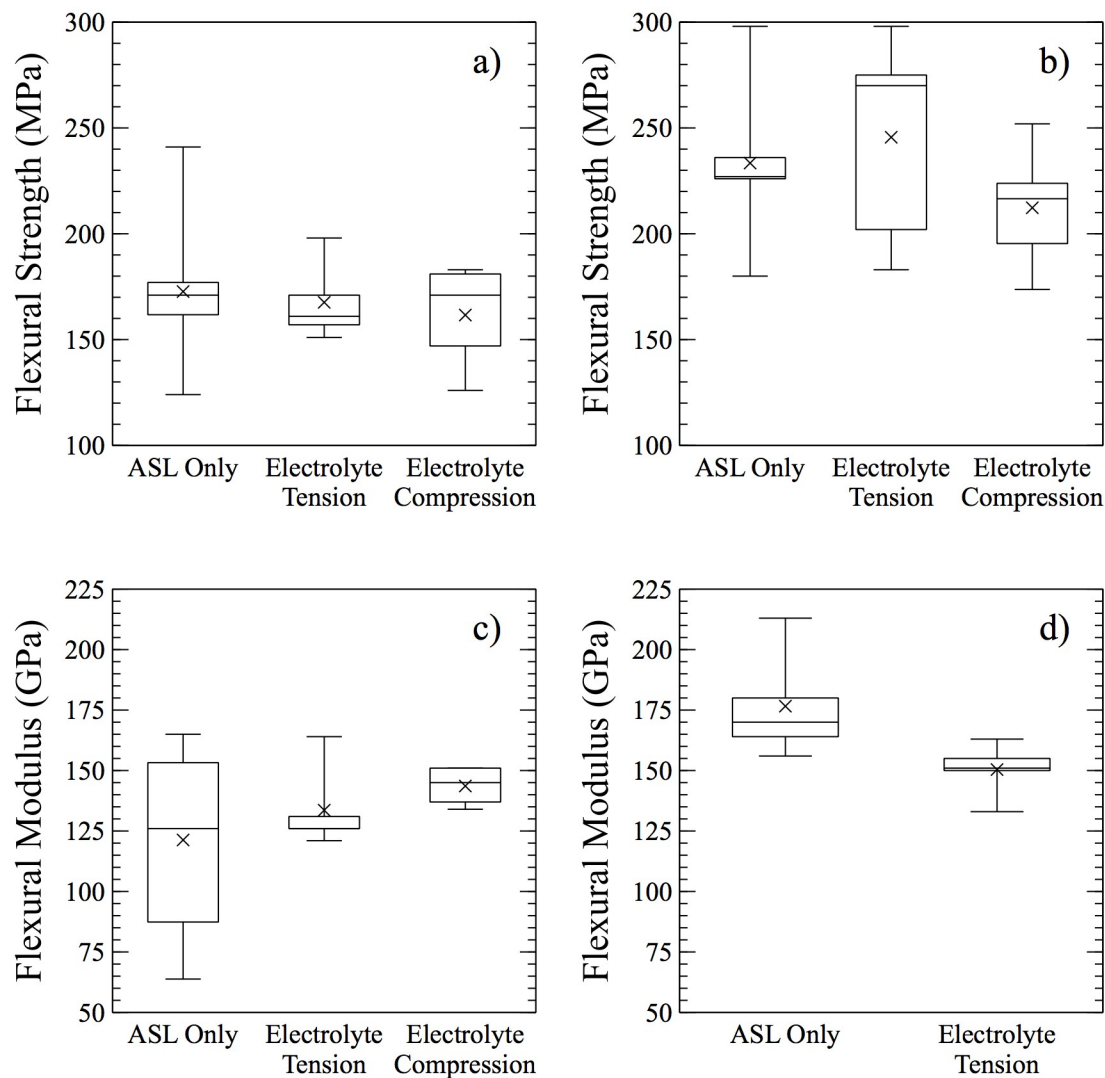


Figure 3.4: Flexural test measurements of coupons sample sets: a) strength at 25 °C b) strength at 650 °C c) modulus at 25 °C d) modulus at 650 °C

layered ceramics and one that would be particularly damaging to SOFCs due to resulting ionic conductivity loss between layers. [80] In the half-cell coupons, it was clear that the fracture plane contained mixed transgranular and intergranular fracture. Some grains were sheared through while others remained whole. The striations visible in Figures 3.5b and 3.6b are characteristic of fracture proceeding through a grain, while other grains remained whole.

3.2.3 Reduction and Strength

Mass loss of SOFC half-cell coupons exposed to reducing atmosphere at various elevated temperatures is shown in Figure 3.7. Mass loss is attributed to the reduction of NiO, used as a precursor in fabrication, to Ni metal, which serves as the catalyst for fuel oxidation and electronic conductor, and the reduction of ceria to $\text{CeO}_{2-\delta}$. Ni-GDC/GDC half cells showed the expected trend of increasing reduction rate at higher temperatures. Reduction curves were fit to an exponential decay and the summary of parameters is shown in Table 3.2. At 650 °C and 700 °C the reduction occurs very quickly, reaching steady state values after 18 hours. 550 °C showed a much slower mass loss than even 575 °C. At temperatures lower than 550 °C, the kinetics are slow enough to tolerate a brief exposure to oxygen without re-oxidizing the sample. Of note in the reduction is that each temperature appears to approach a different asymptote, showing that the amount of NiO and GDC reduced at steady state is dependent on the temperature of the cell. This will affect the mechanical properties of the cells as it changes both the porosity and amount of nickel metal in

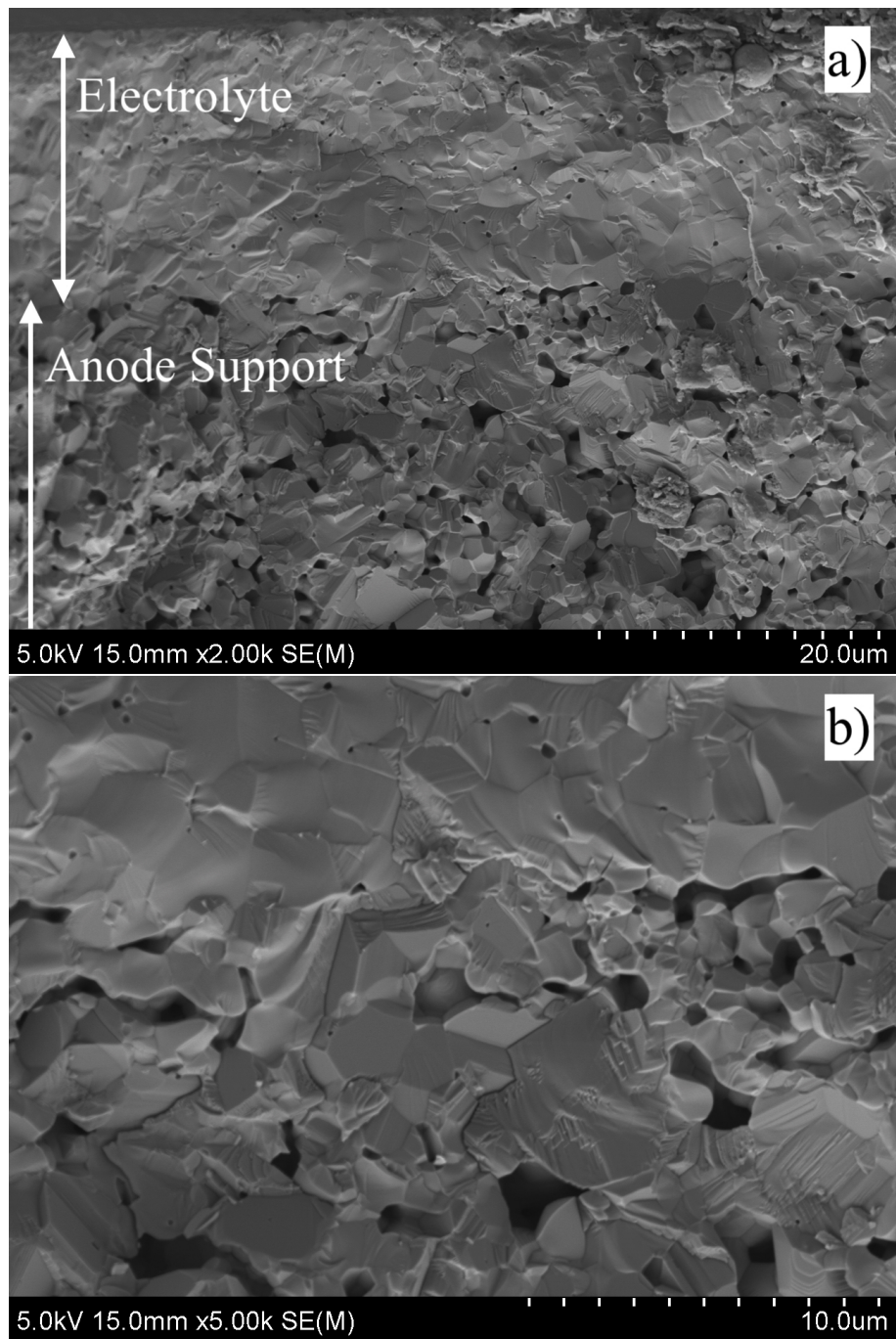


Figure 3.5: SEM micrographs of unreduced half-cell fracture surface tested in air at 25 °C at a) 2k magnification and b) 5k magnification

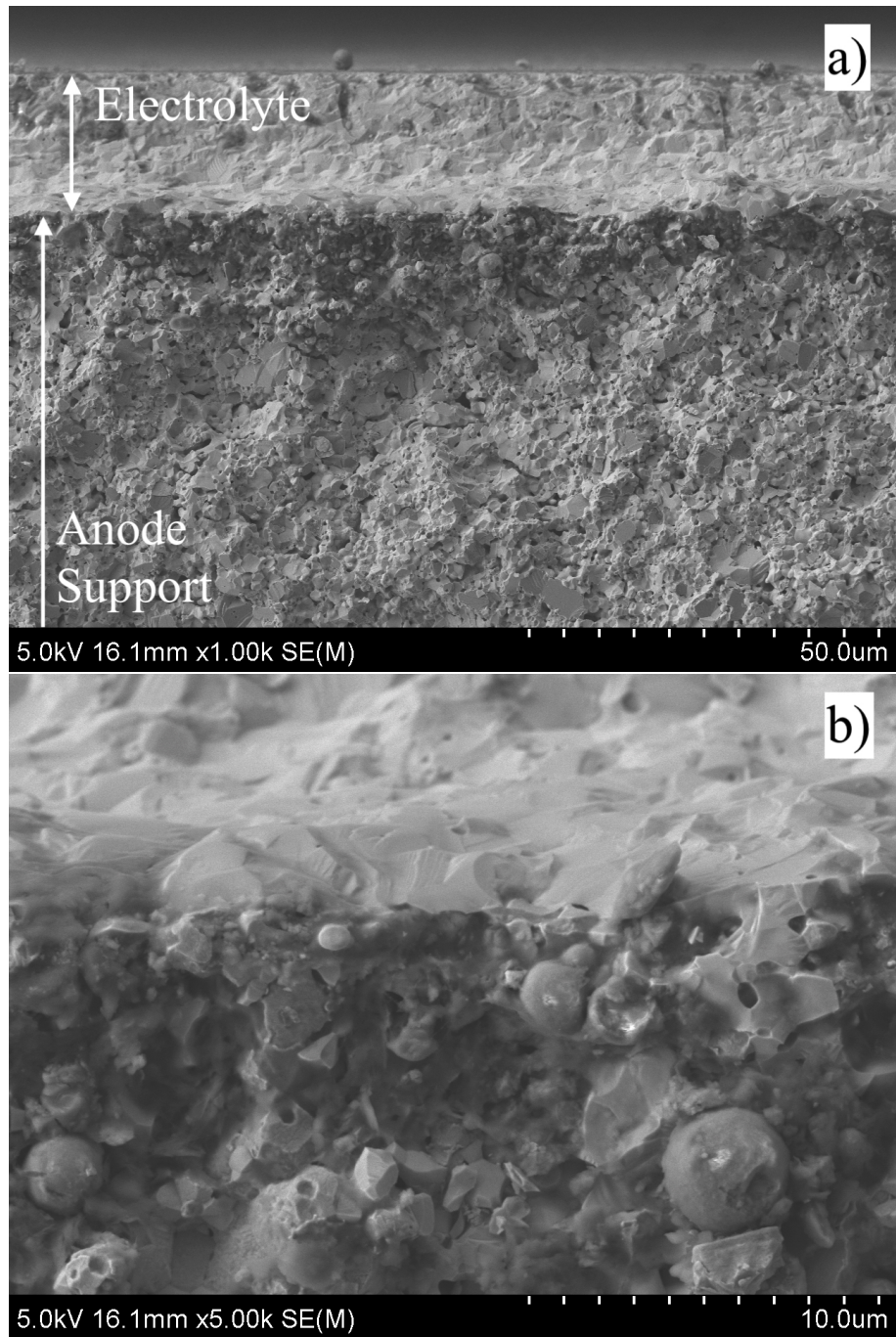


Figure 3.6: SEM micrographs of reduced half-cell fracture surface tested in reducing atmosphere at 650 °C at a) 1k magnification and b) 5k magnification

Table 3.2: Summary of fit parameters for reduction of NiO-GDC/GDC half-cell coupons under 3% H₂, 3% H₂O, 94% N₂ at different temperatures.

Temperature (°C)	Exponential Rate (h ⁻¹)	Asymptote (Mass %)
550	0.0463	89.78
575	0.135	89.09
600	0.182	88.36
650	0.512	87.75
750	0.821	87.87

the samples.

3.2.4 Reoxidation at Low Temperatures

Ni-GDC/GDC fuel cells are sensitive to re-oxidation once reduced. Re-oxidation causes fracture of cells due to the large volume difference between NiO and Ni. [66] Based on the results from the TGA, the reaction rates below 300 °C are sufficiently slow to allow for the exposure of a reduced cell to oxygen without detrimental results. [81] To confirm this, a sample was measured by TGA to ensure no mass gain during oxygen exposure and the strength of samples were tested to ensure there was no discernible difference between reduction methods.

For TGA analysis, a piece of a half cell was heated to 650 °C with a 10 °C min⁻¹ ramp rate and reduced. It was then cooled while still under reducing atmospheres. Once below 100 °C, it was exposed to simulated air (21% O₂) for 18 hours, placed back

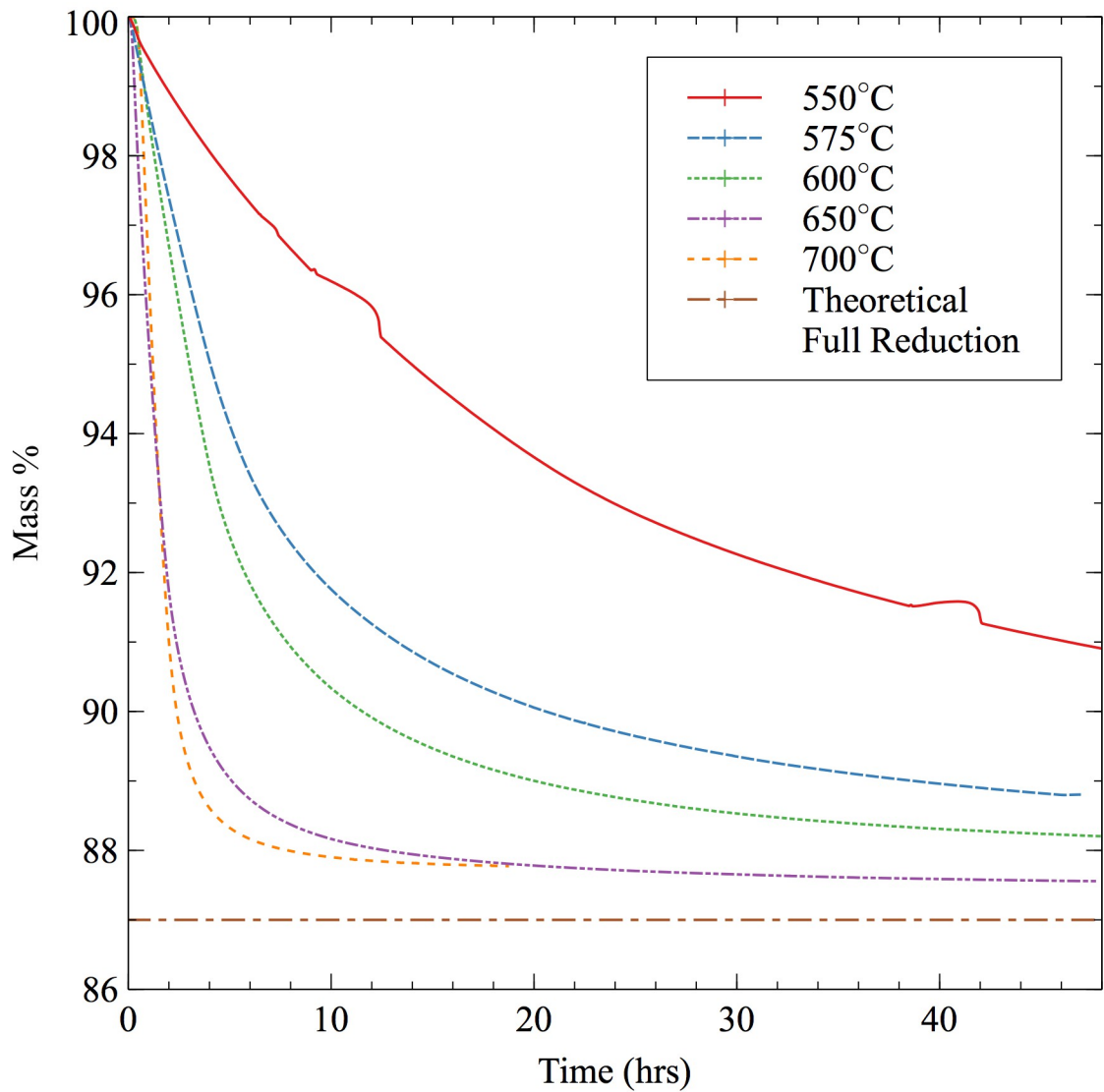


Figure 3.7: Thermogravimetric analysis curves for Ni-GDC/GDC half-cells showing mass loss over time at temperatures ranging from 550 °C to 750 °C in 3% H₂ 3% H₂O balance N₂, 50 sccm flow.

into reducing atmosphere, and heated back up to 650 °C. Figure 3.8 shows the change in mass overlaid onto the temperature and oxygen partial pressure experienced by the sample. Following this treatment, the cell showed no mass gain during the oxygen exposure and continued to reduce at the same rate as before once it was returned to the initial conditions. This shows that cells which are cooled appropriately do not re-oxidize and could be handled in between a batch reduction of cells, and their assembly into a stack configuration.

Box plots of flexural strength and modulus of the in-situ reduced and batch reduced coupons are shown in Figure 3.9. Mechanical strength of half-cell coupons which had been reduced in-situ with an 18 hour reduction time showed no difference in strength when compared with coupons which had been previously batch reduced, cooled, and reheated under reducing environments. Both of these sample types showed a dramatic decrease in strength and Young's modulus compared to the un-reduced samples, but no statistically significant difference between treatments. The decrease in strength and modulus is due to the increase in porosity and conversion of NiO to metallic nickel in the cells. The decrease in variation between measurements in reduced cells is likely due to the increased number of large voids that form during NiO reduction.

The statistical similarity of the properties of the samples reduced via each method indicates that planar, Ni-GDC/GDC based SOFC ASL and half-cells are able to be safely reduced, cooled, and handled in ambient conditions without leading to damaging re-oxidation of the nickel anode material. This resilience could enable some degree of large-batch reduction of cell anodes prior to SOFC stack assembly,

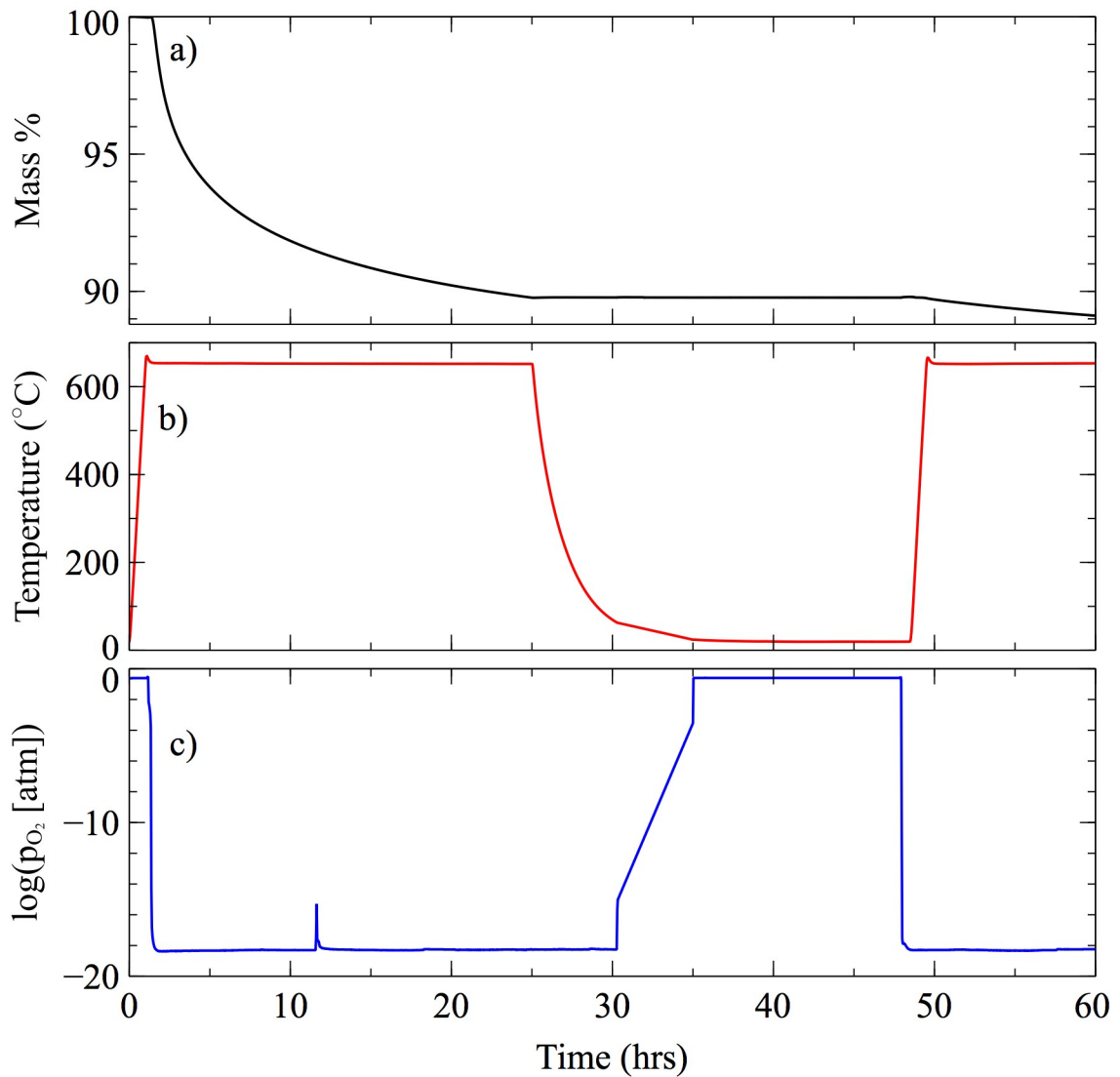


Figure 3.8: Thermogravimetric analysis of Ni-GDC/GDC half-cell showing no mass gain after reduction and exposure to room temperature and simulated air: a) Mass loss of interrupted reduction with exposure to ambient condition; b) Temperature of sample during cycle c) Oxygen partial pressure measured at the sample during cycle

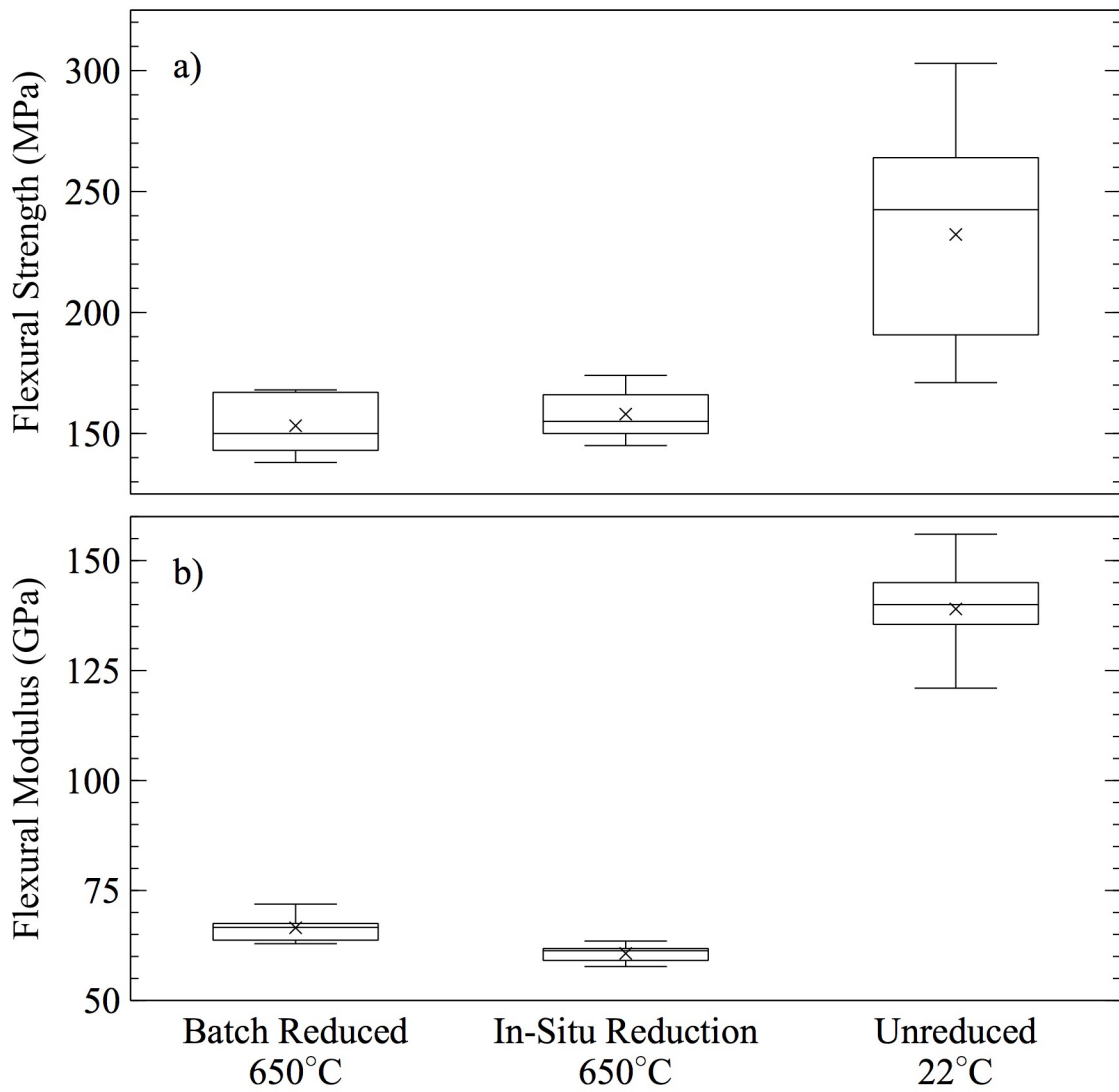


Figure 3.9: Flexural properties, a) strength and b) modulus, of Ni-GDC/GDC half-cell coupons after reduction via two different methods, compared to unreduced cells. Strength and modulus show a decrease upon reduction but no significant difference between methods.

leading to more rapid startup and a greater degree of sealing control.

3.3 Conclusions

A temperature and atmosphere controlled three-point bend fixture was designed and built for use in a universal testing machine. SOFC coupons and component materials were evaluated for flexural strength at room temperature and SOFC operating temperatures. In addition, the effects of porosity percent and pore geometry on flexural strength in GDC were investigated. Furthermore, the impact of temperature on the reduction rate of NiO in NiO-GDC SOFC anodes was examined along with the resilience to re-oxidation at ambient conditions of this SOFC component.

Pore geometry had a significant impact on the flexural strength of GDC, with spherical pores showing the greatest resistance to fracture. This supports the concept of pores acting as the new crack tip once a crack has advanced to the pore. Additionally, samples tested at 650 °C were stronger than those at room temperature. This is likely due to localized compressive stresses from thermal expansion of the material. This hypothesis is further supported by the results of testing NiO-GDC anode support coupons and half-cells. Coupons tested at 25 °C, 450 °C, and 650 °C displayed a linear strength dependence with temperature. There was no statistical difference in strength between anode support layers and half-cells composed of anode support and electrolyte at a given temperature in air. Half-cells in which NiO was reduced to Ni by exposure to H₂ at 650 °C displayed significant differences in strength when the electrolyte layer was subjected to compressive stress as opposed to

tensile stress. Placing the ceramic electrolyte in compression and the metal-ceramic composite anode in tension resulted in the highest strength.

The reduction temperature of NiO-GDC/GDC half-cells was shown to have an effect on the rate of NiO reduction and amount of NiO reduced. At lower temperatures, the oxidation rate of Ni-GDC is slow enough that the anode can be exposed to air for significant periods below 100 °C. Any re-oxidation, combined with the cooling and re-heating of a cell back to 650 °C, showed no effect on the mechanical properties when compared to cells which had been reduced in-situ at 650 °C. These results indicate that it is possible to reduce and cool cell components to an extent without any additional effects to mechanical properties, allowing for more flexibility during cell manufacturing, stack assembly, and with quality control screenings.

This work leads to three important conclusions for the mechanical properties of GDC-based SOFCs using Ni anodes. Porous GDC used in anode supported SOFCs should be fabricated such that the pore geometry is spherical as this maximizes energy required to advance a crack through the ceramic. Care should be taken in stack construction to ensure any out-of-plane cells are placed to compress the electrolyte and to place the reduced anode in tension so as to lower the chance of fracture. Finally, it is possible to reduce the anodes of Ni-GDC SOFCs and then handle them at ambient conditions for quality control and stack assembly. This will remove a degree of variability from the manufacture of cells and stacks.

Chapter 4: Defect Chemistry and Oxygen Non-Stoichiometry of Double Perovskite $\text{SrFe}_{0.2}\text{Co}_{0.4}\text{Mo}_{0.4}\text{O}_{3-\delta}$

4.1 Introduction

SFCM is a new material that is of particular interest because of its high conductivity and stability in hydrocarbon fuels. [41] SFCM takes advantage of the perovskite structure and multivalent cations similar to SMM, but the combination of both Fe and Co further increase the conductivity of the material. It has been shown that an SOFC using SFCM as an anode support material is redox stable up to 30 cycles at 600 °C between $\text{H}_2/3\%\text{H}_2\text{O}$ and nitrogen. [42, 43]

This work expands upon the fundamental knowledge of SFCM and aims to understand the defect chemistry which leads to its high conductivity as an MIEC. XRD and Rietveld refinement show the phase stability and lattice parameter changes of SFCM across pO_2 s. Electrical conductivity is measured as a function of pO_2 to determine changes electrical conductivity types. TPD spectroscopy was used to characterize the oxygen desorption as it occurs from the lattice. The non-stoichiometry of SFCM was measured under oxidizing and reducing environments at various temperatures via thermogravimetric analysis and a defect equilibrium model

and diagram is proposed from the data with results compared to SMM and other perovskite materials.

4.2 Results and Discussion

4.2.1 Phase Purity and Chemical Expansion

The XRD patterns obtained after reduction in 1.9% H₂, 2.9% H₂O at 600 °C and oxidation in pure oxygen at 600 °C, in addition to the fresh as synthesized powder and the pattern obtained from Rietveld refinement, are presented in Figure 4.1a. A tetragonal, unordered B-site, double perovskite structure was used as a starting point for Rietveld refinement based on the structures of Sr₂CoMoO₆, Sr₂NiMoO₆ and Sr₂Fe_{0.75}Co_{0.25}MoO₆. [38, 82] Results from the Rietveld refinement calculations are given in Table 4.1. The refined unit cell is presented in Figure 4.1b and was used to create the theoretical XRD pattern for comparison.

SFCM proved to be stable under reducing conditions, being pure phase based on the Rietveld refinement. Overall phase purity remains at greater than 76% as synthesized, 85% under oxidizing conditions and at 100% after reduction. Sr₂Co_{1.2}Mo_{0.8}O₆ was found in SFCM under ambient and oxidizing conditions. This secondary phase reversibly disappears when returning to reducing conditions after oxidation.

Changes in SFCM's lattice parameters are attributed to the oxidation states of the B-site cations and the concentration of vacancies in the sample after exposure to different p_{O₂}s. Reduction of SFCM from an as synthesized state causes a 0.025% decrease in *a* and the volume of the unit cell and a 0.025% increase in *c*. These are

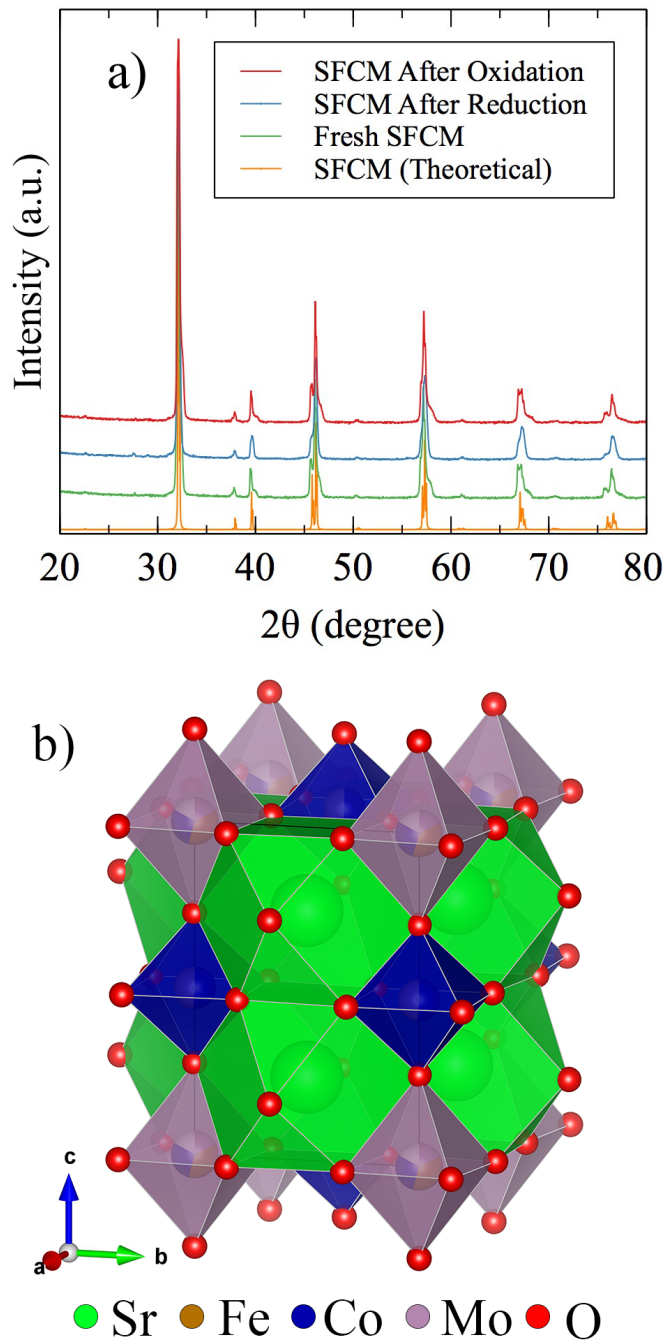


Figure 4.1: a) Powder XRD patterns of SFCM samples taken after synthesis, reduction, and oxidation compared to pure phase SFCM diffraction pattern. b) Crystal structure of unordered double perovskite SFCM.

Table 4.1: Refinement results of SFCM before and after exposure to reducing and oxidizing environments

Condition	Oxidized	Fresh	Reduced
Space Group	I 4 \overline{m}	I 4 \overline{m}	I 4 \overline{m}
a (Å)	5.5636(2)	5.5558(3)	5.5544(2)
c (Å)	7.9310(2)	7.9184(3)	7.9204(2)
Volume (Å ³)	245.49	244.41	244.35
Sr-O1 (Å)	2.794	2.790	2.790
Sr-O2 (Å)	2.789	2.785	2.784
M1-O1 (Å)	1.993	1.990	1.990
M1-O2 (Å)	1.782	1.780	1.780
M2-O1 (Å)	1.950	1.948	1.947
M2-O2 (Å)	2.183	2.180	2.180
Phase Purity (% SFCM)	85.24	76.08	100.0
R _w (%)	14.277	15.519	17.324

the result of the bond lengths between strontium and oxygen in site 2 (Sr-O2) and the distance between metal site 2 and oxygen site 1 (M2-O1) decreasing. Oxidizing the SFCM results in a 0.14% increase in a and a 0.16% increase in c resulting an 0.44% increase in cell volume. This is the result of all bond lengths increasing by 0.002 to 0.004 Å. These small lattice parameter shifts are in line with the general nature of perovskites to display little to no change due to chemical expansion. [53] Additionally, when changes do occur, perovskites have been shown to have anisotropic chemical expansion, as such with $\text{Sr}_2\text{Fe}_{1.5}\text{Mo}_{0.5}\text{O}_6$ (SFM) where a increases upon reduction while c decreases. [83] In summary, SFCM shows very little change to lattice parameters as a result of changing metal oxidation states or vacancy creation as it undergoes reduction or oxidation.

4.2.2 Conductivity

SFCM has a conductivity dependence typical of MIEC conductors, as shown in Figure 4.2. At high p_{O_2} ranges ($10^{-1.5}$ atm to 1 atm) it shows p-type conductivity, where conductivity increases with p_{O_2} . Down to 10^{-1} atm, the change in conductivity is linear with a slope of 0.089 (log-log scale). Below 10^{-1} atm the slope changes away from the previous trend, suggesting a change in the predominant charge carrier. At low p_{O_2} ranges (10^{-24} atm to 10^{-19} atm) the conductivity behaves linearly with n-type conductivity, increasing at lower p_{O_2} , with a slope of -0.11 (log-log scale). The sample measured in this work exhibited a lower conductivity than that reported in previous work (2 S/cm compared to 30 S/cm at 600 °C). [41] This difference is

likely due to sample preparation creating additional porosity, reducing the absolute conductivity, but the trend with p_{O_2} remains consistent.

Based on the slopes in the high p_{O_2} region, at least two defect regimes exist in that area transitioning near 10^{-1} atm. Both high and low p_{O_2} regions have slopes much lower than $+1/4$ or $-1/4$ respectively, which indicates that the relationship between electronic charge carriers and oxygen is dependent of the other defect species in the material. In fact, the lower than $1/4$ slope suggests that the electronic charge carries are taken up by the other species, decreasing the expected number based on p_{O_2} change. At low p_{O_2} , n-type conductivity is promoted by the generation of oxygen vacancies, freeing electrons as negative electronic charge carriers to maintain charge balance. Some of these electrons are consumed by the reduction of B-site metals to lower oxidation states. At high p_{O_2} , oxygen vacancies are filled and B-site metals oxidize, consuming electrons and allowing for the creation of holes, promoting p-type conductivity. The different slopes between high and low p_{O_2} are the result of different defect species interacting with the electronic carriers at different points in the reduction.

4.2.3 Temperature Programed Desorption

TPD was performed in conjunction with TGA to determine the extent of oxygen desorption from SFCM. Figure 4.3 presents the data from the TGA on top with the mass and rate of mass change, while the 32 m/z signal from oxygen in the mass spectrometer is on bottom. The cyclic noise present in both mass and

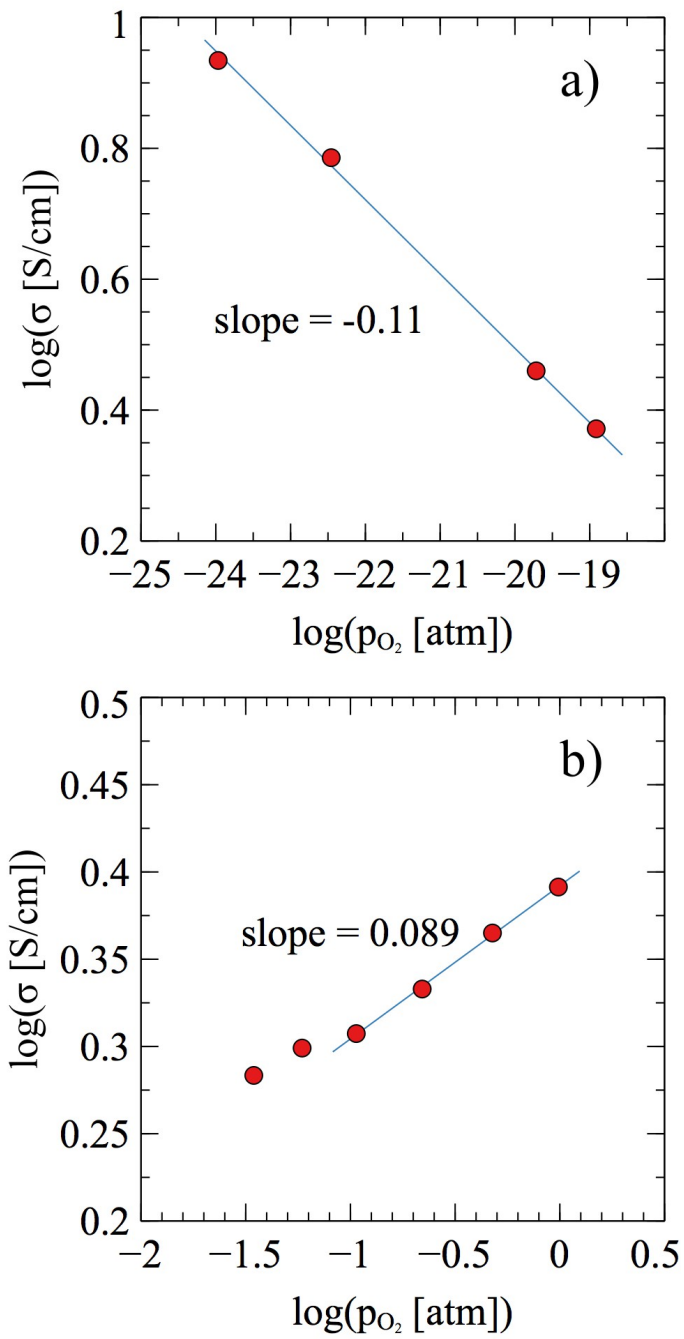


Figure 4.2: Total conductivity as p_{O_2} changes under a) reducing and b) oxidizing conditions at 600 °C.

MS signals is due to temperature fluctuations as a result of an improperly tuned PID controller on the TGA furnace, but the noise remained much lower than the measured signal. The rate of mass loss matches the oxygen signal from the MS, confirming that oxygen is generated from SFCM when heated under N₂ and is the cause for mass loss in the sample. SFCM shows two maxima for the rate of oxygen loss during heating. The first, α , occurs at 405 °C with the second peak, β , occurring near 800 °C. The MS monitored for other species, such as carbon and water, but no significant amounts were observed.

Perovskite materials have oxygen desorption classified based on the temperature at which it occurs. Low temperature desorption (referred to as α), occurs due to the reduction of metals and desorption of oxygen near the surface. High temperature desorption (referred to as β), takes place when oxygen is able to diffuse through the bulk and be released. [84] SFCM shows both α and β desorption, indicating that both the surface and lattice can generate oxygen vacancies due to the reduction of the different B-site cations and that those vacancies are mobile to move from the bulk to the surface. SMM shows only β desorption above 800 °C, while SFM has α desorption from 400 °C to 800 °C and Sr₂CoMoO₆ (SCM) desorbs starting below 400 °C. [85, 86] In the case of SFM and SCM, the use of the multivalent Fe or Co allows for reduction at a lower temperature than SMM. For SFCM, the same effect is seen through the combined use of Fe and Co. This demonstrates SFCM's ability to begin to create oxygen vacancies at 400 °C and exchange oxygen with the bulk lattice starting as low as 450 °C and peaking near 800 °C.

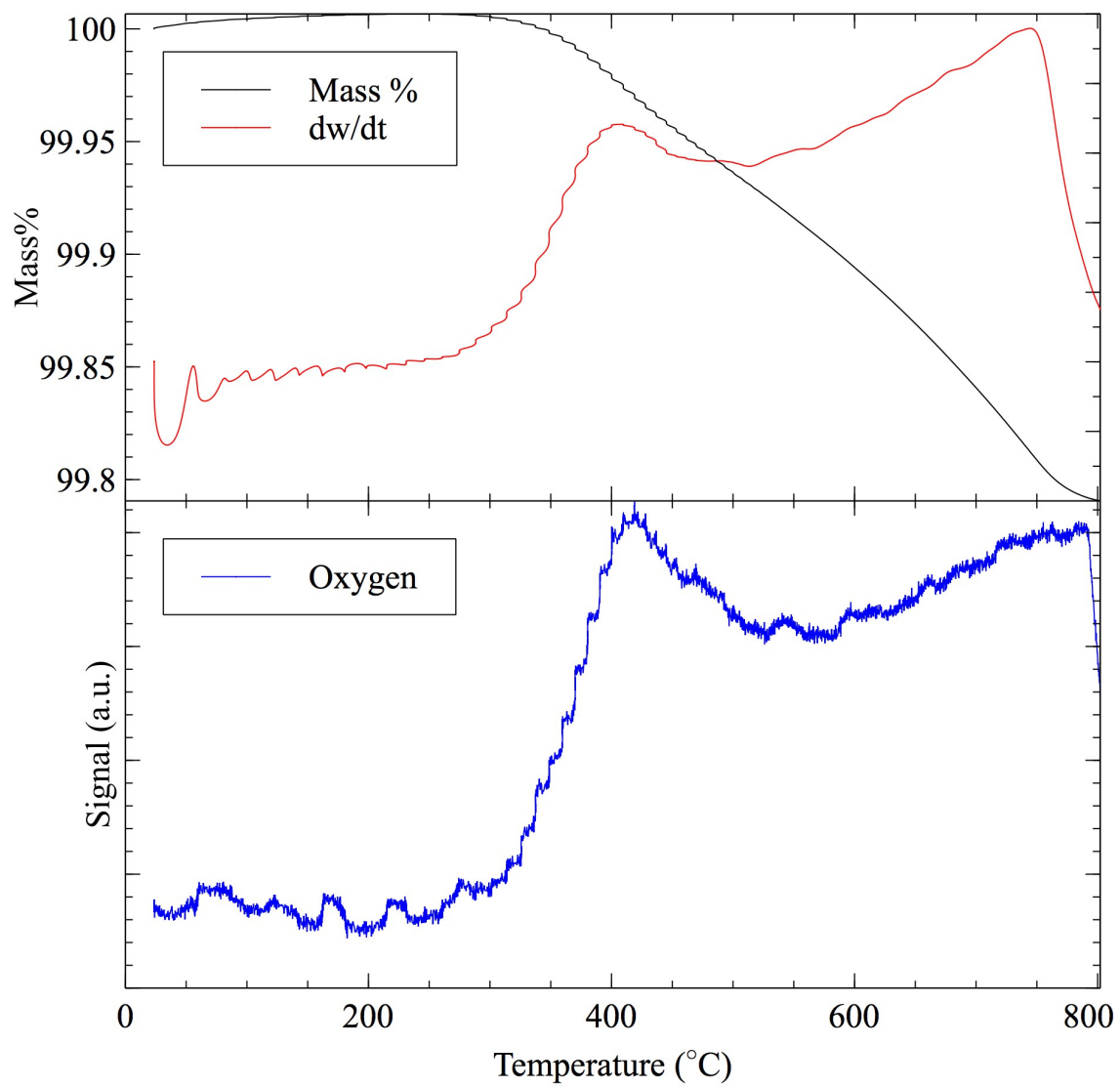


Figure 4.3: Temperature programmed desorption of oxygen in SFCM with mass loss from TGA (top) and oxygen desorption from MS (bottom) as it is heated to 800 °C in N₂

4.2.4 Oxygen Non-Stoichiometry

Oxygen non-stoichiometry and oxygen vacancy concentrations are shown in Figure 4.4 at 600 °C for high and low p_{O_2} regions. At high p_{O_2} , SFCM has two linear regions, changing between them near $10^{-0.75}$ atm. The transition between regions in oxygen stoichiometry occurs at a similar p_{O_2} to where the conductivity changes in Figure 4.2. This change is the result of a change in defect regime regions. In the low p_{O_2} region, a linear trend occurs down until 10^{-21} atm where the non-stoichiometry rate increases. Due to the pure phase XRD under reducing conditions, it is not likely that the increase in non-stoichiometry is due to phase decomposition and instead is a change in regimes where more oxygen vacancies are present.

SFCM shows similar trends in non-stoichiometry to SMM and SFM, but with the added complexity expected from the additional B-site species. SMM approaches a plateau in oxygen content as it reached 1 atm of oxygen the same as SFCM but possesses a constant slope of -1/6 when plotted on a log-log scale. [87] In comparison, SFCM has multiple slopes associated with the degree of vacancy formation, as shown in Figures 4.4c and 4.4d. These different slopes can be attributed to the reduction of the three different B-site cations at different p_{O_2} . As an oxygen vacancy forms, the electrons required to maintain charge balance can be accommodated by the reduction of Fe, Co, or Mo, each with an independent equilibrium constant, whereas SMM only has Mo reduction to accommodate electrons from oxygen vacancy generation. The high slopes of Figure 4.4d show how SFCM can generate more oxygen vacancies at lower p_{O_2} because of the Fe and Co cations. SFM and SMM show similar amounts

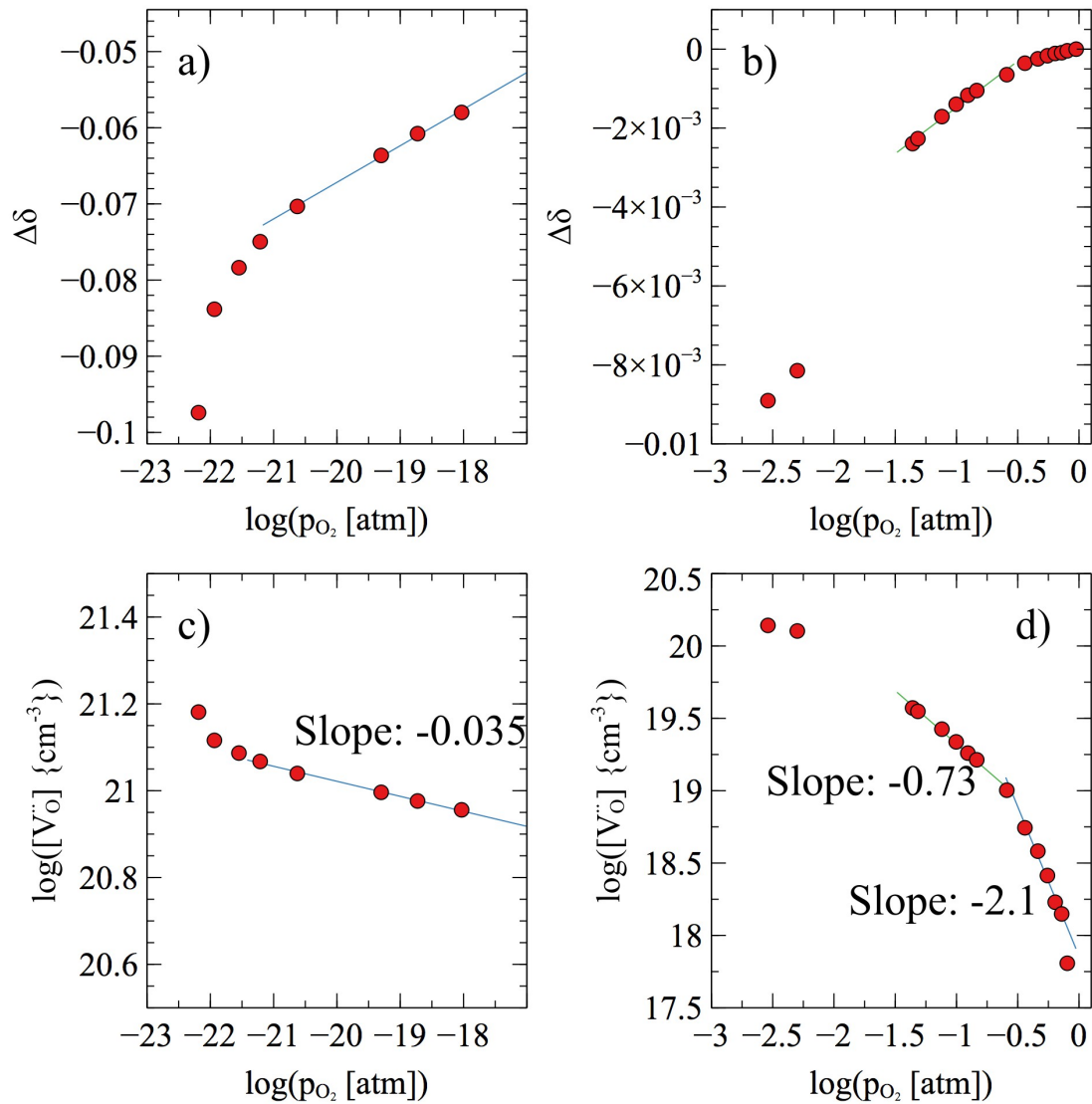


Figure 4.4: Non-stoichiometry (top) and corresponding oxygen vacancy concentration (bottom) of SFCM under oxidizing conditions (right) and reducing conditions (left) at 600 °C

of non-stoichiometry at the same p_{O_2} but at 1000 °C. [88] SFCM shows almost twice the non-stoichiometry at a much lower temperature of 600 °C. SFCM’s ability to create vacancies at higher p_{O_2} results in a larger accumulated vacancy concentration at low p_{O_2} .

TGA non-stoichiometry measurements were performed on the same sample at 400 °C, 500 °C, and 600 °C which are in the low temperature-SOFC range. Figure 4.5 shows the non-stoichiometry measurements for the sample tested at three temperatures in the low p_{O_2} (a) and high p_{O_2} (b) regions. As expected, lowering the temperature reduces the non-stoichiometry at a given p_{O_2} and decreases the p_{O_2} at which transitions between regimes occur. At 400 °C, oxygen vacancy formation decreases considerably compared to 500 °C and 600 °C. This aligns with the results of the TPD (Figure 4.3) where SFCM does not start desorbing oxygen until 350 °C to 400 °C, and then only from the surface.

4.2.5 Defect Equilibrium Model and Diagram

To best understand what is occurring in SFCM, a defect equilibrium diagram and model need to be created to relate the changes in conductivity and non-stoichiometry to the concentration of the various defects present in the material. Defect reactions with their corresponding equilibrium equations are given in Equations 4.1–4.4, which use Kröger–Vink notation, where a species is denoted by the site it sits on (subscript) and the relative charge to the site’s expected valency (superscript). For example, V_O^{2+} is a vacancy in an oxygen site with a 2+ charge and

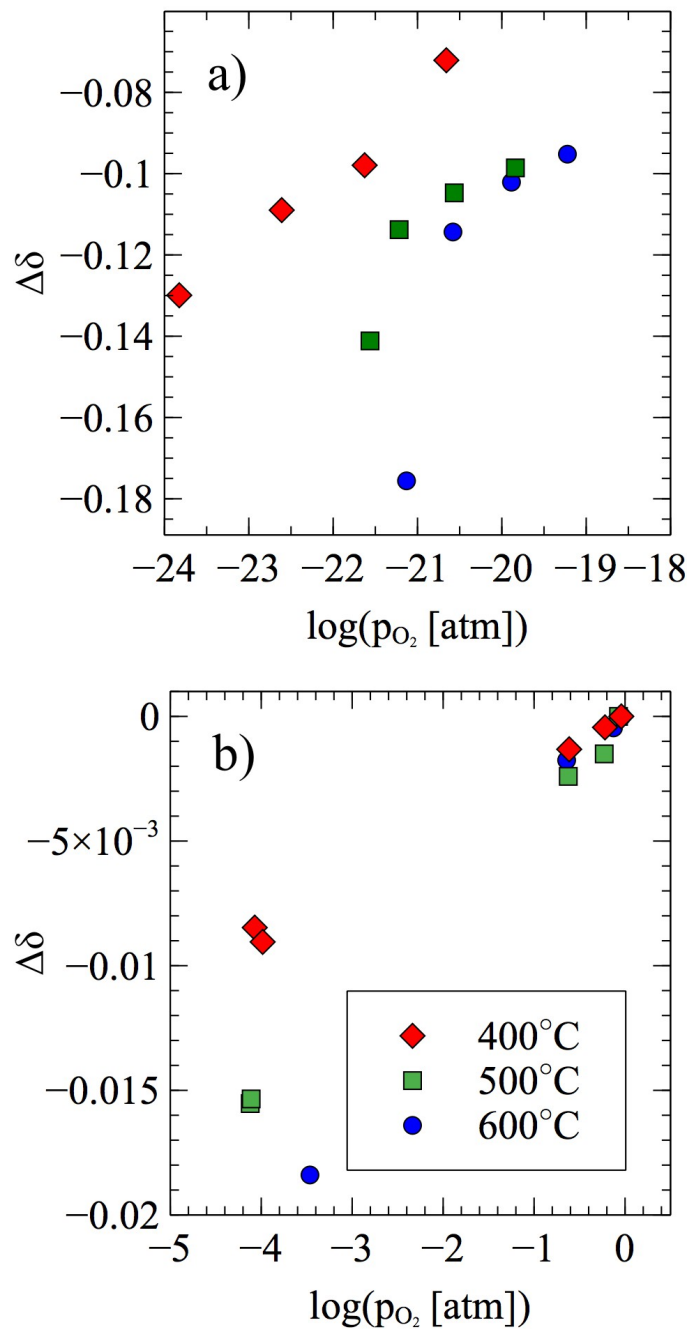
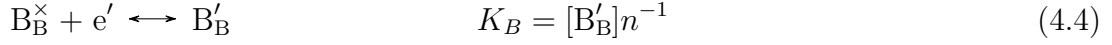
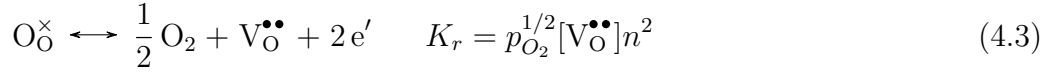
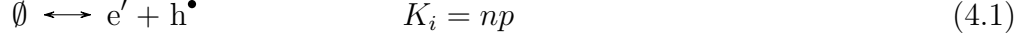


Figure 4.5: Non-stoichiometry of SFCM as p_{O_2} changes at 400°C , 500°C , and 600°C

B'_B is a B-site metal in a B-site with a 1 $-$ charge. K represents the equilibrium, or mass-action, constant for the reaction. To simplify the set of equations, Equation 4.4 represents the combined reduction of any B-site cation (Fe, Co, or Mo). β is the ratio of A-site vacancies to B-site vacancies from Schottky defects.



The Duncan-Wachsman approach allows for the accurate solution of defect equations across p_{O_2} regions using dominant defect triads, compared to the dominant defect pairs of the Brouwer approach which lead to inaccurate results near transition regions. [89] The Duncan-Wachsman approach is needed in this work to model the defect equilibria because the measured p_{O_2} range crosses various Brouwer regions, as indicated by the non-linearity of Figure 4.4c. Using this method, Equations 4.1–4.4 can be solved to give models of the defect concentrations across p_{O_2} . Due to the fact that impurity phases form under oxidizing conditions, only the pure phase, reducing p_{O_2} were solved for. Table 4.2 gives the resulting equations from the Duncan-Wachsman approach for the defect concentrations at these p_{O_2} . To allow for the solution of the equations, it was assumed that all B-site metals will have already reduced to their maximum potential, that is $[B'_B]$ is constant, in the p_{O_2} range of interest.

Using the TGA and conductivity data with the equations given in Table 4.2, the

Table 4.2: Equations for defect equilibrium under reducing conditions

Defect	Equation
n	$K_r^{\frac{1}{2}} p_{O_2}^{-\frac{1}{4}} \left(\frac{3}{4} K_r^{\frac{1}{2}} p_{O_2}^{-\frac{1}{4}} + \left(\frac{1}{2} [B'_B] \right)^{\frac{3}{2}} \right)^{-\frac{1}{3}}$
p	$K_i K_r^{-\frac{1}{2}} p_{O_2}^{\frac{1}{4}} \left(\frac{3}{4} K_r^{\frac{1}{2}} p_{O_2}^{-\frac{1}{4}} + \left(\frac{1}{2} [B'_B] \right)^{\frac{3}{2}} \right)^{\frac{1}{3}}$
[V_O^{••}]	$\left(\frac{3}{4} K_r^{\frac{1}{2}} p_{O_2}^{-\frac{1}{4}} + \left(\frac{1}{2} [B'_B] \right)^{\frac{3}{2}} \right)^{\frac{2}{3}}$
[V_A'']	$\beta K_s^{\frac{1}{\beta+1}} \left(\frac{3}{4} K_r^{\frac{1}{2}} p_{O_2}^{-\frac{1}{4}} + \left(\frac{1}{2} [B'_B] \right)^{\frac{3}{2}} \right)^{-\frac{2}{\beta+1}}$
[V_B''']	$K_s^{\frac{1}{\beta+1}} \left(\frac{3}{4} K_r^{\frac{1}{2}} p_{O_2}^{-\frac{1}{4}} + \left(\frac{1}{2} [B'_B] \right)^{\frac{3}{2}} \right)^{-\frac{2}{\beta+1}}$
[B'_B]	Constant

reaction equilibrium constants can be fitted to obtain a general defect equilibrium diagram for reducing p_{O_2} as shown in Figure 4.6a. The electron mobility was calculated from the fitted data at 600 °C to be $0.0408 \text{ cm}^2 \text{ V}^{-1} \text{ s}^{-1}$, which is within the range for small polaron defects for SMM. [87] By fitting and plotting the values of K_r from various temperatures (Figure 4.6b), the enthalpy of formation for oxygen vacancies was found to be 39.1 kJ mol^{-1} in SFCM under reducing conditions.

While the fit for the oxygen vacancy concentration in Figure 4.6a fits well, the model predicts a steeper slope for the concentration of electrons. The cause of this is from the assumption that $[B'_B]$ is a constant, made while solving the defect reaction equations. In reality, while most B-site metals will have reduced, a portion will still be reducing at the low p_{O_2} , decreasing the overall number of conduction electrons, and reducing the p_{O_2} dependence of n. At low p_{O_2} both the

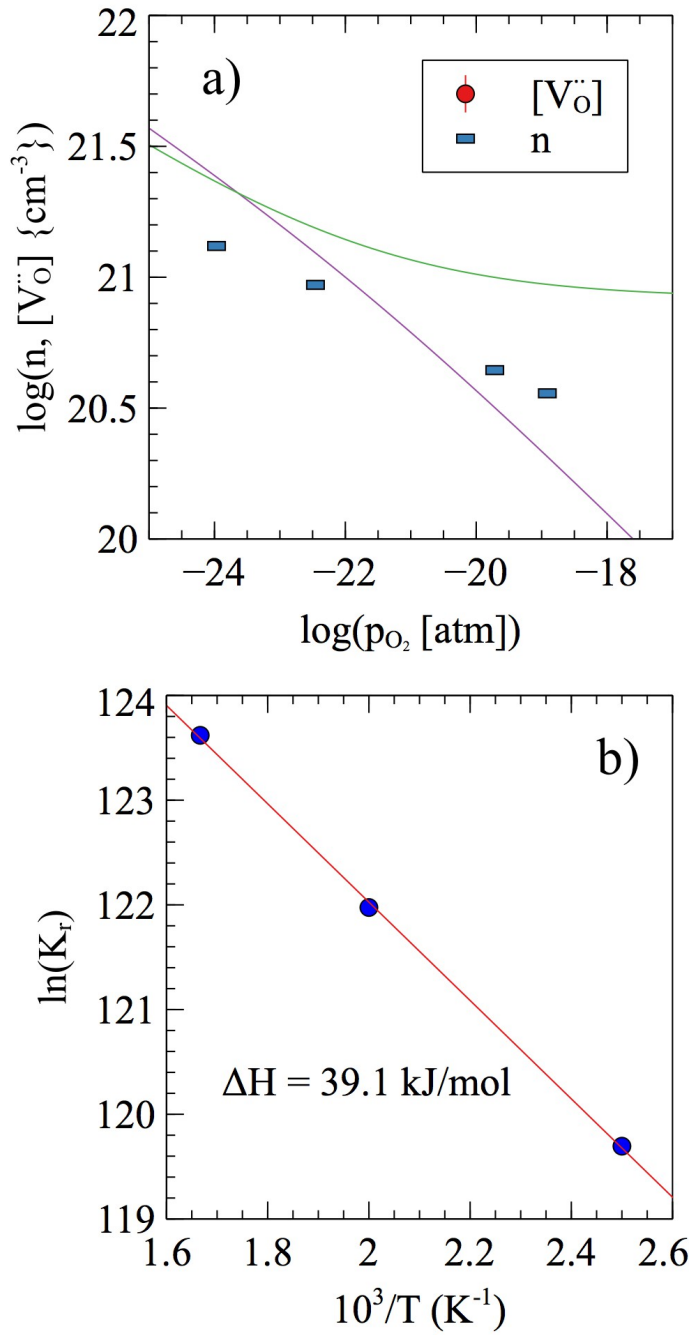


Figure 4.6: Oxygen vacancy and electronic defects in SFCM based on conductivity and TGA non-stoichiometry

concentrations of electrons and oxygen vacancies are on the same order of magnitude promoting mixed conduction. SFCM has an enthalpy of formation lower than that of comparable materials. SFM and SMM have much higher enthalpies of 253 kJ mol^{-1} and 110 kJ mol^{-1} respectively. [87, 88] $\text{SrFeO}_{3-\delta}$ has a more comparable, but still greater, enthalpy of 80 kJ mol^{-1} . [90] This low enthalpy of formation of oxygen vacancies in SFCM allows for a greater range of non-stoichiometry and thus SFCM's high performance.

4.3 Conclusions

SFCM has potential as an electrode material in a number of electrochemical device applications. Specifically, it has a potential to replace nickel-based anodes in SOFCs due to its high conductivity and redox stability, creating an all-ceramic anode. SFCM forms impurity phases when heated at $600\text{ }^\circ\text{C}$ under oxidizing environments but becomes pure phase with reduction. It also exhibits very small chemical expansion with changing p_{O_2} , in line with its perovskite structure. SFCM is an improvement over previous double perovskite materials because of high conductivity at temperatures below $600\text{ }^\circ\text{C}$. This is in part because SFCM supports the formation of oxygen vacancies at both surface and lattice positions shown by overlapping α and β oxygen desorption, starting as low at $350\text{ }^\circ\text{C}$ and continuing up until above $800\text{ }^\circ\text{C}$. Oxygen vacancies form more rapidly than other MIEC materials with decreasing p_{O_2} as combination of B-site cations enables reduction though a large range of p_{O_2} resulting in a low enthalpy of formation for oxygen vacancies at 39.1 kJ mol^{-1} .

Proposed defect equilibrium equations were given for the low p_{O_2} range and are supported by thermogravimetric and conductivity measurements for the complex system. Thermogravimetry at lower temperatures demonstrated SFCM's activity until 400 °C at which the amount of oxygen vacancy formation slows dramatically.

Chapter 5: Flexural Strength and Flaw Distributions of
 $\text{SrFe}_{0.2}\text{Co}_{0.4}\text{Mo}_{0.4}\text{O}_{3-\delta}$ Based Ceramic-Supports for
Solid-Oxide Fuel Cells at Operating Conditions

5.1 Introduction

This work characterizes the changes which occur in fracture toughness and flaw distributions of SFCM, SFCM-GDC ASL, and SFCM-GDC/GDC half-cells when exposed to oxidizing and reducing conditions up to 600 °C by use of flexural testing and Weibull analysis. Additionally, electrical conductivity, thermogravimetric analysis, and thermal expansion are used to determine the causes for changes in mechanical properties under these conditions.

5.2 Results and Discussion

5.2.1 Redox Cycling Stability

SFCM has a high initial conductivity of 35 S/cm but decreases after 3 cycles to 19 S/cm and again at 9 cycles, shown in Figure 5.1a. The addition of GDC to create a SFCM-GDC composite decreases the initial conductivity to 15 S/cm. At

4 cycles, SFCM-GDC decreases conductivity and stabilizes to 8 S/cm for 19 cycles. The addition of the GDC improved the redox cycling stability by providing a very stable, contiguous framework for the SFCM. [13, 54, 91]

Figure 5.1b shows the mass loss of SFCM-GDC as it is reduced in 3% humidified H₂. For comparison, another popular anode material, nickel oxide GDC, is plotted along with it. The reduction of SFCM-GDC results in a less than 1% reduction of mass from the formation of oxygen vacancies in the SFCM and GDC, and it reaches steady state in under two hours. NiO-GDC on the other hand loses a large amount of mass from the reduction and phase change of NiO to Ni metal, taking over 30 hours to reach steady state.

Further cycling of SFCM in the TGA was performed and results are given in Figure 5.2, with 5.2a showing the mass loss of SFCM with time as it is cycled between air and hydrogen, and 5.2b being a summary of the total mass changes that occur with each cycle. With each cycle, less than 1% total mass change is observed. Reduction occurs over a time period of five hours while oxidation happens at a faster rate, approximately one hour. Fitting the reduction and oxidation to exponential functions gives a biexponential with decay rates of 0.438 and 27.89 for reduction and an oxidation rate of 2.90. Previous experiments have shown that SFCM generates an impurity phase of Sr₂Co_{1.2}Mo_{0.8}O₆ under ambient and oxidizing conditions. [92] This impurity phase does not contribute to the gain or loss of oxygen as seen in the TGA. Sr₂Co_{1.2}Mo_{0.8}O₆ has a cubic structure compared to SFCM's tetragonal structure, leading to additional stress and strain created by its generation impacting the mechanical and electrical properties between oxidizing and reducing

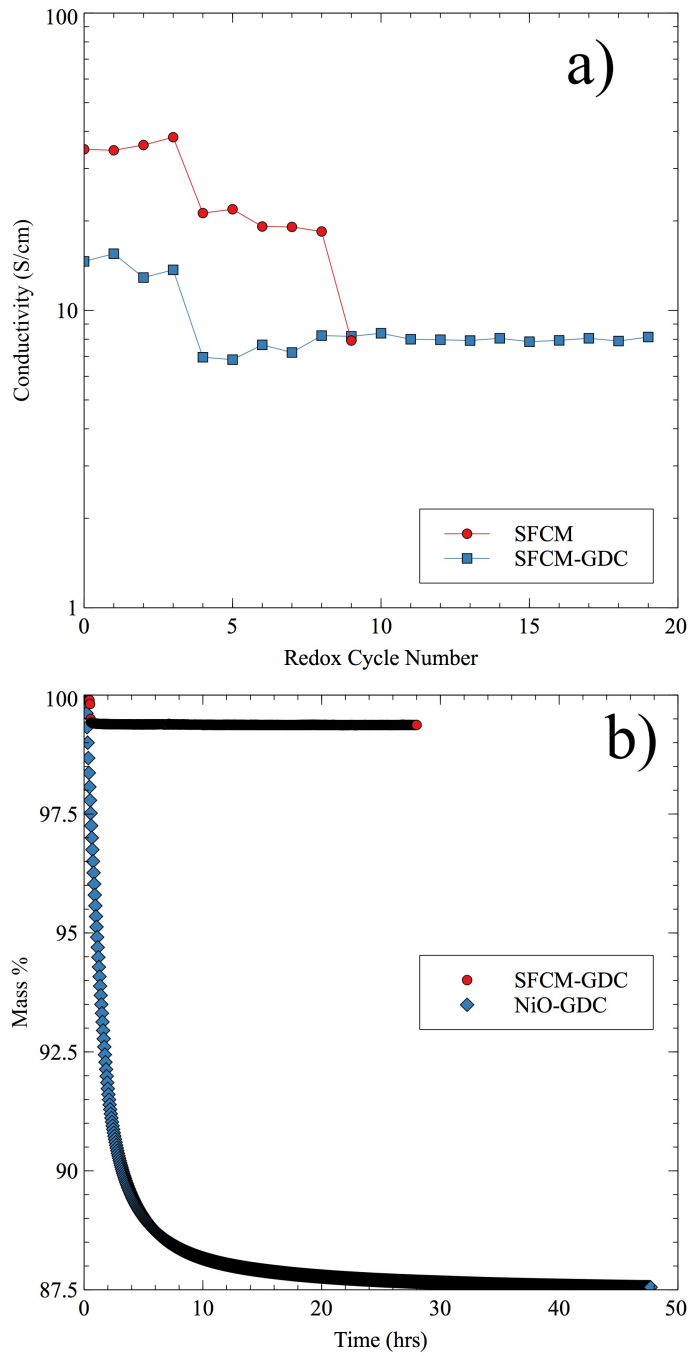


Figure 5.1: a) DC conductivity of SFCM and SFCM-GDC after cycling at 650 °C between 10% H₂ in N₂ and air. b) Mass loss of SFCM-GDC and NiO-GDC during reduction in 3% H₂/3% H₂O in N₂ at 650 °C.

environments.

5.2.2 Fracture Toughness

Fracture toughness was found to be $(0.124 \pm 0.023) \text{ MPa}\sqrt{\text{m}}$ at room temperature, increasing with temperature up to 600°C , as shown in Figure 5.3a. From room temperature to 500°C , the rate of increase in K_{Ic} is low at $4.3 \times 10^{-5} \text{ MPa}\sqrt{\text{m}}/\text{ }^\circ\text{C}$. From 500°C to 600°C , the fracture toughness increases by 90%. The increase in fracture toughness is a result of the thermal expansion of the material. During process of creating the bar, the sample was cooled from 1340°C to room temperature. This cooling and associated contraction induces stresses in the bar sample, which combine with the stresses added during testing to fracture the sample. As the sample is heated, the residual stresses are relaxed, increasing the amount of stress which must be applied externally to cause the bar to fracture. Any change in fracture toughness due to the weakening of bonds is masked by this effect. The increase in fracture toughness from 500°C to 600°C matches the temperature where the rate of thermal expansion also increases, as shown in Figure 5.3b.

Figure 5.3b also presents the thermal expansion of GDC and a SFCM-GDC composite. At temperatures below 550°C , the expansion of SFCM-GDC matches that of pure SFCM, greater than that of pure GDC. Above 550°C , the rate of expansion slows in comparison to SFCM and matches the rate of expansion for GDC. Thus, below 550°C , SFCM-GDC expands the same as SFCM and above 550°C it expands the same as GDC. We would then expect that SFCM-GDC composites have

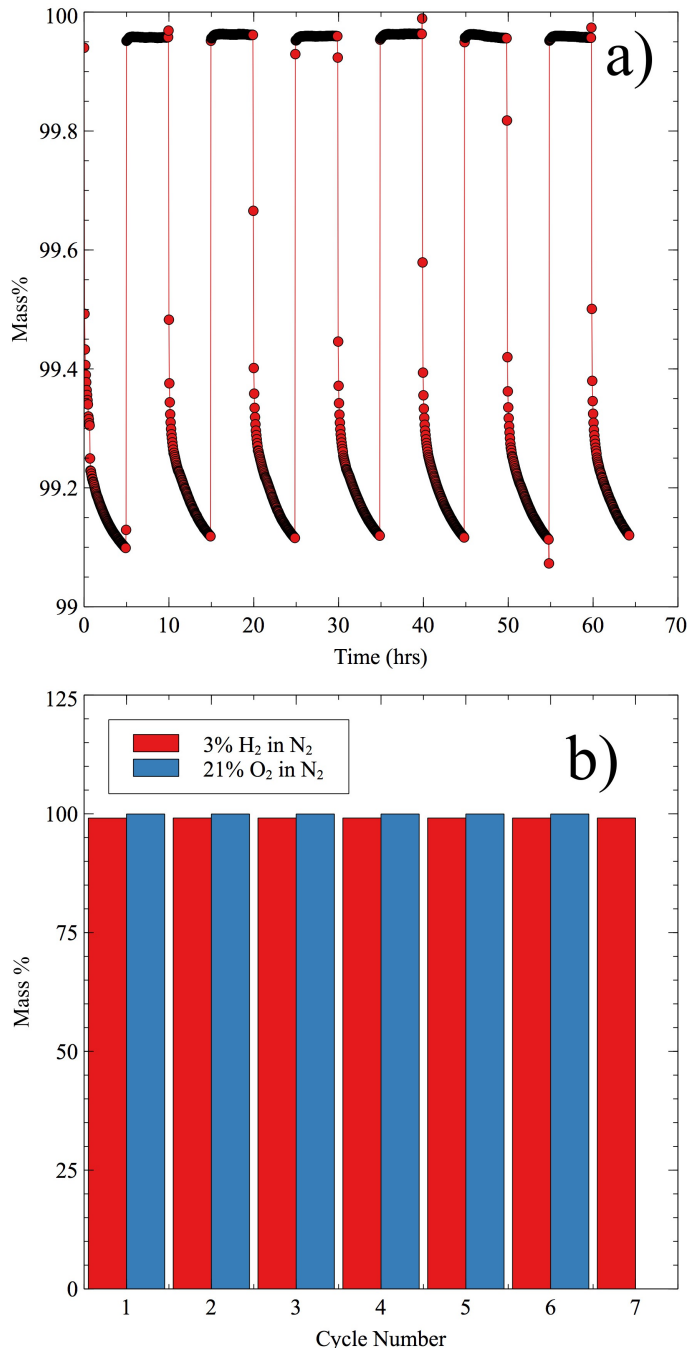


Figure 5.2: Mass changes of SFCM during cycling between 21% O₂ and 3% H₂/3% H₂O in N₂ at 600 °C. Each exposure was 5 hours. a) Percent mass change with time as the gas is switched back and forth. b) Summary of maximum and minimum changes with each cycle.

the same increase in fracture toughness as SFCM up to 550 °C to due expansion and relaxation of intrinsic stresses, but not further increase the rate above 500 °C, as SFCM does.

5.2.3 Half-cell Strength of Anode-Supported SOFCs at Operating Conditions

Figure 5.4 gives box plots of the results of three point flexural testing of SFCM-GDC/GDC half-cells, and Table 5.1 summaries the strengths. The circles on the right of 5.4 represent the results of a Student's t-test, to determine if the means of the different data sets are the same. The more the circles overlap the more similar the data sets are. In this case, there is no overlap between circles at the 95% confidence interval, highlighting that the strengths tested at each condition are unique from each other.

At ambient conditions the strength of the half-cells was measured to be 57.7 MPa. Upon heating, the strength increases to 74.2 MPa. This result correlates with the increase in fracture toughness discussed earlier, which is expected based on Equation 1.6. Another contributing factor to the increase in strength is the effect thermal expansion has on pre-existing cracks and flaws. Any expansion of the material helps push closed a surface crack which would lead to failure, decreasing its size and increasing the stress that would be required to cause that crack to open and propagate.

Upon reduction of the half-cell at 600 °C, the fracture strength decreases

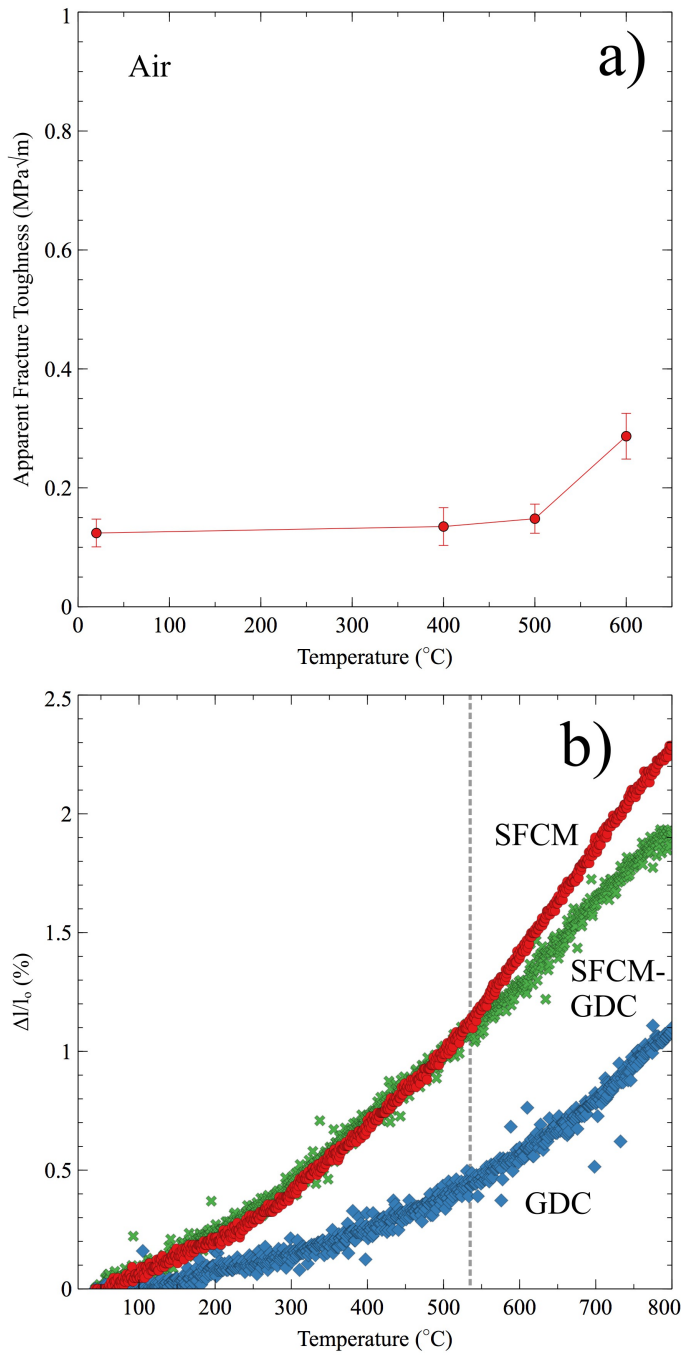


Figure 5.3: a) Fracture toughness of SFCM from 20 $^{\circ}\text{C}$ to 600 $^{\circ}\text{C}$. b) Thermal expansion of SFCM, GDC, and SFCM-GDC.

Table 5.1: Summary of strengths for SFCM-GDC/GDC half-cells at different environments

Temperature (°C)	Atmosphere	Number	Mean (MPa)	Std Dev (MPa)
20	Air	17	57.7	6.71
600	Air	5	74.2	2.98
600	5% H ₂	14	39.9	5.89

below that of the ambient strength to 39.9 MPa. During this transition to reducing conditions, the impurity phase reduces back into SFCM, causing a decrease in mechanical properties from the change in lattice parameters. Additionally, bulk mechanical properties have changed as SFCM becomes pure phase, oxygen vacancies are generated and B-site transition metals are reduced.

Weibull analysis was performed to compare the distribution of flaws between the ambient tested half-cells and the in-situ reduced half-cells. Figure 5.5 displays the fitting of Weibull distributions to the flexural strength of half-cell coupons tested at ambient conditions and during reduction at 600 °C. Table 5.2 summarizes the fitting parameter for the Weibull modulus with 95% confidence intervals using the maximum-likelihood method. Between the two conditions, there is an appreciable change in the Weibull modulus of the two samples. The Weibull modulus increases decreases from 10.4 at ambient conditions to 7.29 when at reducing conditions. This change in Weibull modulus is the result of the reduction of SFCM impurities changing

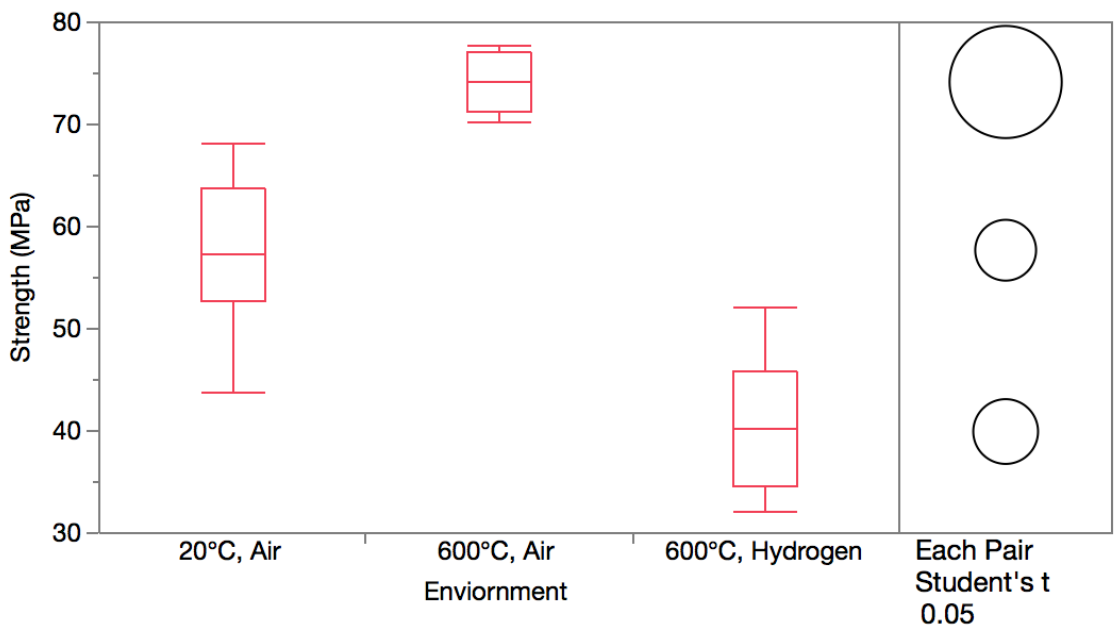


Figure 5.4: Flexural strengths of half-cell coupons made from SFCM-GDC anode with GDC electrolyte tested at 20 °C in air, 600 °C in air, and 600 °C in 5% H₂.

Table 5.2: Summary of Weibull fitting parameters (characteristic strength and Weibull modulus) for SFCM-GDC/GDC half-cells at different environments

Temp. (°C)	Environment	Cha.	α	α	Weibull	β	β
		Strength (α , MPa)	Lower CI	Upper CI	Modulus (β)	Lower CI	Upper CI
20	Air	60.6	57.4	63.6	10.4	6.89	14.7
600	Hydrogen	42.5	39.2	45.8	7.29	4.79	10.3

the bulk properties of the material combined with distribution of flaws becoming wider, creating more variability between flaws.

To confirm any changes in flaw distribution, fractography would need to be performed on every sample, identifying the flaw, but this is not possible due to the porous nature of the fracture surface which obscures the fracture origin. Scanning electron microscopy was performed on fracture surfaces and epoxy-filled samples from each condition to look for any microstructural changes. Figure 5.6 shows the epoxy-filled and polished samples with no discernible difference between samples. No difference is observed because the likely cause of failure, microcracks, would exist along grain boundaries and are obscured by the grain boundaries and pores. [21, 93]

5.2.4 Strength of Anode Support Layer After Redox Cycling

To understand how redox cycling as the result of long term use affects the strength of SFCM based SOFCs, SFCM-GDC ASL test coupons were cycled for 10

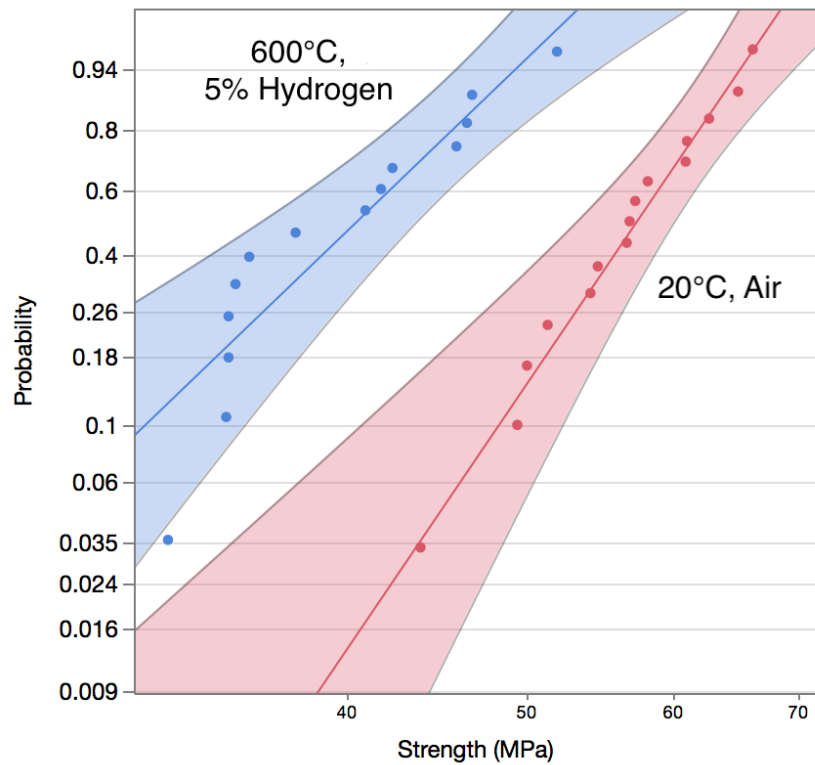


Figure 5.5: Fitted Weibull distributions of SFCM-GDC/GDC half-cells at different environments, plotted linearly with 95% confidence intervals shaded.

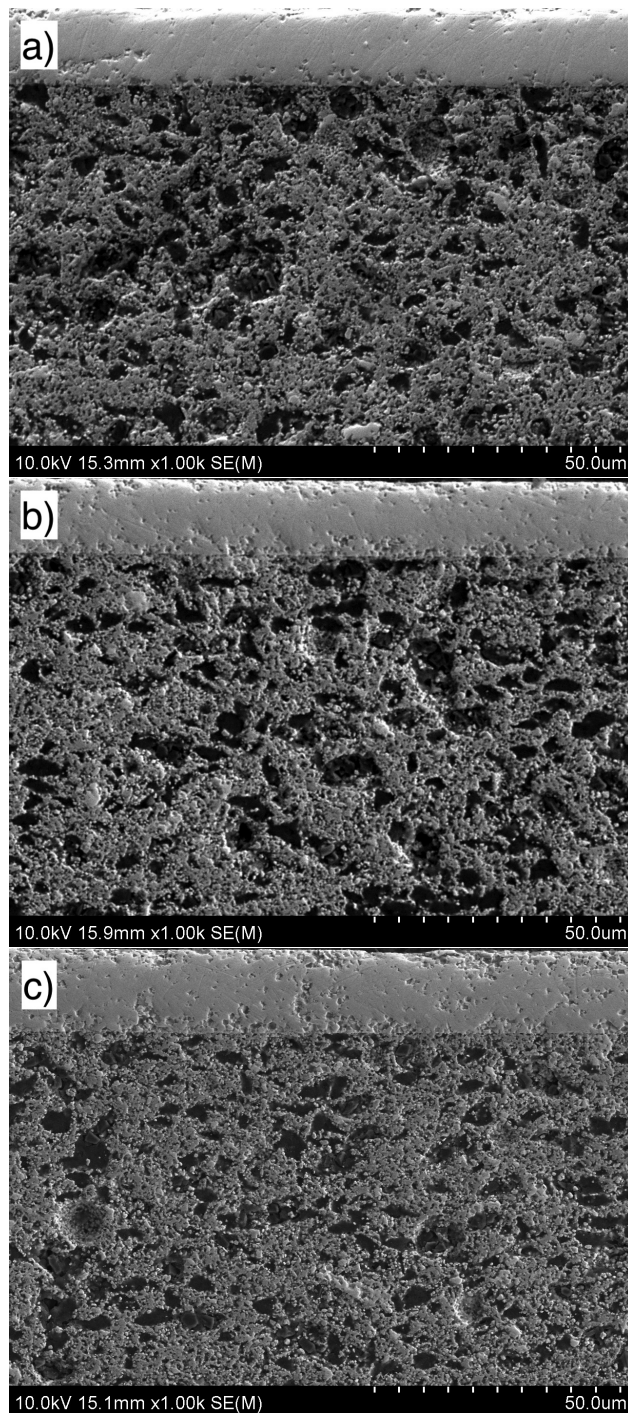


Figure 5.6: Scanning electron microscope images of epoxy-filled and polished SFCM-GDC/GDC half-cell cross sections tested at a) 20 °C in air, b) 600 °C in air and c) 600 °C in 5% H₂

Table 5.3: Summary of Cycled SFCM-GDC ASL Mechanical Properties

Number of Cycles	Number	Mean	Modulus	Mean	Strength
		Modulus	Std Dev	Strength	Std Dev
		(GPa)	(GPa)	(MPa)	(MPa)
0	14	24.5	5.01	34.3	7.23
10	20	27.3	3.60	22.4	4.94

times between nitrogen and 10% H₂ environments. Figure 5.7 shows the strength and modulus from the samples which were not cycled (0 cycles) and those cycled 10 times, tested using a four-point bend at ambient conditions. Table 5.3 summarizes the means and standard deviations of the test results. The overlapping Student's t circles in Figure 5.7b demonstrate that cycling did not significantly change the elastic modulus of the samples, while the strength did significantly decrease. This is the result of changes in microstructural flaws, rather than the change of an intrinsic material property.

The strengths of the cycled and un-cycled cells were fitted to Weibull distributions to observe how flaw distributions changed with redox cycling. Figure 5.8 presents the fitted data and distributions and Table 5.4 summarizes the fit parameters of the Weibull modulus with 95% confidence intervals. The Weibull moduli between the two data sets are very similar, indicating that the flaw distribution is the same between them. The decrease in characteristic strength is then due to the growth of flaws with cycling. SEM images in Figure 5.9 are of a sample which had not

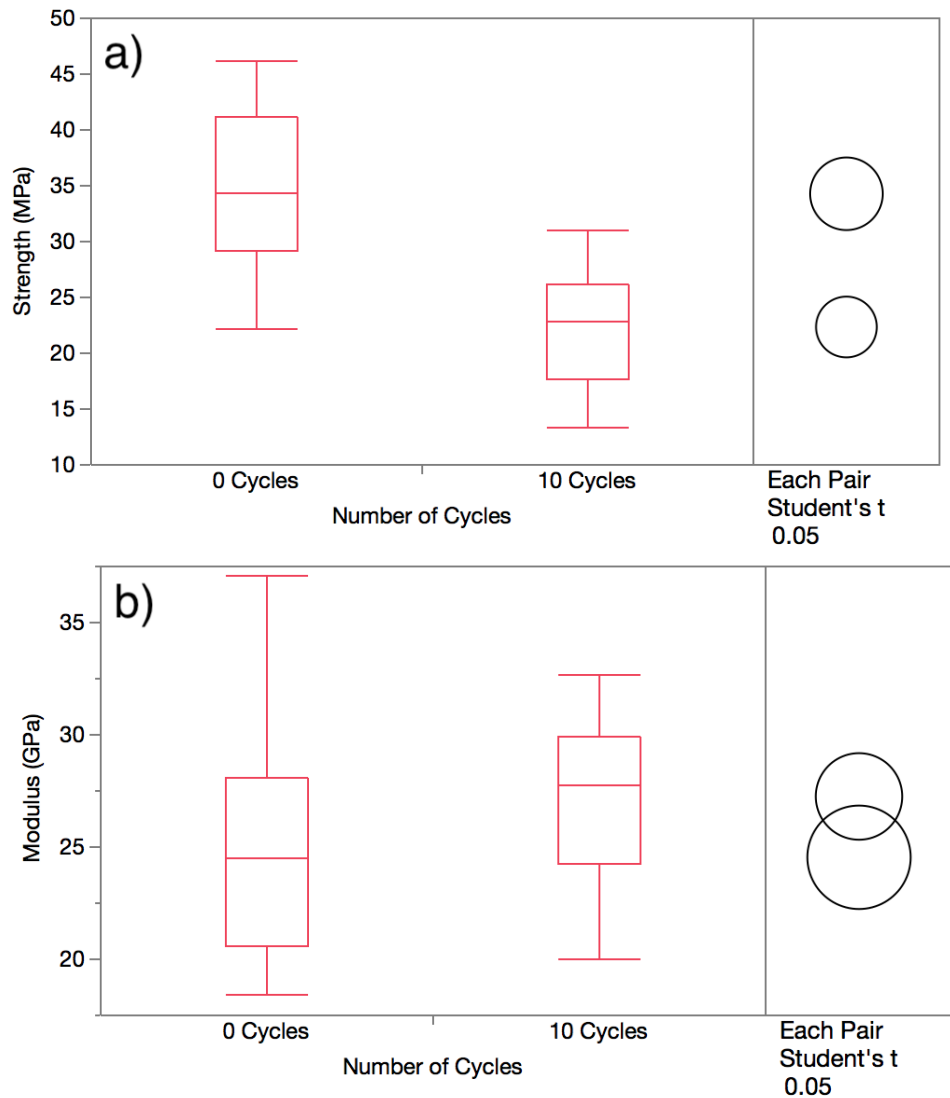


Figure 5.7: Results of four point bend test at ambient conditions of SFCM-GDC ASL with a) strength and b) modulus for samples before any cycling and after 10 redox cycles between 10% H₂ and N₂.

Table 5.4: Summary of Weibull Fit Parameters (characteristic strength and Weibull modulus) for Cycled SFCM-GDC ASL

Number of Cycles	Char. Strength	α	α	Weibull Modulus	β	β
	(α , MPa)	CI Lower	CI Upper	(β)	CI Lower	CI Upper
0	37.1	33.7	40.8	5.75	4.06	9.85
10	24.3	22.3	26.5	5.39	4.00	8.28

been cycled (a) and one which had been cycled 10 times (b) after being epoxy-filled and polished. The sample which had been cycled 10 times has a greater number of pores at larger sizes compared to the un-cycled sample. This indicates that the finer microstructure of the pores is susceptible to changes during redox cycling due to chemical expansion, but the larger flaws which lead to complete cell failure do not change as the result of redox cycling. [94]

5.3 Conclusions

In this work, the mechanical properties of SFCM and SFCM-GDC structures are characterized as the environment is changed from ambient to the working conditions of SOFCs and with redox cycling. The electrical conductivity of SFCM-GDC is stable up to 19 cycles due to the reversibility and phase stability of SFCM-GDC in the environment range. The fracture toughness of SFCM was found to be $(0.124 \pm 0.023) \text{ MPa}\sqrt{\text{m}}$ at room temperature and increases with temperature, due

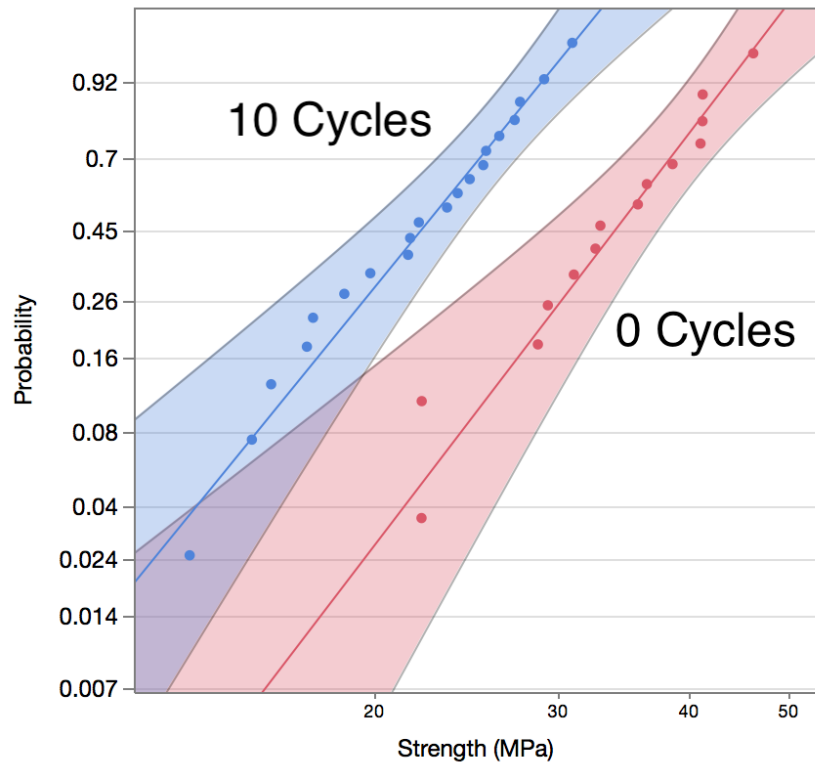


Figure 5.8: Fitted Weibull distributions of SFCM-GDC ASL before any cycling and after 10 redox cycles between 10% H₂ and N₂, plotted linearly with 95% confidence intervals shaded

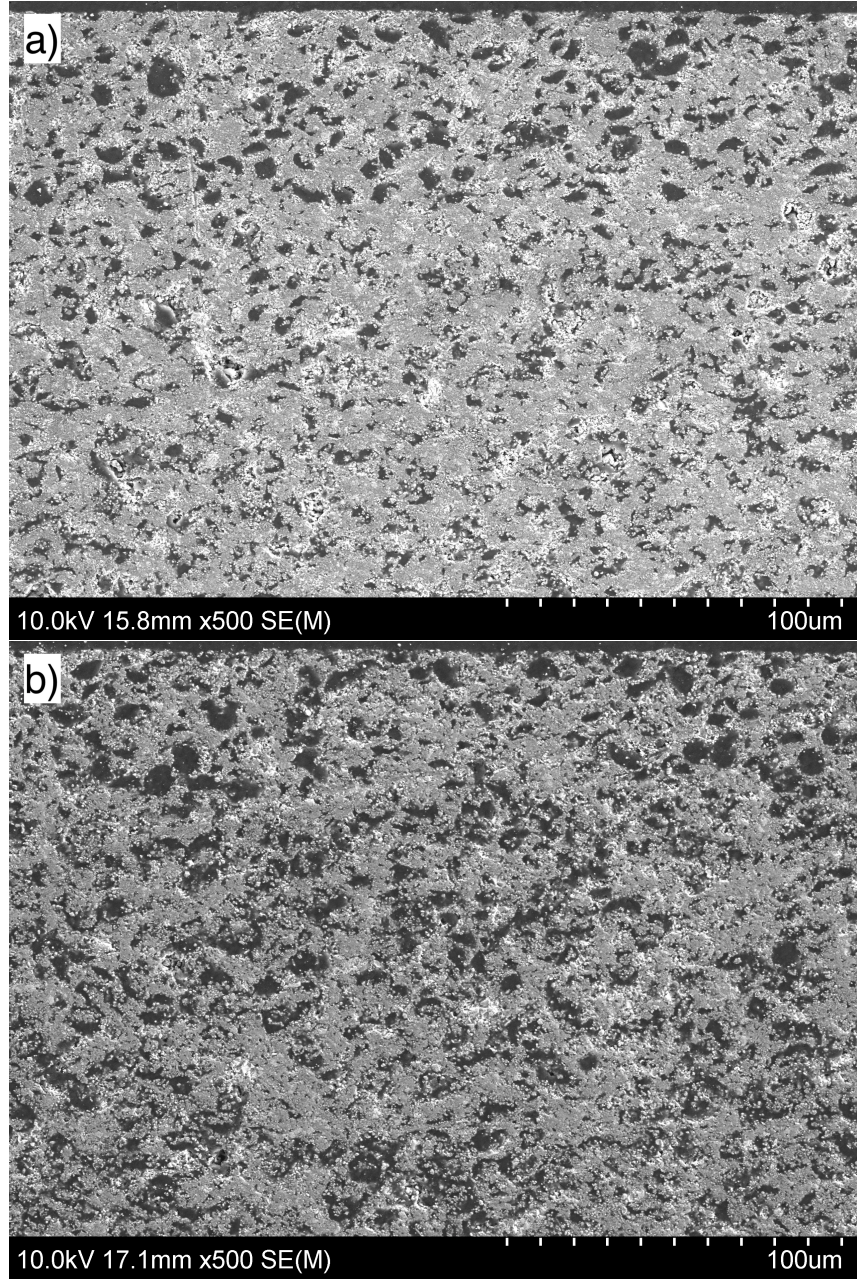


Figure 5.9: Scanning electron microscope images of epoxy-filled and polished SFCM-GDC ASL cross sections tested a) before any cycling, b) after 10 cycles between 10% H₂ and N₂

to relaxation of residual stresses. The flexural strength of SFCM-GDC/GDC half-cells increases by 23.9% upon heating from room temperature to 600 °C. This is due to thermal expansion pushing cracks closed during heating, requiring additional stress to propagate surface cracks and the increase in fracture toughness. Once exposed to reducing conditions, the flexural strength decreases by 29.4% of the original strength, as impurities reduce and SFCM and GDC generate oxygen vacancies. Reduction was shown to increase the size and variability of the distribution of flaws which lead to failure. Redox cycling led to the uniform increase in critical flaw size and changed the fine microstructural porosity, decreasing strength from 34.3 MPa to 22.4 MPa.

These findings show that SFCM, when combined with GDC, make a suitable anode material for SOFCs. SFCM-GDC is a stable material system, both in terms of conductivity and mechanically, with redox cycling. Reduction does increase the likelihood of failure by decreasing characteristic strength and the distribution of flaws, but repeated cycling only decreases characteristic strength and does not change the Weibull modulus.

Chapter 6: Conclusions

SOFCS are an interesting technology with the promise of helping meet growing energy demands by improving fuel conversion efficiency. The mass deployment and adoption of SOFCs are limited by their high operating temperature and reliability concerns. New materials have been developed to help lower the operating temperature of SOFCs to less than 600 °C, but an understanding of how these materials affect reliability needed to be developed. This work has done that, investigating factors which impact mechanical strength and thus the structural integrity of the cell.

To properly investigate the impacting factors on mechanical properties, a test apparatus was built which was capable of testing materials at conditions which are common in an SOFC. Previously, only the temperature or p_{O_2} effects on strength or modulus could be measured. This new apparatus not only can test the flexural properties of materials at temperatures in excess of 600 °C, but it also allows for the control of the gaseous environment. The interdependent effects of temperature and p_{O_2} are now able to be evaluated using this setup.

The use of GDC has enabled the lowering of SOFC temperatures, with Ni-GDC commonly performing as the anode. As a result of this trend, the mechanical properties of GDC, Ni-GDC, and Ni-GDC/GDC half-cells were investigated. It was

demonstrated how the amount and choice of pore-former can impact the mechanical strength due to total porosity percent and shape factor of the pores providing crack tip blunting. Coupons of ASL Ni-GDC and half-cell Ni-GDC/GDC linearly increased strength upon heating with no dependence on half-cell orientation for strength. Upon reduction, all cells showed significant decrease in strength as NiO reduced to Ni, increasing porosity and as GDC reduced. After reduction, the highest strength was shown by samples which had the electrolyte in compression. Finally, it was demonstrated that reduced Ni-GDC/GDC half-cells could be exposed to air for extended periods of time when below 100 °C without oxidation of the Ni or significant impact to the flexural strength upon reheating under reducing atmospheres.

To develop a redox stable system, the phase purity and oxygen non-stoichiometry of a new ceramic anode material, SFCM, was measured under oxidizing the reducing conditions at temperatures in the low temperature-SOFC range. Under a H₂ SFCM is pure phase, but forms Sr₂Co_{1.2}Mo_{0.8}O₆ as an impurity under oxidizing conditions. SFCM itself has very little lattice parameter change at different p_{O₂} but the impurity Sr₂Co_{1.2}Mo_{0.8}O₆ has a cubic structure with a very different lattice parameter. Oxygen desorbs from SFCM starting at 350 °C and continues in excess of 800 °C, enabling it to serve as an MIEC at temperatures below 600 °C. SFCM possesses a low enthalpy of formation of oxygen vacancies (39.1 kJ mol⁻¹), allowing a large number of oxygen vacancies to form, up to a $\Delta\delta = 0.176$ at 600 °C in 97% H₂. The Duncan-Wachsman method was then applied to propose an initial defect equilibrium diagram to match the observed behavior.

This information on the phase and point defect structure of SFCM was used

in understanding the mechanical properties of SFCM and SFCM-GDC composite half-cells. SFCM fracture toughness was measured to be $(0.124 \pm 0.023) \text{ MPa}\sqrt{\text{m}}$ at room temperature, increasing to $(0.286 \pm 0.038) \text{ MPa}\sqrt{\text{m}}$ at 600°C , due to the relaxation of residual stresses from sintering. SFCM-GDC/GDC half-cells increased strength by 23.9% after heating from room temperature to 600°C due to the increase in fracture toughness combined with thermal expansion applying compressive stresses to pre-existing flaws. After reduction, the half-cells showed a decrease in strength as impurities decreased and oxygen vacancies were generated in SFCM and GDC. Redox cycling was found to have no impact on the flaw distribution of SFCM-GDC/GDC half-cells, but the cells did decrease the overall characteristic strength due to the growth of microcracks from the changing amount of SFCM impurities.

Combined, this work evaluates the impact of both temperature and pO_2 on the flexural strength of a current, state of the art electrolyte and anode and a new potential anode material, based on microstructure and point defects. These results can feed back into the design and fabrication of SOFC cells and stacks to improve reliability. With the knowledge that GDC based cells only decrease strength upon reduction, not heating, pre-reduction steps or a gentler reduction process may be developed which reduce the likelihood of failure. Additionally, this work shows how, while an improvement compared to Ni-GDC, SFCM cells do weaken during redox cycling due to impurity formation.

6.1 Future Work

6.2 Publications and Presentations

Appendix A: Statistics

A.1 t-Test

The Student's t-test, or particularly the two sample t-test, is a statistical test commonly used to determine if two sets of data are significantly different from each other. A standard t-test creates a confidence interval around a mean for in which the true mean is thought to exist. By comparing the differences of two means and using the null hypothesis test to determine if the difference is zero, it can be determined if the two means are distinct, with a particular confidence. In the case of randomly dividing samples to receive separate treatments, this constitutes an unpaired test, as compared to a before-after sample set in which measurements are paired. The t-test thus gives a way to evaluating two sets of data, say flexural strength before and after reduction, and to calculate if the reduction had any significant effect.

Like all statistical tests, this relies on a few base assumptions about the population. First, it is assumed that the population has a normal distribution, which reasonably fits for the samples which were studied. This assumption can be tested by other statistical tests, such as the Shapiro–Wilk test or Pearson's chi-squared test, or can be confirmed visually by comparing a histogram of the data to a normal distribution plot. The Student's t-test is not overly sensitive to the fit a normal

distribution, but cases such as bimodal distributions will give inaccurate results. Second, for the t-test as described by Student, the two populations should have the same variance, meaning that the spread of the data compared to the mean should be equivalent, as determined by the F test. In the event where the variances are not equal, a variation of the t-test may be used known as the t-test for unequal variances or the Welch's t-test. Finally, the two populations should be sampled independently from each other.

The t-test begins by calculating the t-score or t-value for a data set. The broadest and most applicable means of doing this is given by the Welch's t-test, Equation A.1, which is for sample sets with unequal variances and unequal sample sizes. \bar{X} is the mean of the sample set, s^2 is the variance, and n is the number of samples in the sample set. Because the true variance of the population is not known, the variance of the sample set is used which is the square of the standard deviation.

$$t = \frac{\bar{X}_1 - \bar{X}_2}{\sqrt{\frac{s_1^2}{n_1} + \frac{s_2^2}{n_2}}} \quad (\text{A.1})$$

Once the t-score is calculated it is compared to the critical t-score based on the confidence level desired and degrees of freedom in the measurements. Typically, a confidence level of 95% is used, but 99% is also frequently found. This can also be referred to the level of significance, which is 1 minus the confidence level, so 0.05 or 0.01. In the simple case of a single set of data, the degrees of freedom is $n - 1$. This is because for a sample set to have a given mean, all but one of the values could be any number (and thus are free), but the last value, must have a value which causes the mean to be what is expected. For two sample t-tests where the sets have

the same number of samples the degrees of freedom become $2n - 2$. But, for the case where the variances are unequal and measurement number may be unequal like Equation A.1, the pooled degrees of freedom must be calculated from Equation A.2, known as the Welch–Satterthwaite equation. The degrees of freedom calculated by Equation A.2 is then rounded down to the next integer.

$$dof = \frac{\left(\frac{s_1^2}{n_1} + \frac{s_2^2}{n_2}\right)^2}{\frac{\left(\frac{s_1^2}{n_1}\right)^2}{n_1-1} + \frac{\left(\frac{s_2^2}{n_2}\right)^2}{n_2-1}} \quad (\text{A.2})$$

With the desired confidence level and degrees of freedom calculated, the critical t-value is then looked up in a table. This table gives the pre-calculated t-values between which 95% or 99% of all values fall for the degrees of freedom in the distribution. If the calculated t-value is closer to zero than the critical t-value, it is determined that the two sample sets do not have a significant difference between them. This is because the difference between the sets falls within the range where 95% of any random selection of two data sets from the same distribution would fall. Conversely, if the calculated t-value is further from zero than the critical t-value, it can be said there is a significant difference between the two and the true population means of the two sets is different.

Many software packages will automatically calculate these values given an input dataset. The work in this thesis used JMP by SAS Institute to perform the calculations, but Minitab, SPSS, R, Python, Matlab, or Excel are all capable of performing the calculations with built-in functions.

A.2 Weibull Statistics

Many things in life do not have one true value but are randomly distributed across a range of possible values, creating a distribution. This distribution can be modeled and analyzed to determine the likelihood of a particular outcome given the total possible number of outcomes. Just as there are many things which can fit a distribution, there are many different types of distributions which can represent the real world case. The most commonly known distribution is the normal distribution but others are frequently used and are variations on each other, such as Student's t, Lorentz, exponential, Chi-squared. In fracture mechanics, the Weibull distribution is used to represent the distribution of the strength of individual samples. The cumulative distribution function (CDF) of a Weibull distribution is given in Equation A.3, where P is the probability of failure having occurred, σ is the applied stress which is greater than zero, σ_{min} is the minimum stress needed for failure, σ_θ is a scaling factor known as the characteristic strength, and m is the Weibull modulus, or the distribution shape factor. Commonly there is considered no minimum stress for failure to occur, resulting in $\sigma_{min} = 0$.

$$P = 1 - e^{-\left(\frac{\sigma-\sigma_{min}}{\sigma_\theta}\right)^m} \quad (\text{A.3})$$

The Weibull distribution was first proposed by Waloddi Weibull as an empirical fit to the observations he had been making. In a curious case, years later, his Weibull distribution was backed up by theory as extreme value distributions and weakest link theory was developed in the study of fracture mechanics. In weakest link theory,

it is the result of only the largest flaw which causes failure. If a material has a normal, symmetric distribution of flaw sizes, then the cases of the largest flaw will be naturally skewed to the right, above the mean size and following the tail of the normal distribution. Of the functions which were developed for extreme values, Weibull's offered the most versatility in terms of bounds, fit and confidence intervals.

The Weibull distribution given in Equation A.3 has two parameters, the characteristic strength and the Weibull modulus. The characteristic strength is very similar in concept to the mean of a distribution but will always be slightly higher. The mean of a distribution is defined as the point where the total probability has reached 50%. In contrast, the characteristic strength is defined as the point where the total probability has reached 63.2%, or otherwise the strength which makes the exponential term of Equation A.3 go to -1 . The Weibull modulus is a measure of the width of the distribution and thus the variability of flaw sizes and strength of the material. The value of the Weibull modulus depends highly on the material and the processing which occurred, but typically ranges in the 1 to 20 range. From an engineering perspective, a high Weibull modulus is desired because it makes the failure point more predictable. If multiple flaw types exist, each with their own distribution, the application of the Weibull distribution become complicated. Failure of each sample must be assigned the different types via fractography, and the contribution of each distribution attributed to that of the whole.

The CDF can be plotted linearly by rearranging Equation A.3 to take the form of Equation A.4, where the slope of the line is m and the intercept is $-m \ln(\sigma_\theta)$. This allow for fitting of the Weibull parameters and a visual estimation of if the data

fits a Weibull distribution. The preferred fitting method is the maximum likelihood method, rather than the linear regression method, as it results in smaller confidence intervals for the estimated parameters.

$$\ln(-\ln(1 - P)) = m \ln(\sigma) - m \ln(\sigma_\theta) \quad (\text{A.4})$$

To achieve meaningful results with small confidence intervals, a large number of samples must be tested. It is best practice that for Weibull parameters to be estimated, in excess of 30 samples should be tested. While sometimes it is not practical to test such numbers of samples, values reported with smaller sample sets should have the confidence intervals examined.

One unique advantage of the Weibull distribution is the ability to scale the stress applied to a sample to a different size. When applying stress to a relatively small sample, due to the low volume of the stressed sample, there is a low probability that a large critical flaw will be found which causes failure. If, one was to repeat the test on a larger sample, the added volume means a greater chance of having a critical flaw cause failure at a lower strength. As a result, the larger volume which is placed under stress, the weaker it will be. Equation A.5 shows this relationship where V_E is the effective volume which was placed under stress. For a pure tensile test, V_E is the entire volume of the sample, but for flexural tests V_E is much less. In addition to being able to scale the overall size of the sample up or down, this size scaling allows for the comparison between test methods, such as 3-point and 4-point bending. Using the known effective volumes from 3 and 4-point bending with similar sample dimensions and bottom spans, Equation A.6 allows the results

of the two tests to be related to each other, as long as m is constant between the two test methods. As a result, the 3-point bend testing will always result in a greater strength compared to 4-point (as long as $m > 1$), due to the smaller volume which it engages when testing.

$$\frac{\sigma_1}{\sigma_2} = \left(\frac{V_{E2}}{V_{E1}} \right)^{\frac{1}{m}} \quad (\text{A.5})$$

$$\sigma_{3pt} = \sigma_{4pt} \left(\frac{m+2}{2} \right)^{\frac{1}{m}} \quad (\text{A.6})$$

Appendix B: TGA Manual

B.1 Theory of Operation

Thermogravimetry works on the principle of measuring small changes in mass as the environment changes. Changes in environment can come from changing temperature or gas composition. This system uses a Cahn microbalance to measure mass, a furnace to heat the sample up to 1100 °C, and mass flow controllers (MFCs) to control the gaseous environment.

B.2 Mass Measurement

The TGA uses a Cahn D200 microbalance for the mass sensing capability. The microbalance works by measuring the current required to maintain balance between the sample and a counter balance. The sample can be hung at two different points on the arm of the balance, Loop A or Loop B. The choice of loops determines the capacity and sensitivity of the measurements, as shown in Table B.1. Full specifications are given in the microbalance manual. Loop A is used most commonly for its increased sensitivity.

The microbalance has an independent flow of nitrogen gas to it to maintain

Table B.1: Cahn D200 Microbalance Specifications

	Loop A	Loop B
Capacity (g)	1.5	3.5
Maximum Weight Change (mg)	150	750
Sensitivity (μg)	0.1	1
Repeatability	10% total load on both pans	

a consistent atmosphere. Only a small amount of flow is required (5 to 10 sccm) to keep positive pressure, but if the protective cover is removed additional time will be required to purge the balance.

B.2.1 Setup and Operation

Alignment of the balance is key to producing a low noise signal. Ideally, the hang-down wire should run through the center of the tubes and at minimum it must not touch anywhere or allow the sample pan to touch the walls of the furnace. The hang-down wire is made from platinum or a platinum-rhodium mixture and is in two pieces, to facilitate the changing out of the bottom portion in case of contamination and degradation. Two successful methods of straightening the wire are to lay it flat on a surface and roll it out from the center, similar to working dough, or to hang it with a weight and soften it using heat allowing it to stretch straight. Hooks on the ends are created using tweezers and a razor blade for a sharp bend.

With the hang-down wire straight and in place, the furnace tube can be adjusted

to place the sample pan in the middle, equidistance from all walls. Moving the tube can be achieved by adjusting the supporting clamp at the bottom of the furnace or adjusting the insulation holding it in place at the top. Alignment usually requires looking straight down the tube from above the microbalance. A light can be placed at the bottom of the tube, replacing the thermocouple, to give illumination as to the location of the sample pan in the tube. Alternatively, the furnace can be heated to 800 °C so that the tube and pan glow, giving a better light, but adjustments must wait for the furnace to cool. Usually, both methods are used, the flashlight for a first alignment and the hot furnace to check afterwards.

With everything aligned, the counterbalance needs to be properly adjusted. Place on the sample pan any appropriate crucible which will be used and open the microbalance cover and remove the cover from the counterbalance by gently pulling. At this point, the microbalance is turned off using the switch on the back of the microbalance controller unit. Counterbalance weights are added or removed to have the empty sample pan and crucible balance with the counter. A light touch to the arm of the balance may be needed to off-set static and friction but ensure this is done with clean tweezers. Once the system balances, or does so as closely as possible, the covers may be replaced and the balance turned back on. Static, especially in the winter time, commonly causes the counterbalance to swing wildly as the cover is placed back over it. Using an un-gloved hand or wiping the inside down with deionized water helps reduce the static.

The thermocouple in the bottom of the furnace should be placed as close to the sample as possible. To achieve this, the thermocouple is incrementally raised

while observing the mass readout from the microbalance. Once the balance becomes unstable or jumps, the thermocouple should be backed out 0.5 to 1 cm and tightened in place. The thermocouple is covered with a quartz sheath to act as a thermowell and protect the thermocouple. If changing between materials systems or significant degradation has occurred to the thermowell, it should be replaced.

At this point, the system should be burned out to remove any contamination on the sample pan or hang-down wire, and time is needed for it to stabilize. The furnace should be heated to 1000 °C for 4 hours in an oxygenated environment. This also provides time for the system to stabilize, as monitored by creating a run with the MicroScan Acquisition software. It can take up to 24 hours for it to stabilize. If random jumps occur in the mass, recheck the alignment and thermocouple placement.

After stabilization, a sample can be loaded in to a crucible and sample pan. While the microbalance is calibrated to measure the mass of the sample added, it is good practice to measure and record the mass using a separate balance beforehand. Crucibles may be reused where appropriate. After the sample is placed, the furnace is raised slowly, to ensure not altering the alignment, and connected to the fittings above. The furnace should be at the maximum height position when finished. Time should then be given to allow the mass reading to stabilize before starting a test.

The program MicroScan Acquisition controls the TGA and records data. After opening, select “Balance > Establish Connection” to connect to the D200. If an error occurs, power cycle the balance, restart the program, and check the serial cable leading to the balance. Upon successful connection, the current readout of the balance will be displayed. The balance may be tared before adding a sample

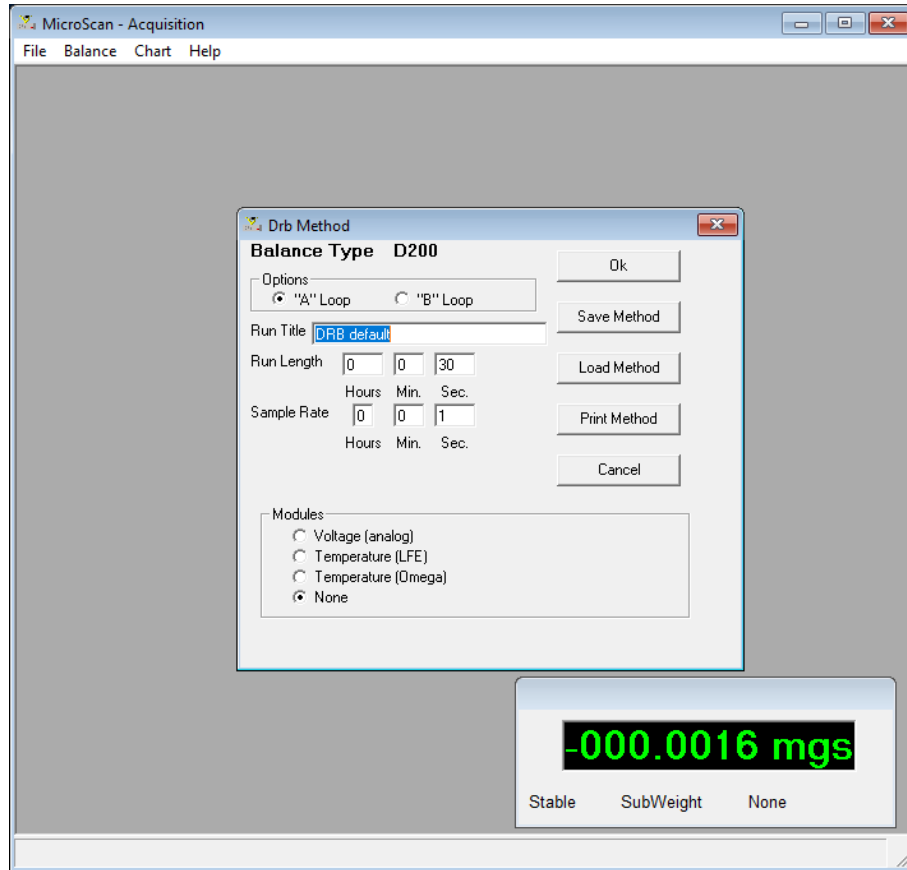


Figure B.1: MicroScan Acquisition with Open Method open and the current read out of the balance displayed

by selection “Balance > Tare.” Starting a new run is achieved by selecting “File > Open Method.” Figure B.1 shows the “Open Method” screen with the current balance readout from MicroScan Acquisition.

From here, the total length of the run is defined along with the sample rate. The sample rate will need to match the rate given in the other programs. Additionally, the run title can be defined and the loop can be changed if needed. Once the run length and sample rate are entered, selecting “Ok” brings up the menu where the run can be started. Selecting “Start Run” causes MicroScan Acquisition to prompt for

the location to save the data in a proprietary format, and once the file path is given, it then starts collecting data. During the run, collected data is plotted and can be viewed using the controls at the top of the plot. After a run is complete, the saved file is converted to a comma separated value (csv) by opening it with MicroScan Analysis and selecting “File > Export... > Comma/Tab Separated...”

B.3 Heating

Heating is done by a furnace surrounding the alumina or quartz tube and sample. It is controlled by a Eurotherm controller and readings are taken from a thermocouple placed inside the furnace tube. As a result, there is a lag in the system between the furnace elements heating and the thermocouple sensing the heat. The controller can be programmed with up to 8 segments in the temperature profile and programming can be performed from the front panel of the unit or by the Eurotherm iTools software. The iTools software must be closed before attempting to use the LabVIEW program which reads the temperature from the controller.

B.4 Gas Delivery

Gas flows are controlled by the MKS Type 647C Multi-channel Flow Ratio/-Pressure Controller and the individual MKS Type M100B MFCs. Each MFC controls one gas by measuring the flow with a thermal mass sensor and adjusting it using a valve to meet the desired set point. Each MFC has a rated size and must have the zero and gas correction factor (GFC) properly set. The zero can be set physically

using a screw on the MFC if a large adjustment is needed or electronically using the controller. The zero should be set with both sides of the MFC open to the atmosphere to ensure no leak from a leftover pressure differential. The GFC can be theoretically calculated based on the heat capacity of the gas compared to a standard. This assumes that the MFC is properly calibrated, which may not be a safe assumption. As such, it is best to calibrate the MFC by adjusting the GFC so that it measures correct flow rates as given by a bubble meter.

If an MFC leaks despite being set to off, the tension spring for the valve located inside the MFC may need adjustment. The manual for the MFC outlines the procedure. If the tension is correct and the valve still leaks, service is advised. An alternative is to add an external shut-off valve, which can be closed either manually or automatically. This has been implemented for one of the current MFCs.

Different gases can be supplied to the MFCs as needed for the experimental setup. If the gas to an MFC is changed, a new GFC will need to be obtained. Gases can be humidified after the MFC with the use of a bubbler, but they should not be humidified beforehand for risk of damaging the MFC. Care should also be taken when mixing or changing gas compositions to avoid potentially dangerous combinations, such as mixing fuels and oxidizers. When changing between a reducing and oxidizing environment, it is good practice to allow sufficient time for a sweep gas (such as N₂) to reduce the risk of the different atmospheres mixing.

The MFCs can be controlled by a computer with LabVIEW. They can either be manually set or given a scheduled program to follow. Typically, a constant total flow rate will be used among all tests. A good starting point for the total flow rate

is 50 sccm. After turning on the MKS controller, the master flow control must be turned on by pushing “ON” followed by “0/All.”

B.5 pO₂ Measurement

p_{O₂} of the gas flow is measured by a home-built YSZ sensor located after the MFCs combine into one flow. Gas flows down a two-bore alumina tube along with a platinum wire to the end of a YSZ tube. The wire is lightly connected to the inside of the YSZ tube using platinum paste. The gas then flows in the reverse direction, between the alumina and YSZ tubes to the outlet. Outside the YSZ tube at the end, a separate piece of platinum wire is connected to the end of the tube. This setup is then placed in a furnace and heated to 800 °C where the difference of partial pressure can be measured according to the Nernst equation. Voltage potentials from the two wires are measured by a Keithley 2000 digital multimeter.

Once the system is setup, very little needs to be done to maintain the sensor. If the sensor needs to cooled in anticipation of a power outage or in order to be worked on, a ramp rate of 1 °C min⁻¹ is to be used to avoid damaging the YSZ tube. For accurate p_{O₂} measurements, after any modification a calibration curve needs to be created using a reference meter. Voltage measurements and p_{O₂} calculations are recorded by the computer using a LabVIEW program.

B.6 Controls

Almost all of the components of the TGA system are computer controllable. As previously mentioned and explained, the microbalance is controlled by the MicroScan Acquisition program. LabVIEW programs interface with the Keithley, MKS controller, and Eurotherm temperature controller.

B.6.1 Gas Controls

Gas flows can be controlled with either the Gas Controller or Gas Scheduler programs. Gas Controller allows for the immediate control of any gas flow channel while Gas Scheduler changes the gas flows at predetermined times allowing for the automated changing of composition. Figure B.2 shows the front panel of Gas Controller, Figure B.3 is the front panel of Gas Scheduler, and the code for both programs is explained in Appendix C.2

To start using Gas Controller, ensure proper channels are set for the MKS Controller Port, Arduino Port, and Servo Channel. On and Off position adjust the position of the external shut-off valve controlled by the Arduino. These values should only change if changing USB to serial adapters or with new hardware. Starting the LabVIEW program immediately begins the control to gasses to the specified values. The radio buttons on the left turn channels on or off and set them to the set point. To end the program, push the STOP button within the program front panel. The program displays the current reading for the flow to ensure flow is occurring as specified.

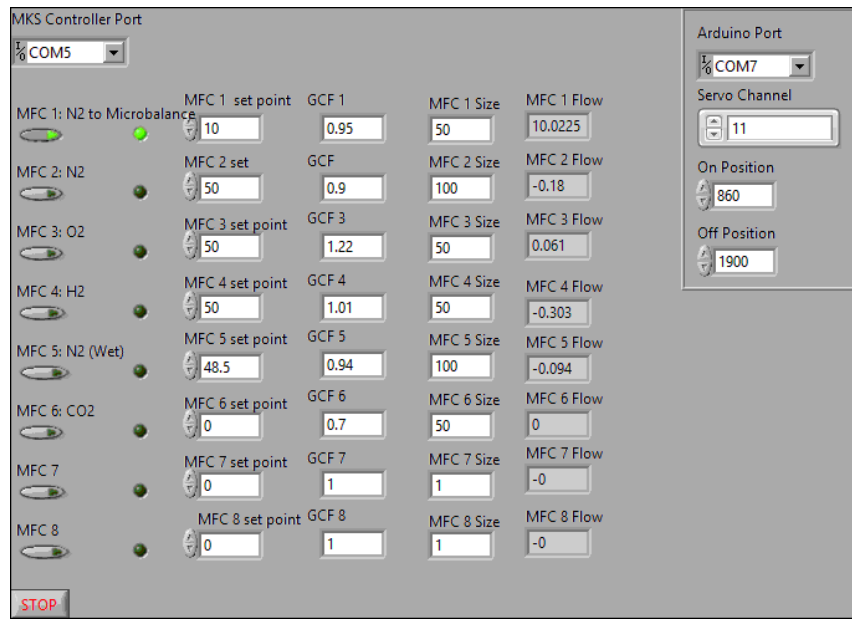


Figure B.2: Front panel display of Gas Controller program

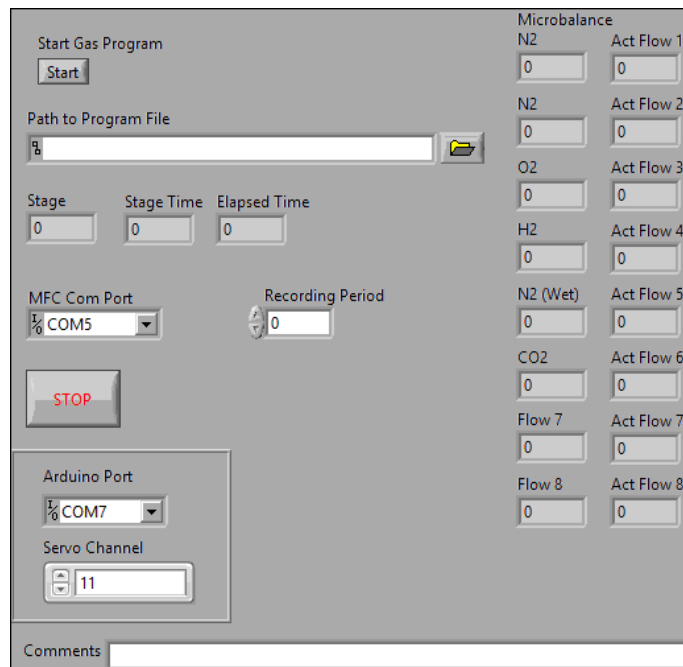


Figure B.3: Front panel display of Gas Scheduler program

The Gas Scheduler requires the input of a tab delimited text file, referred to as a schedule. An example schedule comes with the program. In this schedule, the time for the desired gas flow is given in seconds, followed by the set point of each channel. The program ends on the row with a negative time value, retaining those set points.

Before starting the program, the file path to the schedule must be given by clicking the folder icon next to the Path to Program File field. Again, ensure that the com ports and channels are correct. The program records the measured flows at a set interval, as defined by the Recording Period (in seconds) and records them to a csv. Additionally, comments can be added to the csv in the optional comments field. After starting the program, the start button needs to be pressed.

B.6.2 Temperature and p_{O_2} Measurements

The program Temp & pO₂ Measurements reads the values from the Eurotherm controller and the Keithley multimeter, plots them, and records the results to a csv. Figure B.4 shows the front panel of the program with the user controls.

Before running the program, ensure that the com ports and channels are correct. The Measurement Period should match that given to MicroScan Acquisition. Enabling the timer provides for the program to stop at after the designated time. Comments can be added to the csv file by filling in the File Comments field. When the program starts running, it will ask for the location to save the csv. As a note, the timer for the program starts as soon as the program does, before defining the csv location, but the first measurement does not occur until afterwards.

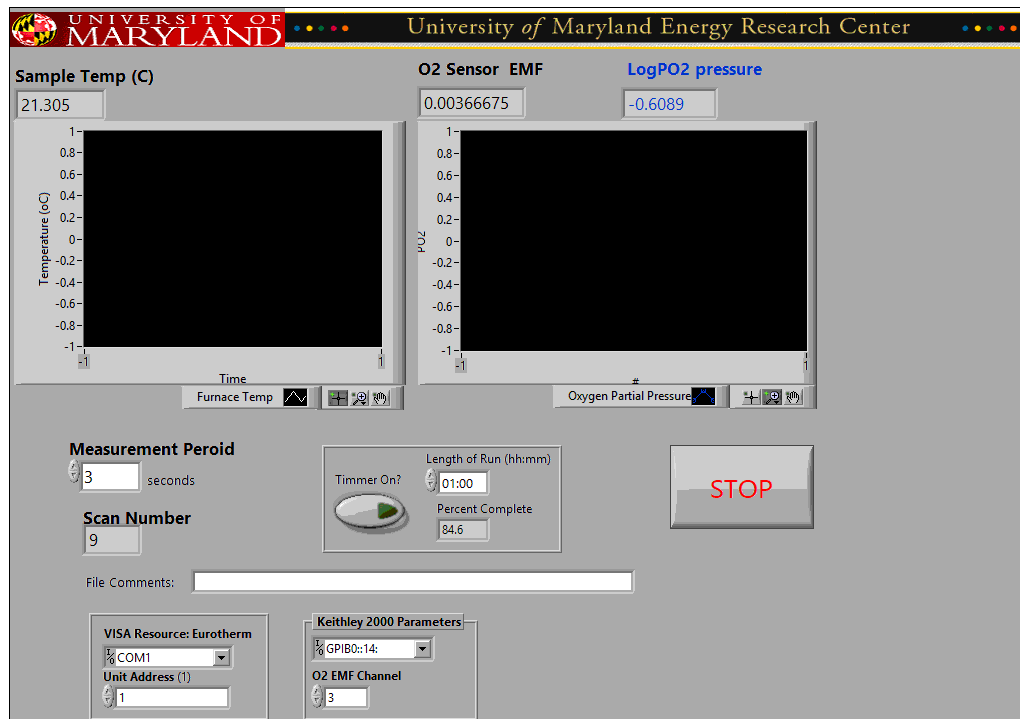


Figure B.4: Front panel display of Temp & pO₂ Measurements program

B.6.3 Starting a Run

Multiple programs need to be started simultaneously for a run of the TGA. Because each program starts differently, the following is a recommendation for the order to start the programs. Time values from MicroScan should then be used in subsequent analysis. This procedure minimizes the amount of time difference between measurements on the TGA, temperature and p_{O₂}.

To begin, enter all values into the various programs. In MicroScan Acquisition, follow the full setup, including clicking Start Run, but stop immediately afterwards with the file browser up. In Temp & pO₂ Measurements, follow the full setup including designating where to save the data. As soon as the file path to save data

is submitted, switch to MicroScan Acquisition and complete the setup, submitting the file path also. If using Gas Scheduler, start that program as normal followed by the temperature program on the Eurotherm.

B.7 Interfacing with Other Devices

The effluent of the TGA can be fed to other devices for advanced analysis, such as an MS. When doing this, one thing to note is physical distance between the TGA and the other instrument. The longer the gas line connecting the two instruments, the longer it will take gas to travel from one instrument to the other. During this time period, diffusion will occur up and down the line, broadening any signal to the second instrument. This delay and broadening effect will need to be investigated for each experimental setup.

B.8 Troubleshooting

- **Unsteady mass:** check alignment and thermocouple placement
- **No gas flow on any channel:** check master flow control
- **No gas flow on one channel:** check if the channel is on and manual valves are open
- **MFC leaks when off:** Check zero, adjust spring tension as described in MFC manual, add external shutoff valve or return for repairs

- **No or noisy voltage from PO_2 sensor:** Check wire connections from sensor, rebuild sensor with new platinum paste
- **Communications Error:** Check that no other program is communicating with the hardware, restart the hardware and unplug then plug-in the USB connection

Appendix C: Code

The programs referenced in this appendix are published as open-source software and are in the public domain. The code and latest versions of all parts are available on GitHub at <https://github.com/patrickstanley/> with the provided repository names and contributions are welcome.

C.1 Arduino PID Relay Furnace Controller with Serial Connectivity

The purpose of this Arduino sketch is to power a heating furnace (controlled by a solid-state relay) with PID controls. In addition, serial communications are used to monitor, log, and interact with the controller. A running average is used to reduce thermocouple measurement noise for the derivate component of the controls.

This sketch is available at <https://github.com/patrickstanley/arduino-pid>.

C.1.1 Hardware and Other Libraries

This was built to be used on a Arduino Uno R3, but should be easily run on a variety of different boards. For temperature sensing, an [Adafruit MAX31856](#) is used with the provided [library](#). Also used is the PID controller [library by br3ttb](#). This sketch pieces the two libraries together and adds serial communications functionality.

C.1.2 Variables

The following is a list of control variables which may be changed per setup.

- RelayPin: The physical pin the relay is connected to.
- Adafruit_MAX31856(CS, DI, DO, CLK): Pins for the MAX31856
- WindowSize: Length of on/off cycle, needed to account for AC power
- printdelay: Delay time in milliseconds for printout on serial
- MaxOP: Maximum operating power, used to extend life of elements
- myPID(&Input, &Output, &workingSet,P,I,D, DIRECT): PID values need to be adjusted for the particular setup. If inverse behavior is experienced (e.g. heats when it should cool) switch DIRECT.
- workingSet and Setpoint: Initial setpoint for power on
- ramrate: Sets a ramp rate for the working setpoint. Measured in milliseconds for 1C change.

C.1.3 Serial Communications

Baud rate is set to 9600. Output is tab delimitated of Setpoint, Working Setpoint, Thermocouple Temperature, and Output Power. To change Setpoint, send a new number over serial and press return. The newline character of the serial monitor may have to be changed send \n as end of line.

C.1.4 Arduino Sketch

```
1 #include <Adafruit_MAX31856.h> //loads library for thermocouple reader
2 #include <PID_v1.h> //loads PID library
3 #include <RunningAverage.h> //loads class for Running Average
   ↳ calculations
4 #define RelayPin 2 //set pin number which is connected to power relay
   ↳ for device
5
6 const byte numChars = 32;
7 char receivedChars [numChars]; // an array to store the received data
8
9 boolean newData = false; //trigger to determine if data needs to be
   ↳ read
10
11 Adafruit_MAX31856 max = Adafruit_MAX31856(4, 5, 6, 7); // Software SPI,
   ↳ Pin number for: CS, DI, DO, CLK
12
13 //Define Variables
14 double workingSet, Setpoint, Input, Output;
15 int WindowSize = 1000; //Length of cycle for power on/off
16 unsigned long prevprintMillis = 0;
17 const long printdelay = 5000; //delay amount before printing via serial
18 unsigned long windowStartTime;
19 unsigned long prevRampTimer = 0;
20 unsigned long MaxOP = .95; // Max Operating Power
21
```

```

22 RunningAverage myRA(10); //Set up running average with # of
    ↪ measurements
23
24 PID myPID(&Input , &Output , &workingSet ,250 ,50 ,8 , DIRECT); //Specify the
    ↪ links and initial tuning parameters
25
26 void setup() {
27     pinMode(RelayPin , OUTPUT); //define RelayPin as an output
28
29     //staring serial communications
30     Serial.begin(9600);
31     Serial.println("PID Controller Output");
32     Serial.println("Setpoint\t Working SP\t TC Temp\t Output"); //tab
        ↪ delimited for logging
33
34     //setup for thermocouple reader
35     max.begin();
36     max.setThermocoupleType(MAX31856_TCTYPE_K); //change type if needed
37
38     windowStartTime = millis(); //start timer for duty cycle window
39
40     myRA.clear(); // explicitly start clean
41
42     //initialize the variables we're linked to
43     workingSet = 20;
44     Setpoint = 20;
45

```

```

46 myPID.SetOutputLimits(0, MaxOP * WindowSize); // tell the PID to range
        ↪ between 0 and the full window size
47 myPID.SetMode(AUTOMATIC); // turn the PID on
48 }
49
50 // function to receive data via serial and process when endmarker is
        ↪ received
51 void recvWithEndMarker() {
52     static byte ndx = 0;
53     char endMarker = '\n'; // define line endmarker for client
54     char rc;
55
56     while (Serial.available() > 0 && newData == false) {
57         rc = Serial.read();
58         if (rc != endMarker) {
59             receivedChars[ndx] = rc;
60             ndx++;
61             if (ndx >= numChars) {
62                 ndx = numChars - 1;
63             }
64         }
65     else {
66         receivedChars[ndx] = '\0'; // terminate the string
67         ndx = 0;
68         newData = true;
69     }
70 }
```

```

71 }
72
73 //Function to repeat new setpoint for confirmation
74 void showNewData() {
75   if (newData == true) {
76     String recievedString = String(receivedChars);
77     Serial.print("Setpoint changed to ... ");
78     Serial.println(recievedString.toFloat());
79     Setpoint = recievedString.toFloat();
80     newData = false;
81   }
82 }
83
84 void loop() {
85   recvWithEndMarker(); //check for new setpoint
86   showNewData(); //sets new setpoint and displays it
87   myRA.addValue(max.readThermocoupleTemperature()); //add themocouple
88   ↪ read to rolling average
89   Input = myRA.getAverage(); //sets PID input to rolling average value
90   myPID.Compute(); //calculate PID output
91
92 //print delay for serial output so not to flood logs
93   unsigned long printMillis = millis();
94   if (printMillis - prevprintMillis >= printdelay) {
95     prevprintMillis = printMillis;
96     Serial.print(Setpoint); Serial.print("\t"); Serial.print(workingSet);
97     ↪ Serial.print("\t"); Serial.print(max.readThermocoupleTemperature()

```

```

    ↵ () ; Serial.print("\t") ; Serial.println(Output/WindowSize*100);

96 }

97

98 //turn the output pin on/off based on pid output

99 if ( millis() - windowStartTime >= WindowSize)

100 { //time to shift the Relay Window

101     windowStartTime += WindowSize;

102 }

103 if (Output < millis() - windowStartTime) digitalWrite(RelayPin,LOW); //  

    ↵ HIGH and LOW set to default off

104 else digitalWrite(RelayPin,HIGH);

105

106 //sets ramp rate functionality

107 unsigned long ramptimer = millis();

108 unsigned long ramprate = 6000; //milliseconds for 1C change

109 if (workingSet != Setpoint)

110 {

111     if (ramptimer - prevRampTimer >= ramprate && workingSet < Setpoint)

112     {

113         workingSet++;

114         prevRampTimer = ramptimer;

115     }

116     if (ramptimer - prevRampTimer >= ramprate && workingSet > Setpoint)

117     {

118         workingSet--;

119         prevRampTimer = ramptimer;

120     }

```

```
121     }  
122 }
```

C.2 MKS Gas Controller and Scheduler

The purpose of these LabVIEW programs is to communicate with and control MFCs for remote and automated operation of the TGA. Individual MFCs can be turned on or off and have their set point changed. After basic controls are developed, a new VI, a scheduling program, is provided which reads a text file automatically changing flow rates at predetermined times. The VI gas controller and gas scheduler VIs, along with a sample gas schedule, are available under the GitHub repository “mks-mfc.” The VIs are saved for LabVIEW version 2013 and later. This work is the continuation and development of programs previously written by others.

C.2.1 Hardware and Other Libraries

These programs are written for the use of a MKS 647C Multi Channel Flow Ratio/Pressure Controller with Type M100B MFCs. It can accommodate up to 8 channels for MFCs and communicates via serial. Drivers for LabVIEW communications with the MKS 647C are available online from the National Instruments (NI) website. Serial communications occur over the VISA standard and require the installation of the VISA drivers from NI.

An Arduino Uno R3 is utilized with a servo motor and 3D printed parts to manually turn a shut-off valve, compensating for a leaking MFC. Details on the installation of the Arduino controlled shut-off including STL files for 3D printing are

available at <https://hackaday.io/project/52519-automated-gas-flow-shut-off>. To control the Arduino from LabVIEW, the LINX library is used and must be downloaded from the VI package manager. Additionally, the Arduino will need to be flashed with the LINX control sketch before use. This component can be easily removed if not required for the application.

C.2.2 Program Overview

The block diagram of the Gas Controller VI, which manually controls the MFCs, is provided in Figure C.1 and is the fundamental starting block for the gas scheduling program. Starting on the far left of the program, initial communications variables such as baud rate and port information are passed to the sub-VIs which open communications. The program then enters a while loop until the stop button is pressed or an error occurs, at which point serial communications are closed by the appropriate sub-VI.

Within the while loop, the program sequentially goes to each channel, checking the desired status, setting the control variables and reading the flow. If the program is set to not use an MFC, the internal valve is shut and the flow is read to ensure no leakage. If an MFC is set to be used, the percent of full flow is calculated based on the size of the MFC, the gas correction factor, and the desired flow rate. The percent of full flow is then passed to the MFC and the flow is read. For the case of channel 3, which possesses a leaky MFC, the addition of an external shutoff valve controlled by Arduino was implemented. If channel 3 is to be used, the Arduino

sends a pulse width modulation (PWM) signal to the servo motor which corresponds to the valve being in the open position. In the case where channel 3 is to be closed, a PWM signal is sent, which closes the valve.

Finally, after each channel has been set, the program checks for the dangerous combination of hydrogen and oxygen gasses. If the channels for hydrogen and oxygen (in this case channels 3 and 4) are both open, the program immediately shuts the valves and gives an error warning the user and ends the program. As long as this is not the case, the program proceeds to loop back to setting the values for channel 1.

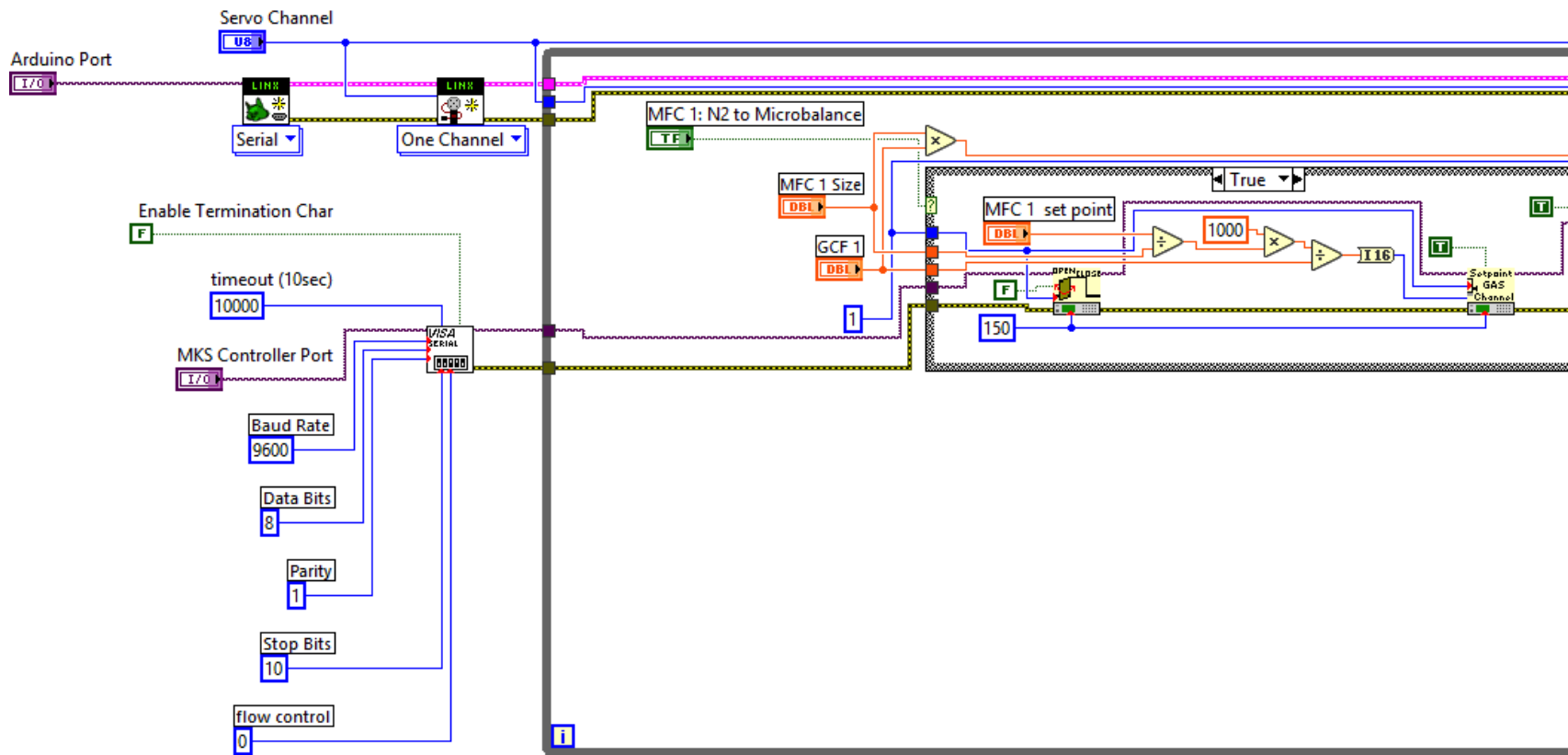


Figure C.1: MFC Controller program

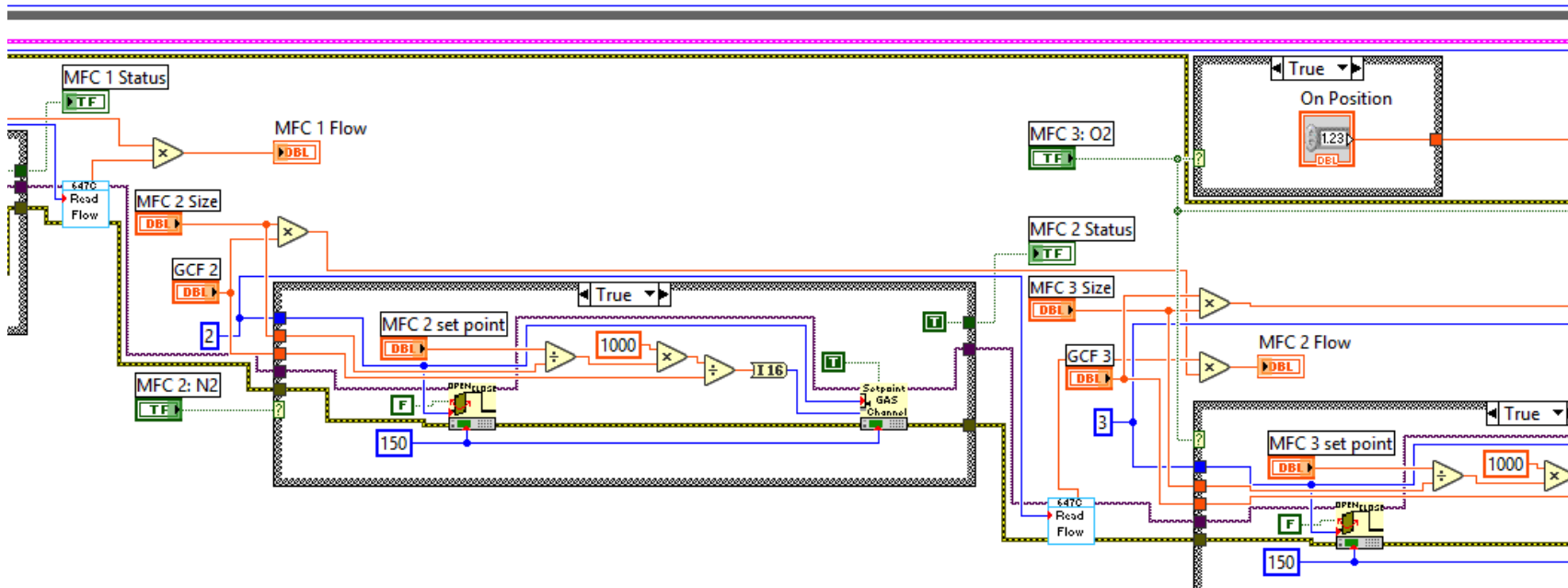


Figure C.1: MFC Controller program (cont.)

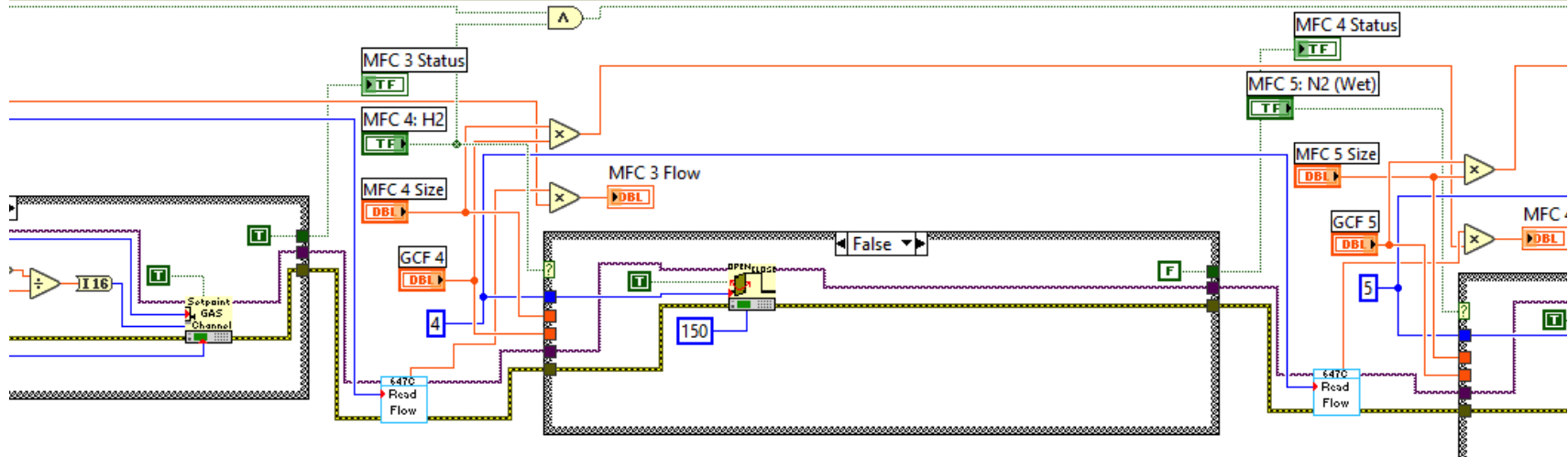


Figure C.1: MFC Controller program (cont.)

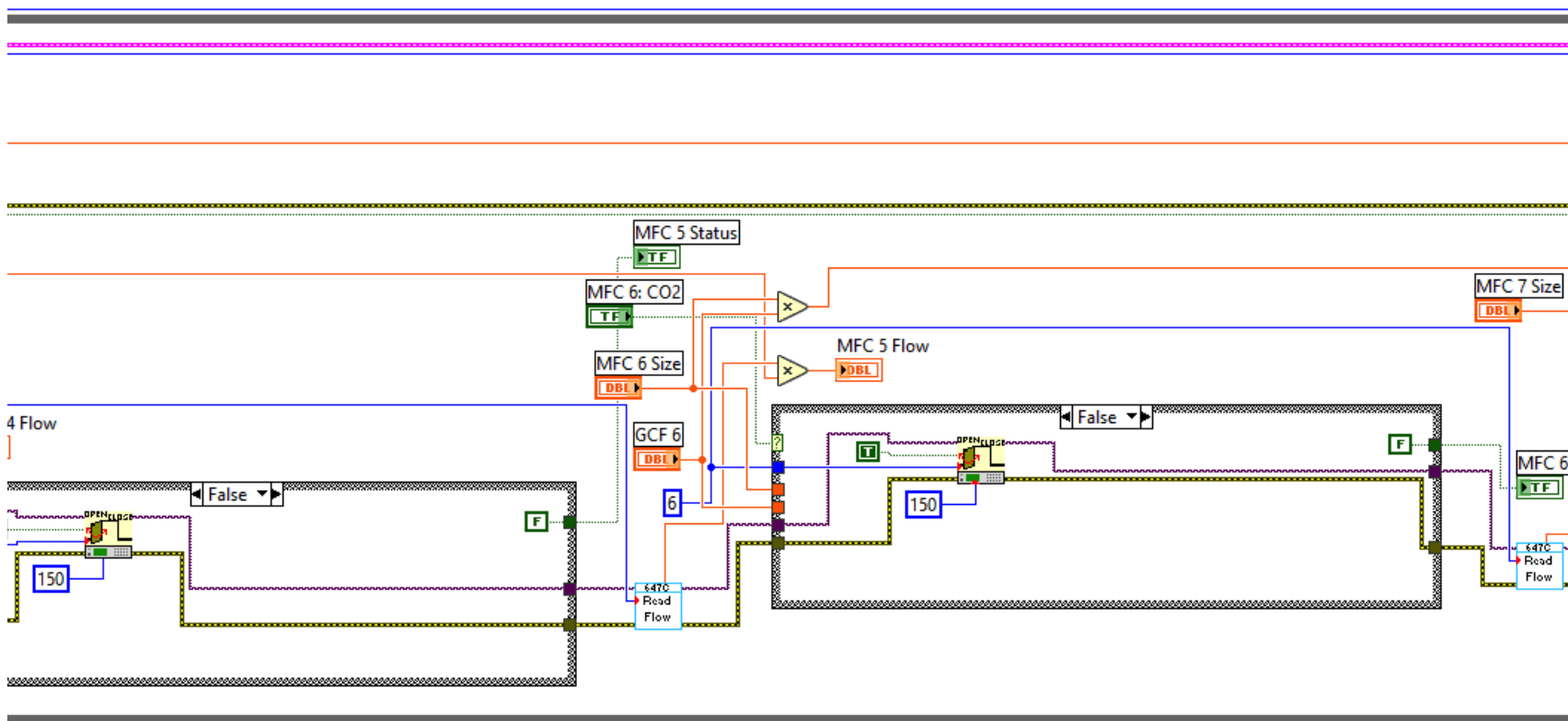


Figure C.1: MFC Controller program (cont.)

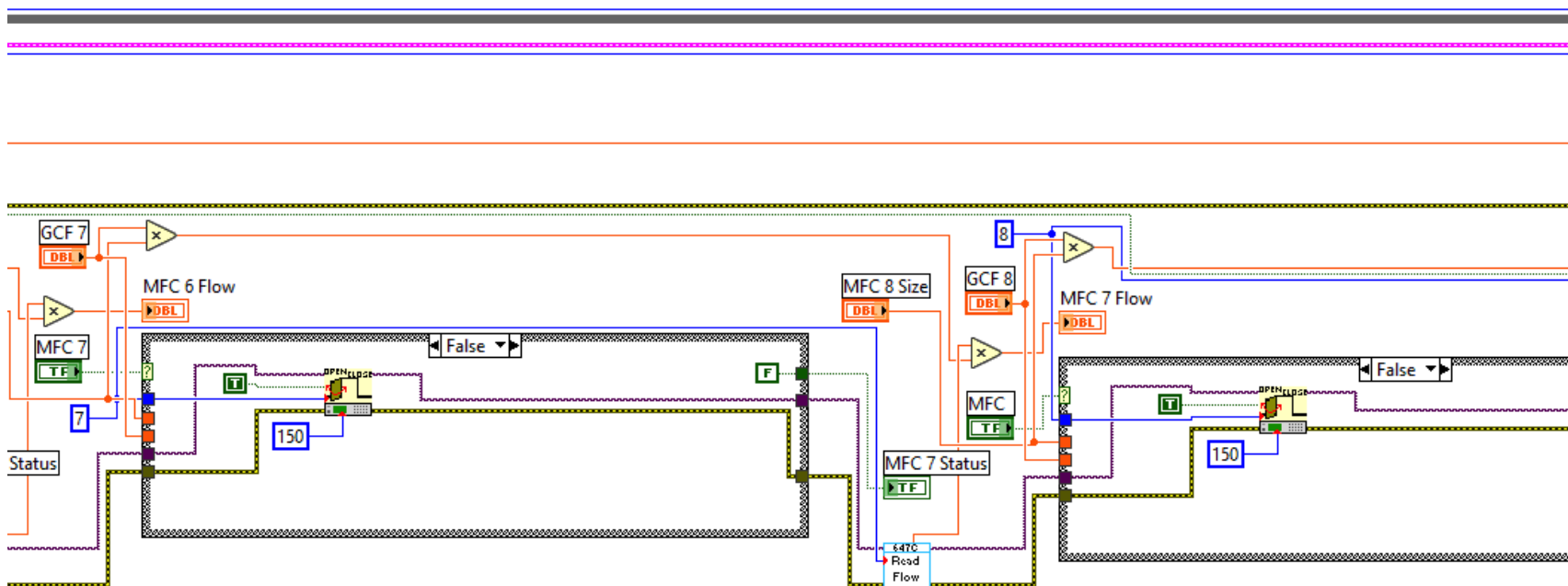


Figure C.1: MFC Controller program (cont.)

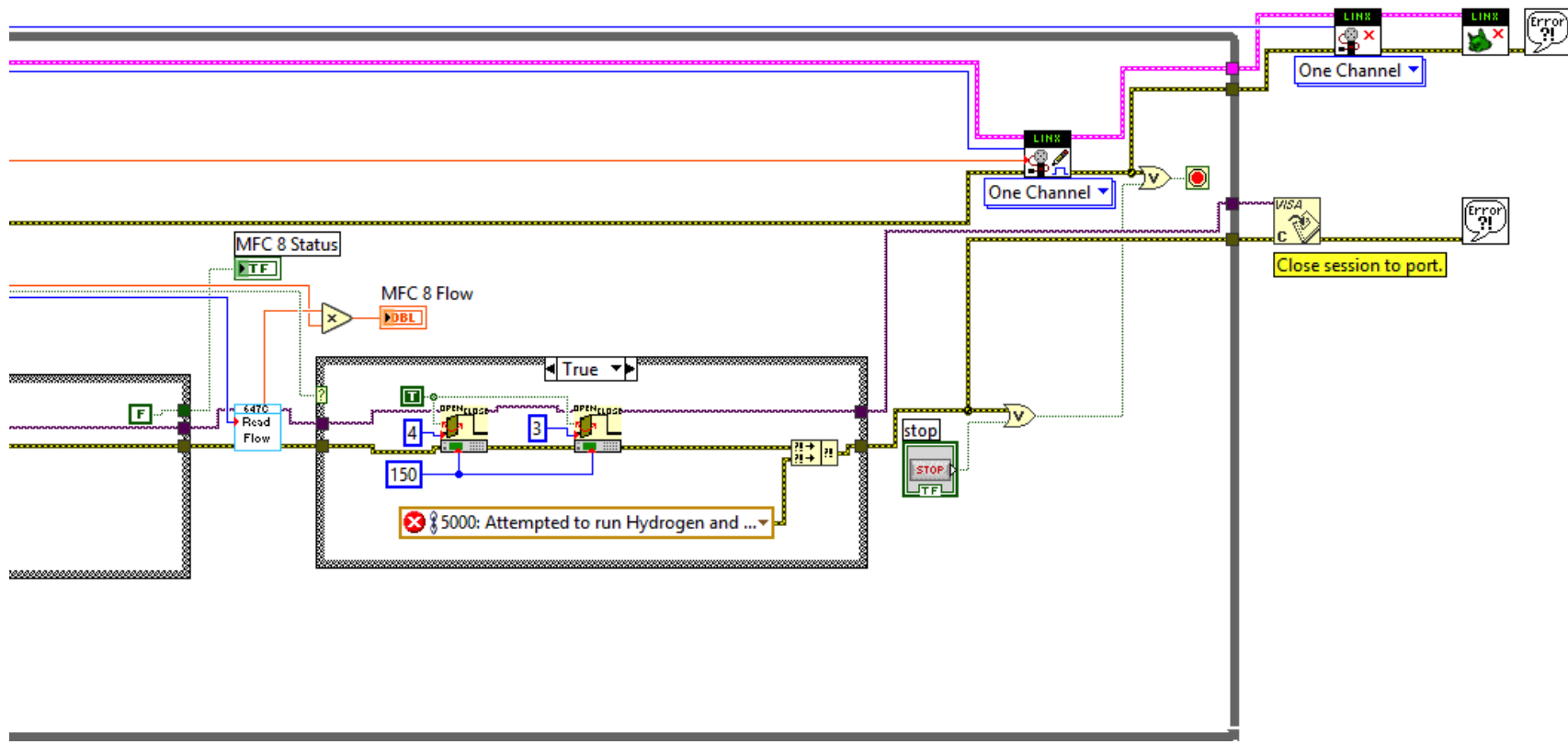


Figure C.1: MFC Controller program (cont.)

The Gas Scheduler program uses the Gas Controller to automate the switching of gasses based on the instructions provided in a text file. The text file, referred to as the gas schedule, is a nine column tab delimited file where the first column is the amount in seconds for which that gas flow is to be run, followed by the flows for each channel. The program sequentially goes through the rows until it encounters a negative time, at which point it ends, leaving that row's gas flows running. The program also additionally records the measured flows to a csv file for manual inspection later.

Figure C.2 gives the block diagram of the program. Before the start of the program, the path to the gas schedule must be specified. At the start of the program, the location to record measured gas flows is requested and setup as a csv file type with a header, variables to count the row of the program and time elapsed are initialized and communications variables are passed to sub-VIs. After this, the program enters a while loop. This while loop is ended if an error occurs, if the stop button is pressed, or if the amount of time in the stage (given by the first column in the gas schedule) is less than zero.

Once the start button is pushed, a timer is started to measure the amount of time elapsed in the stage. If the time has elapsed the amount prescribed (starting with zero seconds), the program reads the gas schedule, increments the stage number, and passes the flow rates to a gas controller sub-VI, after which the VI loops. If time has not elapsed, the program records the flows based on a second elapsed time timer to limit the total number of recordings. After a program end condition is met, the communications channels are closed.

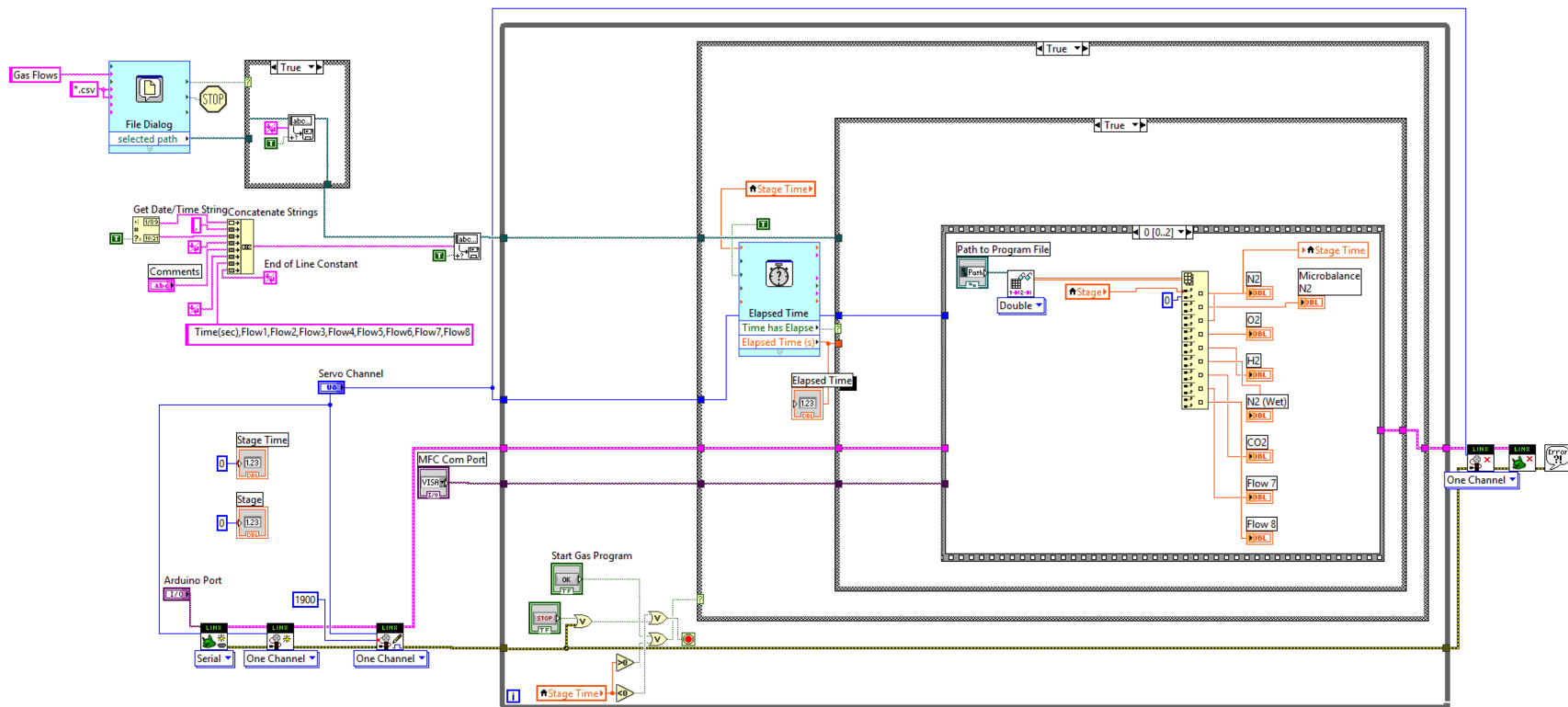


Figure C.2: Gas Scheduler program

C.3 Temperature and p_{O_2} Measurements

The purpose of this LabVIEW program is to periodically measure the temperature from a Eurotherm process controller and calculate p_{O_2} based on voltage from a Keithley multimeter for the TGA system. The VI is available on GitHub under the repository “eurotherm-keithley-measure” and is saved for LabVIEW 2013 and later. This work is the continuation and development of programs previously written by others.

C.3.1 Hardware and Other Libraries

Temperature measurements are taken directly from a Eurotherm 2408 controller with optional serial communications module. A driver package for all 2400 series Eurotherm controllers is available from the NI website. Serial communications again occur by VISA and require the NI VISA drivers.

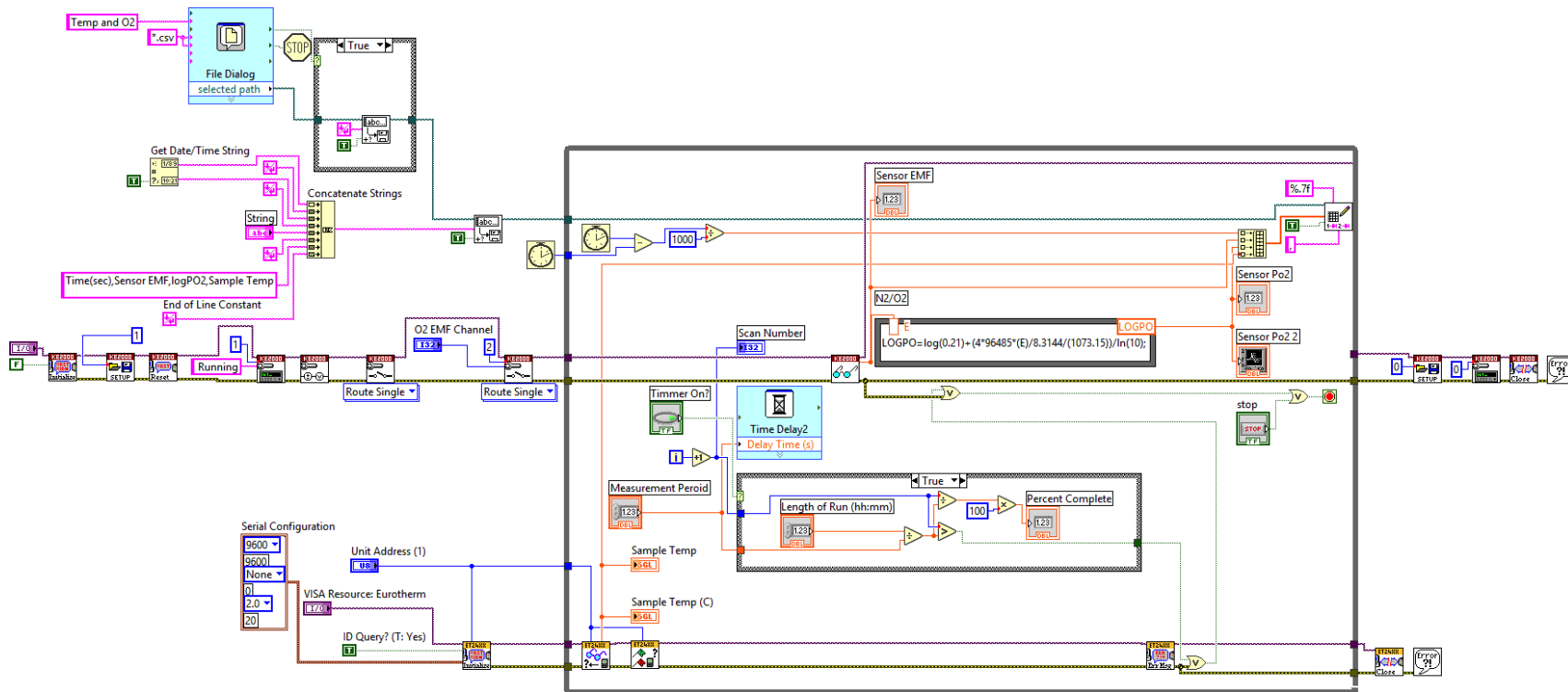
p_{O_2} was calculated from voltage measurements taken of a YSZ sensor by a Keithley 2000 digital multimeter. Communications were established with the Keithley via GPIB (IEEE-488) and thus require the NI-488 driver from NI. Additionally, drivers for the Keithley 2000 are available online from NI and are required for the VI.

C.3.2 Program Overview

A copy of the block diagram is given in Figure C.3. When started, the program asks for the location to save the measurements. The program then creates the csv

file time in seconds, the voltage read, the calculated log p_{O_2} , and the temperature from the controller. Communications variables, such as baud rate and channels, are sent the appropriate sub-VIs to begin communications to the device and a timer is started. The program backs up the Keithley's current settings, resets the device and prepares it to measure voltage on one channel, while displaying "Running" on the front panel display. After the program is complete, the Keithley is reset once again and its original settings are restored before communications are closed to it and the Eurotherm.

The rest of the program occurs in a while loop. The loop is delayed a fixed amount of time, set by the Measurement Period. If the timer functionality is turned on, the loop repeats for a fixed amount of time based on the Length of Run variable, after which a stop signal is sent. During each loop, the process value (temperature) of the Eurotherm is measured and any alarms or flags are checked for. If any occur, they are passed to the error handler and the program stops. The voltage of the specified channel of the Keithley is measured and the $\log(p_{O_2})$ is calculated from it. These values are then displayed, plotted, saved to the csv file.

Figure C.3: Temperature and p_{O_2} measurement program

Bibliography

- [1] U.S. Energy Information Administration. World energy demand and economic outlook. Technical Report May 2016, U.S. Energy Information Administration, 2016.
- [2] Stephen G Osborn, Avner Vengosh, Nathaniel R Warner, and Robert B Jackson. Methane contamination of drinking water accompanying gas-well drilling and hydraulic fracturing. *Proceedings of the National Academy of Sciences of the United States of America*, 108(20):8172–6, 2011.
- [3] Avner Vengosh, Robert B Jackson, Nathaniel Warner, Thomas H Darrah, and Andrew Kondash. A Critical Review of the Risks to Water Resources from Shale Gas Development and Hydraulic Fracturing in the United States. *Environmental Science & Technology*, 16(4):6838, 2014.
- [4] Susan Solomon, Gian-Kasper Plattner, Reto Knutti, and Pierre Friedlingstein. Irreversible climate change due to carbon dioxide emissions. *Proceedings of the National Academy of Sciences of the United States of America*, 106(6):1704–9, 2009.
- [5] J Hansen, D Johnson, A Lacis, S Lebedeff, P Lee, D Rind, and G Russell. Climate impact of increasing atmospheric carbon dioxide. *Science*, 213(4511):957–966, 1981.
- [6] U.S. Environmental Protection Agency. Inventory of U.S. Greenhouse Gas Emissions and Sinks: 1990 - 2015. Technical report, U.S. Environmental Protection Agency, 2017.
- [7] E. D. Wachsman and K. T. Lee. Lowering the Temperature of Solid Oxide Fuel Cells. *Science*, 334(6058):935–939, 2011.
- [8] Robert H. Lasseter and Paolo Paigi. Microgrid: A conceptual solution. In *IEEE Power Electronics Specialists Conference*, volume 6, pages 4285–4290, 2004.
- [9] Seungdoo Park, John M. Vohs, and Raymond J. Gorte. Direct oxidation of hydrocarbons in a solid-oxide fuel cell. *Nature*, 404(6775):265–267, 2000.

- [10] Wikimedia Commons. Solid Oxide Fuel Cell Diagram.
- [11] James Larminie and Andrew Dicks. *Fuel Cell Systems Explained*, volume 93. 2001.
- [12] I. Pilatowsky, R.J. Romero, C.A. Isaza, S.A. Gamboa, P.J. Sebastian, and W. Rivera. Thermodynamics of Fuel Cells. *Cogeneration Fuel Cell-Sorption Air Conditioning Systems*, pages 25–36, 2011.
- [13] Mogens Mogensen, Nigel M. Sammes, and Geoff A. Tompsett. Physical, chemical and electrochemical properties of pure and doped ceria. *Solid State Ionics*, 129(1):63–94, 2000.
- [14] Mikko Pihlatie, Andreas Kaiser, and Mogens Mogensen. Mechanical properties of NiO/Ni-YSZ composites depending on temperature, porosity and redox cycling. *Journal of the European Ceramic Society*, 29(9):1657–1664, 2009.
- [15] J. Laurencin, G. Delette, O. Sicardy, S. Rosini, and F. Lefebvre-Joud. Impact of ‘redox’ cycles on performances of solid oxide fuel cells: Case of the electrolyte supported cells. *Journal of Power Sources*, 195(9):2747–2753, 2010.
- [16] Jiang Liu, Brian D Madsen, Zhiqiang Ji, and Scott A Barnett. A Fuel-Flexible Ceramic-Based Anode for Solid Oxide Fuel Cells. *Electrochemical and Solid-State Letters*, 5(May 2012):122–124, 2002.
- [17] Sossina M. Haile. Fuel cell materials and components. *Acta Materialia*, 51(19):5981–6000, 2003.
- [18] Harumi Yokokawa, Hengyong Tu, Boris Iwanschitz, and Andreas Mai. Fundamental mechanisms limiting solid oxide fuel cell durability. *Journal of Power Sources*, 182(2):400–412, 2008.
- [19] Hideaki Inaba and Hiroaki Tagawa. Ceria-based solid electrolytes. *Solid State Ionics*, 83(1-2):1–16, jan 1996.
- [20] F. Gutierrez-Mora, J. M. Ralph, and J. L. Routbort. High-temperature mechanical properties of anode-supported bilayers. *Solid State Ionics*, 149(3-4):177–184, 2002.
- [21] Ji Haeng Yu, Gun Woo Park, Shiwoo Lee, and Sang Kuk Woo. Microstructural effects on the electrical and mechanical properties of Ni-YSZ cermet for SOFC anode. *Journal of Power Sources*, 163(2):926–932, 2007.
- [22] William D. Callister and David G. Rethwisch. Influence of Porosity. *Materials Science and Engineering: An Introduction*, pages 373–381, 2014.
- [23] Michel Barsoum. Processing and Surface Flaws. In *Fundamentals of Ceramics*, volume 2174, pages 374–381. 2003.

- [24] M. Radovic and E. Lara-Curzio. Mechanical properties of tape cast nickel-based anode materials for solid oxide fuel cells before and after reduction in hydrogen. *Acta Materialia*, 52(20):5747–5756, 2004.
- [25] Miladin Radovic and Edgar Lara-Curzio. Elastic Properties of Nickel-Based Anodes for Solid Oxide Fuel Cells as a Function of the Fraction of Reduced NiO. *J. Am. Ceram. Soc.*, 87(12):2242–2247, 2004.
- [26] J. Laurencin, G. Delette, B. Morel, F. Lefebvre-Joud, and M. Dupeux. Solid Oxide Fuel Cells damage mechanisms due to Ni-YSZ re-oxidation: Case of the Anode Supported Cell. *Journal of Power Sources*, 192(2):344–352, 2009.
- [27] D. Sarantaris and A. Atkinson. Redox cycling of Ni-based solid oxide fuel cell anodes: A review. *Fuel Cells*, 7(3):246–258, 2007.
- [28] John B. Goodenough and Yun Hui Huang. Alternative anode materials for solid oxide fuel cells. *Journal of Power Sources*, 173(1):1–10, 2007.
- [29] Shaowu Zha, Philip Tsang, Zhe Cheng, and Meilin Liu. Electrical properties and sulfur tolerance of La_{0.75}Sr_{0.25}Cr_{1-x}Mn_xO₃ under anodic conditions. *Journal of Solid State Chemistry*, 178(6):1844–1850, 2005.
- [30] S. Primdahl, J. R. Hansen, L. Grahl-Madsen, and P. H. Larsen. Sr-Doped LaCrO₃ Anode for Solid Oxide Fuel Cells. *Journal of The Electrochemical Society*, 148(1):A74, 2001.
- [31] A. Mohammed Hussain, Jens V.T. Høgh, Wei Zhang, Peter Blennow, Nikolaos Bonanos, and Bernard A. Boukamp. Effective improvement of interface modified strontium titanate based solid oxide fuel cell anodes by infiltration with nano-sized palladium and gadolinium-doped cerium oxide. *Electrochimica Acta*, 113:635–643, 2013.
- [32] A. Mohammed Hussain, Jens V.T. Høgh, Torben Jacobsen, and Nikolaos Bonanos. Nickel-ceria infiltrated Nb-doped SrTiO₃for low temperature SOFC anodes and analysis on gas diffusion impedance. *International Journal of Hydrogen Energy*, 37(5):4309–4318, 2012.
- [33] A. Mohammed Hussain, Ke-Ji Pan, Ian A. Robinson, Thomas Hays, and Eric D. Wachsman. Stannate-Based Ceramic Oxide as Anode Materials for Oxide-Ion Conducting Low-Temperature Solid Oxide Fuel Cells. *Journal of The Electrochemical Society*, 163(10):F1198–F1205, 2016.
- [34] Yun-Hui Huang, Ronald I Dass, Zheng-Liang Xing, and John B Goodenough. Double Perovskites as Anode Materials for Solid-Oxide Fuel Cells. *Science*, 2(April):254–258, 2006.
- [35] O Yamamoto. Perovskite-type oxides as oxygen electrodes for high temperature oxide fuel cells. *Solid State Ionics*, 22(2-3):241–246, 1987.

- [36] Harlan U. Anderson. Review of p-type doped perovskite materials for SOFC and other applications. *Solid State Ionics*, 52(1-3):33–41, 1992.
- [37] Tatsumi Ishihara. *Perovskite Oxide for Solid Oxide Fuel Cells*. Springer, 2009.
- [38] Y.-H. Huang, G Liang, M Croft, M Lehtimäki, M Karppinen, and J B Goode-nough. Double-perovskite anode materials Sr₂MMoO₆ (M = Co, Ni) for solid oxide fuel cells. *Chemistry of Materials*, 21(11):2319–2326, 2009.
- [39] Yun-Hui Huang, Ronald I. Dass, Jonathan C. Denyszyn, and John B. Goode-nough. Synthesis and Characterization of Sr₂MgMoO_{6-δ}. *Journal of The Electrochemical Society*, 153(7):A1266, 2006.
- [40] Carlos Bernuy-Lopez, Mathieu Allix, Craig A. Bridges, John B. Claridge, and Matthew J. Rosseinsky. Sr₂MgMoO_{6-δ}: Structure, phase stability, and cation site order control of reduction. *Chemistry of Materials*, 19(5):1035–1043, 2007.
- [41] Ke-Ji Pan, A. Mohammed Hussain, and Eric D. Wachsman. High Performance Low-Temperature Solid Oxide Fuel Cells with SrFe_{0.2}Co_{0.4}Mo_{0.4}O_{3-δ} based Ceramic Anodes.
- [42] A. Mohammed Hussain, Yi-Lin Huang, Ke-Ji Pan, Ian Robinson, and Eric D. Wachsman. A Redox-Robust Ceramic Anode for Low-Temperature SOFC.
- [43] A. Mohammed Hussain, Ian Robinson, Yi-Lin Huang, Ke-Ji Pan, and Eric D. Wachsman. Stable Molybdate-Based Ceramic Anodes for Low-Temperature Solid Oxide Fuel Cells.
- [44] Qin Zhang, Tao Wei, and Yun-hui Huang. Electrochemical performance of double-perovskite Ba₂MMoO₆ (M = Fe, Co, Mn, Ni) anode materials for solid oxide fuel cells. *Journal of Power Sources*, 198:59–65, 2012.
- [45] Nguyen Q. Minh. Solid oxide fuel cell technology - Features and applications. *Solid State Ionics*, 174(1-4):271–277, 2004.
- [46] Vanessa Cascos, José Antonio Alonso, and María Teresa Fernández-Díaz. Nb⁵⁺-Doped SrCoO_{3-δ} Perovskites as Potential Cathodes for Solid-Oxide Fuel Cells. *Materials*, 9(7):579, 2016.
- [47] Zhangwei Chen, Xin Wang, Finn Giuliani, and Alan Atkinson. Fracture Toughness of Porous Material of LSCF in Bulk and Film Forms. *Journal of the American Ceramic Society*, 98(7):2183–2190, 2015.
- [48] Melanie Kuhn, Jae Jin Kim, Sean R Bishop, and Harry L Tuller. Oxygen Nonstoichiometry and Defect Chemistry of Perovskite- Structured Ba_x Sr_{1-x} Ti_{1-y} Fe_y O_{3-y/2+δ} Solid Solutions. *Chemistry of Materials*, 25(1):2970–2975, 2013.

- [49] Jeongpill Ki and Daejong Kim. Computational model to predict thermal dynamics of planar solid oxide fuel cell stack during start-up process. *Journal of Power Sources*, 195(10):3186–3200, may 2010.
- [50] S.H Chan, K.a Khor, and Z.T Xia. A complete polarization model of a solid oxide fuel cell and its sensitivity to the change of cell component thickness. *Journal of Power Sources*, 93(1-2):130–140, 2001.
- [51] Felix Fleischhauer, Andreas Tiefenauer, Thomas Graule, Robert Danzer, Andreas Mai, and Jakob Kuebler. Failure analysis of electrolyte-supported solid oxide fuel cells. *Journal of Power Sources*, 258:382–390, 2014.
- [52] J. Laurencin, G. Delette, F. Lefebvre-Joud, and M. Dupeux. A numerical tool to estimate SOFC mechanical degradation: Case of the planar cell configuration. *Journal of the European Ceramic Society*, 28(9):1857–1869, 2008.
- [53] S.R. Bishop, D. Marrocchelli, C. Chatzichristodoulou, N.H. Perry, M.B. Mogensen, H.L. Tuller, and E.D. Wachsman. Chemical Expansion: Implications for Electrochemical Energy Storage and Conversion Devices. *Annual Review of Materials Research*, 44(1):205–239, 2014.
- [54] Keith L. Duncan, Yanli Wang, Sean R. Bishop, Fereshteh Ebrahimi, and Eric D. Wachsman. Role of point defects in the physical properties of fluorite oxides. *Journal of the American Ceramic Society*, 89(10):3162–3166, 2006.
- [55] Yanli Wang, Keith Duncan, Eric D. Wachsman, and Fereshteh Ebrahimi. The effect of oxygen vacancy concentration on the elastic modulus of fluorite-structured oxides. *Solid State Ionics*, 178(1-2):53–58, 2007.
- [56] David J. Green. *An Introduction to the Mechanical Properties of Ceramics*. Cambridge University Press, 1998.
- [57] Zhen-Yan Deng, Jihong She, Yoshiaki Inagaki, Jian-Feng Yang, Tatsuki Ohji, and Yoshihisa Tanaka. Reinforcement by crack-tip blunting in porous ceramics. *Journal of the European Ceramic Society*, 24(7):2055–2059, jun 2004.
- [58] Milan Ambrožič and Tomaž Kosmač. Optimization of the bend strength of flat-layered alumina-zirconia composites. *Journal of the American Ceramic Society*, 90(5):1545–1550, may 2007.
- [59] Akio Yonezu and Xi Chen. Micro-scale damage characterization in porous ceramics by an acoustic emission technique. *Ceramics International*, 40(7 PART A):9859–9866, 2014.
- [60] S. Meille, M. Lombardi, J. Chevalier, and L. Montanaro. Mechanical properties of porous ceramics in compression: On the transition between elastic, brittle, and cellular behavior. *Journal of the European Ceramic Society*, 32(15):3959–3967, nov 2012.

- [61] Pulin Nie, Heping Lv, Tao Zhou, Xun Cai, and Paul K. Chu. Interfacial adhesion measurement of a ceramic coating on metal substrate. *Journal of Coatings Technology and Research*, 7(3):391–398, may 2010.
- [62] F. Vales, R. Rezakhanlou, and C. Olagnon. Determination of the fracture mechanical parameters of porous ceramics from microstructure parameters measured by quantitative image analysis. *Journal of Materials Science*, 4:4081–4088, 1999.
- [63] Bent F. Sørensen and Andy Horsewell. Crack Growth along Interfaces in Porous Ceramic Layers. *Journal of the American Ceramic Society*, 84(9):2051–2059, dec 2004.
- [64] S. M. Barinov, V. F. Ponomarev, and V. Ya. Shevchenko. Effect of Hot Isostatic Pressing on the Mechanical Properties of Aluminum Oxide Ceramics. *Refractories and Industrial Ceramics*, 38(1-2):9–12, 1997.
- [65] J. J. Roa, M. A. Laguna-Bercero, A. Larrea, V. M. Orera, and M. Segarra. Mechanical properties of highly textured porous Ni-YSZ and Co-YSZ cermets produced from directionally solidified eutectics. *Ceramics International*, 37(8):3123–3131, 2011.
- [66] Arata Nakajo, Jakob Kuebler, Antonin Faes, Ulrich F. Vogt, Hans Jürgen Schindler, Lieh Kwang Chiang, Stefano Modena, Jan Van Herle, and Thomas Hocker. Compilation of mechanical properties for the structural analysis of solid oxide fuel cell stacks. Constitutive materials of anode-supported cells. *Ceramics International*, 38(5):3907–3927, 2012.
- [67] K Yasuda, K Uemura, and T Shiota. Sintering and mechanical properties of gadolinium-doped ceria ceramics. *Journal of Physics: Conference Series*, 339(1):012006, jan 2012.
- [68] Sophie Giraud and Jérôme Canel. Young's modulus of some SOFCs materials as a function of temperature. *Journal of the European Ceramic Society*, 28(1):77–83, 2008.
- [69] Takuto Kushi, Kazuhisa Sato, Atsushi Unemoto, Shinichi Hashimoto, Koji Amezawa, and Tatsuya Kawada. Elastic modulus and internal friction of SOFC electrolytes at high temperatures under controlled atmospheres. *Journal of Power Sources*, 196(19):7989–7993, 2011.
- [70] Koji Amezawa, Takuto Kushi, Kazuhisa Sato, Atsushi Unemoto, Shin Ichi Hashimoto, and Tatsuya Kawada. Elastic moduli of Ce_{0.9}Gd_{0.1}O_{2-??} at high temperatures under controlled atmospheres. *Solid State Ionics*, 198(1):32–38, 2011.
- [71] M. Jenkins, T. Chang, and A. Okura. A Simple Machining Jig for Chevron-notched Specimens. *Experimental Techniques*, 12(8):20–22, 1988.

- [72] ASTM Standard C1421. Standard Test Methods for Determination of Fracture Toughness of Advanced Ceramics at Ambient Temperature. *ASTM International*, pages 1–33, 2016.
- [73] ASTM Standard C1221. Standard Test Method for Flexural Strength of Advanced Ceramics at Elevated Temperatures. *ASTM International*, 11(Reapproved 2008):1–16, 2013.
- [74] Brian H Toby and Robert B. Von Dreele. GSAS-II: The genesis of a modern open-source all purpose crystallography software package. *Journal of Applied Crystallography*, 46(2):544–549, 2013.
- [75] Koichi Momma and Fujio Izumi. VESTA 3 for three-dimensional visualization of crystal, volumetric and morphology data. *Journal of Applied Crystallography*, 44(6):1272–1276, 2011.
- [76] Shang Xian Wu. Fracture toughness determination of bearing steel using chevron-notch three point bend specimen. *Engineering Fracture Mechanics*, 19(2):221–232, 1984.
- [77] Roy W. Rice. *Porosity of Ceramics: Properties and Applications*. Marcel Dekker Inc., New York, 1998.
- [78] Rodger W. Davidge and Anthony G. Evans. The Strength of Ceramics. *Materials Science and Engineering*, (6):281–298, 1970.
- [79] Barry Carter and Grant Norton. *Ceramic Materials Science and Engineering*. 2007.
- [80] Oldřich Ševeček, Michal Kotoul, Dominique Leguillon, Eric Martin, and Raul Bermejo. Assessment of crack-related problems in layered ceramics using the finite fracture mechanics and coupled stress-energy criterion. *Procedia Structural Integrity*, 2:2014–2021, 2016.
- [81] James T Richardson, Robert Scates, and Martyn V Twigg. X-ray diffraction study of nickel oxide reduction by hydrogen. *Applied Catalysis A: General*, 246:137–150, 2003.
- [82] Clemens Ritter, Javier Blasco, Jose-Maria De Teresa, David Serrate, Luis Morellon, Joaquin Garcia, and Manuel Ricardo Ibarra. Structural and magnetic details of 3d-element doped Sr₂Fe_{0.75}T_{0.25}MoO₆. *Solid State Sciences*, 6(5):419–431, 2004.
- [83] D. S. Tsvetkov, I. L. Ivanov, D. A. Malyshkin, A. S. Steparuk, and A. Yu. Zuev. The defect structure and chemical lattice strain of the double perovskites Sr₂BMoO_{6-δ} (B = Mg, Fe). *Dalton Transactions*, 45(32):12906–12913, 2016.

- [84] B. Levasseur and S. Kaliaguine. Effects of iron and cerium in La_{1-y}Ce_yCo_{1-x}Fe_xO₃ perovskites as catalysts for VOC oxidation. *Applied Catalysis B: Environmental*, 88(3-4):305–314, 2009.
- [85] Qiang Liu, Daniel E. Bugaris, Guoliang Xiao, Maxwell Chmara, Shuguo Ma, Hans Conrad Zur Loyer, Michael D. Amiridis, and Fanglin Chen. Sr₂Fe_{1.5}Mo_{0.5}O_{6-delta} as a regenerative anode for solid oxide fuel cells. *Journal of Power Sources*, 196(22):9148–9153, 2011.
- [86] S. Vasala, M. Lehtimäki, Y. H. Huang, H. Yamauchi, J. B. Goodenough, and M. Karppinen. Degree of order and redox balance in B-site ordered double-perovskite oxides, Sr₂MMoO_{6-δ}(M=Mg, Mn, Fe, Co, Ni, Zn). *Journal of Solid State Chemistry*, 183(5):1007–1012, 2010.
- [87] D. Marrero-López, J. Peña-Martínez, J. C. Ruiz-Morales, M. Gabás, P. Núñez, M. A G Aranda, and J. R. Ramos-Barrado. Redox behaviour, chemical compatibility and electrochemical performance of Sr₂MgMoO_{6 - δ} as SOFC anode. *Solid State Ionics*, 180(40):1672–1682, 2010.
- [88] R Kircheisen and J. Töpfer. Nonstoichiometry, point defects and magnetic properties in Sr₂FeMoO_{6-δ} double perovskites. *Journal of Solid State Chemistry*, 185:76–81, 2012.
- [89] Keith L. Duncan and Eric D. Wachsman. General model for the functional dependence of defect concentration on oxygen potential in mixed conducting oxides. *Ionics*, 13(3):127–140, 2007.
- [90] A. Holt, T. Norby, and R. Glenne. Defects And Transport In SrFe(1-x)CO_xO_{3.5}. *Ionics*, 5(5-6):434–443, 1999.
- [91] S R Bishop, K L Duncan, and E D Wachsman. Surface and bulk oxygen non-stoichiometry and bulk chemical expansion in gadolinium-doped cerium oxide. *Acta Materialia*, 57(12):3596–3605, 2009.
- [92] Patrick Stanley, A Mohammed Hussain, Yi-lin Huang, J Evans Gritton, Jonathan A O Neill, and Eric D Wachsman. Defect chemistry and oxygen non-stoichiometry for solid-oxide fuel cells. pages 1–19.
- [93] Robert Danzer, Tanja Lube, Peter Supancic, and Rajiv Damani. Fracture of ceramics. *Advanced Engineering Materials*, 10(4):275–298, 2008.
- [94] David Waldbillig, Anthony Wood, and Douglas G. Ivey. Thermal analysis of the cyclic reduction and oxidation behaviour of SOFC anodes. *Solid State Ionics*, 176(9-10):847–859, 2005.